ACS Catalysis

pubs.acs.org/acscatalysis Review

Operando Methods in Electrocatalysis

Yao Yang,[#] Yin Xiong,[#] Rui Zeng, Xinyao Lu, Mihail Krumov, Xin Huang, Weixuan Xu, Hongsen Wang, Francis J. DiSalvo, Joel. D. Brock, David A. Muller, and Héctor D. Abruña*

Cite This: *ACS Catal.* 2021, 11, 1136–1178 Read Online

ACCESS | Metrics & More | Article Recommendations

ABSTRACT: Electrocatalysis has been the cornerstone for enhancing energy efficiency, minimizing environmental impacts and carbon emissions, and enabling a more sustainable way of meeting global energy needs. Elucidating the structure and reaction mechanisms of electrocatalysts at electrode−electrolyte interfaces is fundamental for advancing renewable energy technologies, including fuel cells, water electrolyzers, CO_2 reduction, and batteries, among others. One of the fundamental challenges in electrocatalysis is understanding how to activate and sustain electrocatalytic activity, under operating conditions, for extended time periods and with optimal activity and selectivity. Although traditional *ex situ* methods have provided a baseline understanding of heterogeneous (electro)catalysts, they cannot provide real-time interfacial structural and compositional changes under reaction conditions, which calls for the use of *in situ/operando* methods. Herein, we provide a selective review of *in situ* and *operando* characterizations, in particular, the use of *operando* synchrotron-based X-ray techniques and *in situ* atomic-scale scanning transmission electron microscopy (STEM) in liquid/gas phases to advance our understanding of electrode−electrolyte interfaces at macro- and microscopic levels, which dictate the charge transfer kinetics and overall reaction mechanisms. The use of scanning electrochemical microscopy (SECM) enables direct probing of the local activity of electrocatalysts at the nanometer scale. In addition, differential electrochemical mass spectrometry (DEMS) and the electrochemical quartz crystal balance (EQCM) enable the simultaneous identification of multiple reaction intermediates and products for mechanistic studies of electrocatalyst selectivity and durability. We anticipate that continuous advances of *in situ/operando* techniques and probes will continue to make significant contributions to establishing structure/composition-reactivity correlations of electrocatalysts at unprecedented atomic-scale and molecular levels under realistic, real-time reaction conditions.

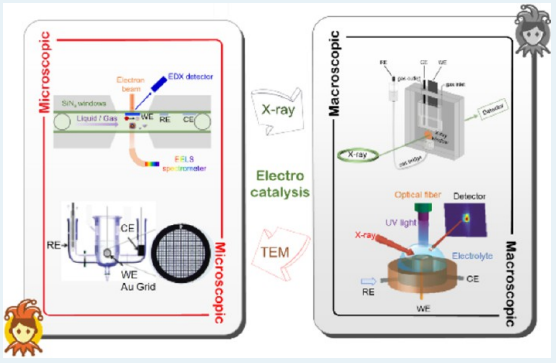

KEYWORDS: *Operando, In situ, Electrocatalysis, Synchrotron X-ray, STEM, SECM, EQCM, DEMS*

Downloaded via Hector Abruna on January 12, 2021 at 02:56:26 (UTC).
See https://pubs.acs.org/sharingguidelines for options on how to legitimately share published articles.

1. INTRODUCTION

Understanding the structure and composition of energy materials and their reaction mechanisms is crucial to the design of high-performance electrocatalysts for renewable energy technologies, particularly fuel cells and electrolyzers. Over the past few decades, advanced analytic methods have dramatically shaped/changed our understanding of materials design and electrocatalytic processes. The use of modern *in situ/operando* techniques has provided extraordinarily valuable insights for establishing structure/composition-reactivity correlations under real-time reaction conditions.[1,2] In this review, we focus on the technological developments and their applications to electrocatalysts of X-ray-based methods and transmission electron microscopy (TEM) for structural and chemical analysis, scanning electrochemical microscopy (SECM) for the direct probing of local activity, and differential electrochemical mass spectroscopy (DEMS) and electrochemical quartz crystal microbalance (EQCM) for dynamic electrochemical studies. We define the terms, "*in situ*" and "*operando*", as follows: *In situ* (Latin, on site/in position) refers to the real-time measurement of an (electro)catalytic process under relevant reaction conditions versus the conventional *ex situ* (Latin, off site) measurements performed before and after reactions. *In situ* methods need to take into account the operating conditions of instruments (e.g., low temperature, high vacuum), which often deviate from the optimal (electro)catalytic reaction conditions (e.g., elevated temperatures and pressures under a gas/liquid environment). *Operando* (Latin, operating/working) refers to the measurement of a working (electro)catalyst under the same reaction conditions as those inside a catalytic reactor or an actual operating device. *Operando* methods minimize the exper-

Received: November 3, 2020
Revised: December 23, 2020

© XXXX American Chemical Society

https://dx.doi.org/10.1021/acscatal.0c04789
ACS Catal. 2021, 11, 1136−1178

imental gap in measurement conditions between instrumental requirements and realistic (electro)catalytic reactions. The term "*operando* spectroscopy" was first proposed by Bañares, Weckhuysen, and others in 2002 as an alternative for "*in situ* spectroscopy" to emphasize the importance of maintaining working conditions of (electro)catalysts in a regular reactor/device.[4,5] The term *in situ* has been widely used by many researchers for the past few decades since the real *operando* measurements often required considerably more complexity in device design and are just emerging in the literature. This review serves as an overview of the development of *in situ*/*operando* techniques in electrocatalysis and highlights the revolutionary transition toward *operando* approaches.

Synchrotron-based X-ray spectroscopy can provide a great deal of information for identifying the electronic structure and coordination environment of active sites. *Ex situ* X-ray absorption spectroscopy (XAS) has been widely used to establish a baseline understanding of the structure−activity correlations for electrocatalysts in fuel cells, water splitting, metal-air batteries, CO_2 reduction, and many other energy-related applications, including precious-metal-based alloys, nonprecious-metal-based perovskites, spinel oxides, Co/Fe-containing N-doped carbons, and others. The significant penetration depth and high flux of high-energy X-rays enable the *operando* study of electrode−electrolyte interfaces under real-time electrochemical conditions. *In situ*/*operando* XAS has been widely used to study valence changes and bonding information on Pt-based catalysts for the ORR in fuel cells and methanol/ethanol oxidation in both homemade half-cell devices and practical membrane electrode assembly (MEA) test stations. Recently, we have employed *operando* XAS to study the synergistic effects of bimetallic and trimetallic oxide catalysts in alkaline fuel cells, under both steady state and potentiodynamic conditions. In addition, *operando* surface-sensitive X-ray scattering techniques, in particular, crystal truncation rods (CTR) and X-ray standing wave (XSWs), enable an atomic-scale understanding of the electrode−electrolyte interface. Special attention is paid to combining multiple X-ray based techniques to provide complementary chemical and structural information under similar reaction conditions.

Newly developed aberration-corrected scanning/transmission electron microscopes (S/TEM) equipped with electron energy loss spectroscopy (EELS) and energy dispersive X-ray spectroscopy (EDX) can provide atomic-scale spatial resolution with an unprecedented level of compositional information and local electronic structure of electrocatalysts. S/TEM equipped with EELS and EDX have been employed to characterize a variety of novel materials, including core−shell or surface-modified nanoparticles, shape-controlled nanocrystals, hollow/spongy-structured nanoparticles (with complex interior architectures), and atomically dispersed transition metal atoms on substrates. S/TEM has been widely used to capture the morphological, chemical, and atomic structures of nanocatalysts, which may be missed in bulk X-ray analysis, leading to the discovery of novel nanomaterials and to a more rational design of catalyst structures. In particular, identical-location TEM (IL-TEM) can probe the facet and shape evolution and catalyst degradation mechanisms precisely at the same location before and after electrochemical tests.

It has been a longstanding challenge in TEM to investigate catalytic reactions *in situ* in gas or liquid environments due to the required high vacuum conditions. Newly developed *in situ* environmental TEM methods are enabling the study of the real-time evolution of catalysts in electrochemical reactions with unprecedented spatial, temporal and energy resolutions. The majority of energy-related reactions, particularly electrochemical processes, occur at the electrode−electrolyte interface in solution phase. *In situ* electrochemical liquid cell TEM is well positioned to provide unique insights on interfacial electrocatalytic process with nanometer-scale (or higher) resolution, as well as compositional and chemical bonding information during the reaction process. Our group has used an *in situ* liquid cell TEM to study the electrochemical behavior of Pt in liquids and dynamic de/lithiation processes of $LiFePO_4$ during dis/charge cycles. These fast-evolving techniques have been employed to understand electrochemical deposition, nanomaterial synthesis and structural evolution, corrosion chemistry, and diffusion in liquids. The environmental TEM, under controlled temperature and gas environments, enables the *in situ* study of the dynamical behavior of nanomaterials at high temperatures and pressures up to and including atmospheric pressure. *In situ* heating TEM can yield new information and insights into the thermal stability of Pt-based catalysts, surface reconstructions and elemental distribution of Pt-based catalysts, as well as shape and facet evolution of metal nanoparticle catalysts in variable gas environments. We recently employed *in situ* heating TEM, together with *in situ* heating XRD, to quantify the degree of ordering in Pt_3Co nanoparticles, and study the (order/disorder) phase transition and morphological changes during the high-temperature annealing process. Coupled with EELS and mass spectrometry, *in situ* gas-phase TEM can simultaneously provide compositional and bonding information and online detection of reaction productions with high sensitivity and selectivity.

SECM can directly measure electrochemical activity, kinetics, and adsorbate coverages with nanometer-scale spatial resolution, sufficiently high for single nanoparticle studies. It is naturally an *in situ* and quantitative technique specialized for interfacial studies of electrochemical processes. Utilizing the full potential of SECM requires a fundamental knowledge and understanding of electrochemistry, through understanding of the technique and its limitations, and attention to design of the experiment and experimental details. However, when appropriately and successfully applied, SECM can be an invaluable tool for fundamental studies of electrocatalysis because the electrochemical processes of interest are not inferred from other measurables but rather are directly probed.

DEMS is a very sensitive analytical technique with a detection limit of ∼0.1 nmol, capable of analyzing even sub-monolayers of organic adsorbates and volatile reaction products. The development of DEMS requires the consistent innovation in the architectures of DEMS cells, such as the conventional cell, thin-layer flow cell, dual thin layer flow cell, and capillary inlet. DEMS has been used to elucidate the mechanism of CO oxidation for designing effective CO-tolerant electrocatalysts as well as the reaction pathways of methanol, ethanol, and formic acid oxidation for fuel cell applications. DEMS systems have been coupled to ATR-FTIR for detecting intermediate species and with SECM for combinatorial catalyst screening. In particular, the double-band-electrode channel flow DEMS is akin to the rotating ring disk electrode (RRDE) system enabling the simultaneous detection of a variety of volatile products during methanol

https://dx.doi.org/10.1021/acscatal.0c04789
ACS Catal. 2021, 11, 1136−1178

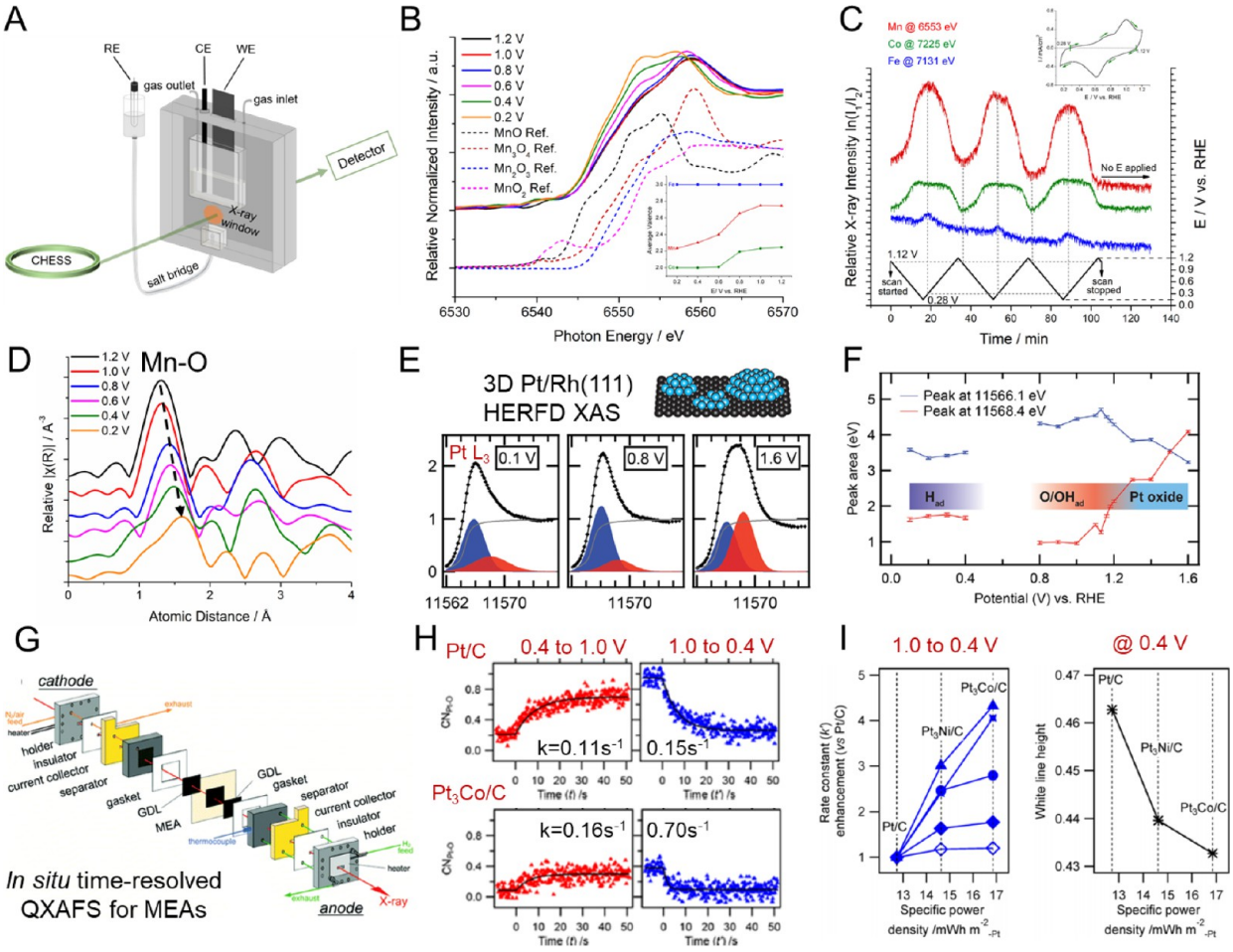

Figure 1. *Operando* X-ray absorption spectroscopy for electrocatalysis. (A) Schematic of an *operando* XAS electrochemical cell with a working electrode (WE, catalyst on carbon paper) and counter electrode (CE, carbon rod) immersed in 1 M KOH. CHESS stands for Cornell High-Energy Synchrotron Source. (B) *Operando* XANES spectra at the Mn K-edge of Mn−Co−Fe trimetallic spinel oxides (solid lines) and the reference manganese oxides (dashed lines). Inset shows the calculated average metal valence as a function of potential based on the linear combination fitting using XANES spectra of reference metal oxides. (C) Periodic changes of the relative X-ray intensities ($\ln(I_1/I_2)$) at 6553 eV (Mn K-edge), 7225 eV (Co K-edge), and 7131 eV (Fe K-edge), respectively, as a function of the cyclic potential. The upper inset shows the corresponding CV at 1 mV/s from 0.15 to 1.2 V vs RHE. (D) *Operando* EXAFS of Mn at a series of applied potentials with no phase correction. The Mn−O bond distance increased as the applied potential decreased from 1.2 to 0.2 V. (E−F) Deconvolution of *in situ* HERFD XAS of Pt islands/Rh(111) in 0.01 M $HClO_4$ showing the signatures of H_{ad} and O/OH_{ad} and changes in their peak areas as a function of applied potentials. (G) Schematic of a laboratory-made PEMFC for *in situ* QXAFS measurements. (H) Time profiles of coordination numbers of Pt−O bonds of Pt/C and Pt_3Co/C during voltage cycling between 0.4 and 1.0 V. (I) Left: Relationships between enhancements in the rate constants during the voltage cycling from 1.0 to 0.4 V in N_2 and specific power density (triangles, circles, and diamond signs refer to CN_{Pt-O}, CN_{Pt-Pt}, and charge transfer processes, respectively). Right: Relationship between Pt L_{III}-edge XANES white line amplitude of Pt and Pt-bimetallic cathode catalysts at 0.4 V in N_2 and specific power density. (A−D) are reprinted with permission from refs 7 and 8. Copyright by the authors 2019 American Chemical Society. (E−F) are reprinted with permission from ref 25. Copyright 2012 American Chemical Society. (G−H) are reprinted with permission from refs 32, 33. Copyright 2012, 2014 American Chemical Society.

oxidation with a high collection efficiency and short response time.

The EQCM enables the study of the dynamic electrochemical processes at the electrode surfaces with a mass resolution better than 10 ng/cm^2. It has the capability of detecting the mass changes through both faradaic and nonfaradaic process, in addition to the electrochemical signals. It has been used for fundamental studies of films and membranes deposited on electrodes and has provided great insights of potential dependent ion and solvent dynamics. In particular, the EQCM has been employed to study the catalyst/electrolyte interfacial processes, such as catalyst deposition and degradation mechanism(s), the adsorption/desorption of intermediates on electrocatalysts, and the ionic movement in polymer membranes.

In this illustrative (though not comprehensive) review, we present the working principles of the above-described techniques followed by selected examples from our work as well as the work of others.

2. *OPERANDO* SYNCHROTRON-BASED X-RAY TECHNIQUES

The high penetration depth and high intensity of synchrotron-based high-energy X-rays enable the *operando* study of electrochemical interfaces under real-time reaction conditions.[1−3] In this section, we will present a select review of *operando* X-ray methods in electrocatalysis for energy-related

https://dx.doi.org/10.1021/acscatal.0c04789
ACS Catal. 2021, 11, 1136−1178

electrochemical reactions with an emphasis on X-ray absorption spectroscopy (XAS) and surface-sensitive X-ray scattering and spectroscopic techniques. *Operando* XAS has been extensively used to provide spectroscopic information on electronic structures. Two types of *operando* surface-sensitive X-ray techniques, including crystal truncation rods (CTRs) and X-ray standing waves (XSWs), will be discussed in detail to highlight their contributions in resolving the structural changes at electrode/electrolyte interfaces at the atomic scale. In addition, the application of *in situ* ambient-pressure X-ray photoelectron spectroscopy (AP-XPS) will be introduced to elucidate the nature of reaction intermediates, such as O-containing species during the ORR in fuel cells. The advantages of incorporating multiple X-ray techniques into one experiment will be given particular attention due to their capability of providing tremendously valuable complementary information. Two examples will be highlighted, including the coupling of XSWs and AP-XPS and the coupling of XAS and small-angle X-ray scattering (SAXS).

2.1. *Operando* X-ray Absorption Spectroscopy. In X-ray absorption spectroscopy (XAS), one measures the changes in X-ray absorption or fluorescence as a function of X-ray photon energy. The X-ray energy is sufficiently high to excite core-level electrons to higher-level unoccupied states. The X-ray absorption process follows the Beer−Lambert law, $A = \log(I_o/I_1) = \mu z$, where μ is the absorption coefficient and z is the sample thickness. An XAS can be divided into three regions: the pre-edge region, X-ray absorption near-edge structure (XANES), and extended X-ray absorption fine structure (EXAFS). The XANES region extends from the edge/near-edge to about 50 eV above the adsorption edge, which reveals information pertaining to the position/occupancy of orbitals, site symmetry, and electronic configuration (i.e., oxidation state). The EXAFS region is energetically further away above the edge, starting at around 50 eV and extending up to 1000 eV. The dominant features are the oscillations in the absorption coefficient, with a magnitude that is typically less than 15% of the edge intensity. The oscillations originate from the interference between the outgoing and backscattered waves of photoelectrons ejected from the absorbing atoms. The frequency and amplitude of the EXAFS oscillations can provide valuable information about near-neighbor distances, coordination numbers, and identities. The EXAFS signal is dominated by single electron, single scattering events in which the plane wave approximation is valid, which can result in determination of interatomic distances and coordination numbers with an accuracy of ±0.02 Å and ±20%, respectively, given appropriate phase correction and fitting procedures.[1,2] In contrast, in the interpretation of XANES, one must consider the dominant multiple scattering near the absorption edge and adapt a spherical photoelectron wave approximation, which requires rather complex theoretical modeling. A detailed analysis of the XANES and EXAFS spectra are beyond the scope of this review, and interested readers are encouraged to read our early review[2] as well as comprehensive reviews by Russell and others.[3]

Synchrotron-based XAS studies of electrocatalysts have provided tremendous information about their electronic structures, coordination environments, site symmetry, etc., which are particularly sensitive for distinguishing different elements in multimetallic metal oxides.[6] The success of an *operando* XAS experiment relies on the customized design of electrochemical cells suited for the target electrocatalytic reactions.[3] Benefiting from its high X-ray intensity, broad energy range, and high energy resolution, synchrotron radiation has become the standard X-ray source for XAS measurements. XAS measurements are often performed in a transmission mode as shown in Figure 1A.[7,8] The sample thickness needs to be optimized to yield the maximum change in the absorbance while not being too thick to minimize background absorption. A typical X-ray absorbance is in the range of 0.3−1.0, depending on the elements of interest and sample thickness and can be calculated in advance with a knowledge of the X-ray absorption cross sections. For electrocatalysts in powder or film forms, the total thickness of the electrolyte and catalyst support needs to be sufficiently thin to minimize background absorption and scattering while not being too thin to cause an undesirable *iR*-drop in the electrochemical signals, which is critical for high-quality XANES and EXAFS. The total thickness in the homemade cell in Figure 1A was designed to be below 200 μm with a catalyst layer of less than 50 μm. The reference electrode (RE) was connected through a salt bridge to minimize the *iR*-drop in such a thin liquid-cell configuration (Figure 1A).[7] It is essential to realize that X-rays can cause radiation damage to the catalysts, electrolytes, and other parts of the cell. Strategies, such as constantly flowing fresh electrolyte, lowering the incident intensity, and translating the X-ray illuminated area, can effectively mitigate such radiation damage. In cases of thick samples or low elemental concentration, XAS measurements can instead be performed in a fluorescence mode, in which the sample is often positioned at 45° relative to the incident X-ray beam,[8] with the fluorescence detector placed perpendicular to the incident beam direction, to minimize the effects of Compton scattering.

Operando XAS has been extensively used to study changes in precious metal-based electrocatalysts for the oxygen reduction reaction,[9−15] nonprecious metal oxides for water oxidation,[15−18] and CO oxidation[19] among other electrocatalytic reactions. Recently, it has also been used to study metal-containing N-doped carbon (M−N−C) electrocatalysts for the ORR in alkaline media.[20−22] We recently employed *operando* XAS to investigate the synergistic catalytic effects of a Co−Mn bimetallic spinel oxide catalyst. This material exhibited significantly higher ORR activity than both Co_3O_4/C and Mn_3O_4/C and outperformed commercial Pt/C catalysts in alkaline fuel cells.[6−8] *Operando* XANES was used to track/monitor the oxidation state changes of Co and Mn not only under steady state (constant applied potential) but also under non-steady state (potentiodynamic, cyclic voltammetry) conditions.[7] Rapid X-ray data acquisition, combined with a slow sweep rate in CV, enabled a 3 mV resolution in the applied potential, approaching a non-steady state. Changes in the Co and Mn valence states were synchronized and exhibited periodic patterns that tracked the cyclic potential sweeps. The non-steady state study suggested possible synergistic effects between Co and Mn, which may explain the superior activity of the $Co_{1.5}Mn_{1.5}O_4$/C electrocatalyst over the monometallic oxide counterparts. We further employed *operando* XANES and EXAFS to investigate the structural roles of a more durable Mn−Co−Fe trimetallic oxide under electrochemical conditions.[8] As shown in Figure 1B, the XANES spectra of the Mn K-edge of Mn−Co−Fe oxides exhibit progressive changes in local electronic structures under various applied potentials (all potentials in this review are versus the reversible hydrogen

https://dx.doi.org/10.1021/acscatal.0c04789
ACS Catal. 2021, 11, 1136−1178

electrode (RHE) unless otherwise noted). The main absorption edge at around 6560 eV corresponds to the excitation of 1s core electrons to unoccupied 4p orbitals. The shoulder peak at ~6553 eV shows a progressive shift to lower energies and an increase in peak intensity when applied potential decreased from 1.2 to 0.2 V, indicating the reduction of Mn at more negative potentials. The linear combination fitting analysis of Mn XANES spectra with pure Mn oxide references enabled quantifying changes in the average valences of Mn, Co, and Fe (Figure 1B, inset). The averaged Mn valences continued to decrease from 2.58 to 2.23 when the potential decreased from 1.2 to 0.2 V, while the Co valences decreased from 2.25 to 2.0 (meaning Co is fully reduced to CoO(II)) when the potential decreased from 1.2 to 0.6 V and remained at 2.0 as the potential was further lowered to 0.2 V. However, the average Fe valence remained virtually unchanged at 3.0 over the entire potential range, indicating that Fe was chemically stable, even under a strong reducing environment. Figure 1C presents the dynamic changes in the valence states of Mn, Co, and Fe during CV measurements. The changes in relative X-ray absorption intensity at characteristic energy values of Mn, Co, and Fe are used to represent the relative changes in metal valences. Mn and Co valences changed synchronically in a periodic fashion under applied potentials with intensity increases and decreases, corresponding to reduction and oxidation of those two elements, respectively. The highest and lowest X-ray intensities are marked by two boundary potentials of 0.28 and 1.12 V, respectively, which are fully consistent with the potentials separating oxidation and reduction currents (0.28, 1.12 V) (dashed lines in Figure 1C inset). In sharp contrast, the oxidation state of Fe remained virtually constant during the CV. This shows that the fast-tracking strategy, described here, is capable of accurately monitoring dynamic changes with an mV-level potential resolution. We thus propose a collaborative effort among Mn, Co, and Fe, in which Mn and Co serve as the synergistic coactive sites to catalyze the reduction of oxygen, resulting in the observed high electrocatalytic activity, while Fe works to maintain the integrity of the spinel structure, likely contributing to the remarkable durability of the catalyst. Additionally, *operando* EXAFS showed the changes in Mn−O interatomic distances under applied potentials (Figure 1D). The Mn−O atomic distance (no phase correction) increased from 2.23 to 2.58 Å as the potential decreased from 1.2 to 0.2 V. The longer Mn−O interatomic distance is consistent with a gradual decrease in the Mn valence. Similar changes in the Co−O distances occurred, while Fe−O showed no appreciable changes under all potentials, again confirming that Fe serves as the stabilizing element to help maintain the structural integrity of the spinel structure and enhance long-term durability.

In a conventional XAS experiment, the energy resolution is limited by the intrinsic lifetime broadening of the core hole. With high-energy resolution fluorescence detected (HERFD) XANES, it is possible to select one particular fluorescence decay channel and isolate the decay transition from a single orbital with a much longer lifetime, minimizing the energy broadening and sharpening the spectral features. HERFD XANES can achieve an energy resolution of 1−5 eV with the use of spherically bent single-crystal spectrometers, while a traditional solid-state detector generally has an energy resolution of 50−200 eV.[23,24] Figure 1E shows an *operando* HERFD XANES study of the surface oxidation of Pt nanoislands on Rh(111) in acid media by Nilsson et al.[25] By selecting the Pt Lα_1 fluorescence line at 9442 eV, the HERFD XANES of Pt L_3 edge (2p-5d transitions) exhibited one sharp peak (blue) at ~11566 eV and another broad peak (red) at ~11568 eV, which were assigned to chemisorbed H and O/OH on Pt surfaces, respectively. Quantitative analysis of those two peaks suggested a progressive increase in the O/OH coverage as the potential increased from 0.8 to 1.13 V, followed by the formation of Pt oxide at higher potentials. Concomitantly, the H_{ads} coverage experienced a subtle increase from 0.8 to 1.13 V, possibly influenced by the coexistence of O/OH_{ads}, and then a significant decay as the potential was further increased to 1.6 V. Corresponding DFT simulations indicated that H and OH adsorption energies on Pt, and the predicted ORR activity, were strongly modulated by the strain and ligand effects of the Rh(111) substrate as well as the thickness and under-coordinated sites on the Pt islands. This HERFD XANES study was able to differentiate the adsorbed O-containing species ($O/OH/H_2O$) from surface Pt oxide,[26,27] and in general, provide much better energy resolution for XANES and EXAFS spectra to identify different oxidation states and chemical environments of electrocatalysts. Readers are referred to reviews by Glatzel, Bergmann, and others for detailed analysis of HERFD XAS measurments.[24]

A high-quality full XAS spectrum, including XANES and EXAFS, often takes half an hour to hours to acquire with a conventional monochromator, making it essentially impossible to track fast reaction dynamics. Besides the strategy of time scan at certain X-ray energy values described in Figure 1C, the Quick XAFS (QXAFS) approach can reduce the acquisition time to seconds or milliseconds, by using a microstepper to continuously scan the monochromator and an energy-dispersive monochromator.[3] The high penetration depth of high energy synchrotron-based X-ray beams enable XAS as a unique technique to study fast reaction kinetics in realistic MEA devices. Early *operando* XAS studies of MEAs by Smotkin, Mukerjee, and others have provided valuable insights into the structural changes of catalysts during fuel cell operation, when compared to the widely used half-cell design.[28−31] Figure 1G illustrates the experimental setup of *in situ/operando* time-resolved QXAFS for MEAs in PEMFCs with a Pt_3Co/C or Pt_3Ni/C cathode in transmission mode.[32−35] Pd/C catalysts were used in the anode, instead of the standard Pt/C, to ensure that the Pt signal was only from the oxygen cathode. A Nafion membrane coated with catalysts was assembled with gas diffusion layers (GDL) made of carbon paper, gasket, current collector, and graphite flow fields, in which a small hole was drilled to allow the X-ray to pass through with minimal background scattering (Figure 1G). A voltage-step cycling process was applied from 0.4 to 1.0 V (oxidation process) and 1.0 to 0.4 V (reduction process), i.e., a potential-step chronoamperometry measurement, to simulate the repetitive power off/on processes, with rapid changes in cell voltages, during automotive operation (Figure 1H). Time transient profiles of the coordination numbers of Pt−O (CN_{Pt-O}) of Pt/C and Pt_3Co/C were acquired at time intervals of 100 ms during voltage cycling between 0.4 and 1.0 V. In the oxidation process (0.4−1.0 V), both Pt/C and Pt_3Co/C showed an increase in CN_{Pt-O}, corresponding to a partial dissociation of Pt−Pt bonds and formation of Pt−O on Pt surfaces, while Pt_3Co/C showed a considerably smaller variation in CN_{Pt-O} than Pt/C. In the reduction process (1.0 to 0.4 V), similar smaller variations were observed for Pt_3Co/C. Fitting the time transients to exponential decay functions

https://dx.doi.org/10.1021/acscatal.0c04789
ACS Catal. 2021, 11, 1136−1178

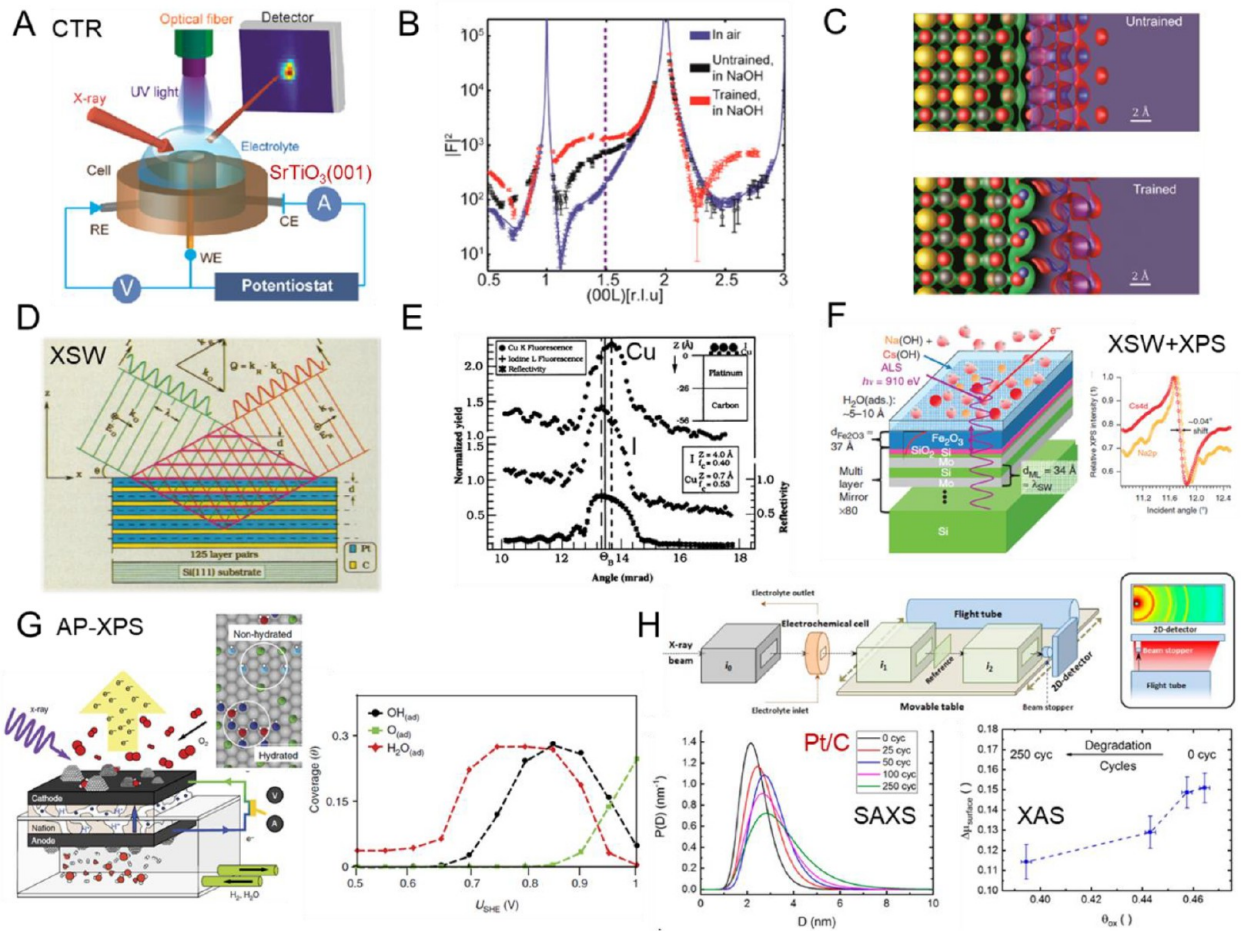

Figure 2. *Operando* surface-sensitive X-ray scattering and coupled structural and spectroscopic techniques. (A) Schematic of the experimental setup for *operando* X-ray reflectivity of $SrTiO_3$ during photoelectrochemical water splitting in alkaline media. (B) Structure factor of 00L CTR of $SrTiO_3$ in air (blue), in 0.1 M NaOH at open circuit before (black) and after (red) electrochemical training (positive bias). "r.l.u." stands for reciprocal lattice units. Blue solid line is the best nonlinear least-squares fit to the CTR of $SrTiO_3$ in air, using the TiO_2 double-layer model. (C) JDFT structure for $SrTiO_3$ surface before and after training. Yellow spheres are Sr, red are O, blue are H, and silver are Ti atoms. Green, red, and blue density contours represent electron, O, and H density, respectively. (D) Depiction of the generation of an X-ray standing wave (XSW) by Bragg reflection from a Pt/C-layered synthetic microstructure. k_o and k_R refer to the wave vectors of incident and reflected plane waves, respectively, and Q is the momentum transfer. (E) Reflectivity profile and normalized fluorescence yields for I and Cu for a Pt/C LSM with an electrodeposited layer of copper and adsorbed iodide layer. Inset: Depiction of the location of the I and Cu layers on the Pt/C LSM. (F) Configuration of XSW studies of cation distribution on poly-Fe_2O_3 on Si/Mo LSM and relative XPS intensity of Na and K as a function of the incident angle. (G) Schematic of an AP-XPS setup for a PEM fuel cell and a snapshot of the surface adsorbates on Pt surface at 0.95 V (red, blue, and cyan circles refer to H_2O_{ad}, OH_{ad}, and O_{ad}, respectively). Calculated coverages of adsorbed O-containing species as a function of computed electrochemical potentials. (H) Upper panel: Schematic representation of the combined SAXS and XAS setup; lower left panel: impact of the electrochemical potential on the Pt/C nanoparticle PSDs, derived from the fitting of *operando* SAXS curves. Lower right panel: Evolution of $\Delta\mu$, calculated from *operando* XANES, as a function of oxide coverage derived from CV profiles. (A–C) are reprinted with permission from ref 50. Copyright by the authors 2016 American Chemical Society. (D–E) are reprinted with permission from ref 60. Copyright by the authors 1990 American Association for the Advancement of Science. (F) is reprinted with permission from ref 63. Copyright 2014 Springer Nature. (G) is reprinted with permission from ref 69. Copyright 2013 Springer Nature. (H) is reprinted with permission from ref 75. Copyright 2016 American Chemical Society.

(solid lines in Figure 1H) demonstrated that, while Pt_3Co (0.16 s^{-1}) and Pt/C (0.13 s^{-1}) had similar rate constants when the voltage increased from 0.4 to 1.0 V, Pt_3Co exhibited a much larger rate constant (0.70 s^{-1}) than Pt/C (0.15 s^{-1}) in the reduction process. Figure 1I (left plot) shows, in the reduction process, the significant enhancement in rate constants of CN_{Pt-O} (triangles) and CN_{Pt-Pt} (circles) extracted from QXAFS and charge transfer extracted from the current–time profile (diamond signs), which follow the order: Pt_3Co/C > $Pt_3Ni/C \gg Pt/C$. This is fully consistent with the observed trends in their ORR activities in PEMFCs. Such a correlation indicates that the rate constant of CN_{Pt-O} is closely related to the desorption rate of oxygen on Pt surfaces and, thus, the reaction kinetics of Pt–O breaking during the ORR. Additionally, the white line intensity at 0.4 V reflects the density of unoccupied Pt 5d bands, which are directly related to the oxidation state of Pt (Figure 1I, right plot). The descending order in white line intensity, $Pt/C \ll Pt_3Ni/C < Pt_3Co/C$, suggests a higher-level electron filling in those unoccupied states accompanied by a downshift in their 5d-band centers. This observation is consistent with early reports by Stamenković and Marković on the Volcano-type correlation between d-band center of Pt-3d metal alloys and their observed ORR activity in acidic media.[36,37] The time-resolved QXAFS method described here provides a unique opportunity to elucidate the reaction kinetics of the ORR in MEAs with

https://dx.doi.org/10.1021/acscatal.0c04789
ACS Catal. 2021, 11, 1136–1178

second or even millisecond-level time resolution and shows the promise to understand the dynamic structural changes under an oxygen environment at high oxidizing potentials. Additionally, although XAS generally provides bulk information, surface chemical information can be collected as well, either through detecting Auger electrons or by employing a grazing incidence geometry. A particular example of iodine adsorption on Ag(111) can be found in early work with surface EXAFS by Citrin.[38] As a complementary technique to resolve the light elements in water inside an MEA, rather than the X-ray sensitive heavy elements, *operando* neutron scattering is particularly useful. Neutron scattering is very sensitive to hydrogen due to its large neutron scattering cross section, enabling the investigation of the dynamics of water flooding at the anode and water depletion at the cathode, contributing to the understanding of water management, which is critical for enhancing the performance of alkaline/anion exchange membrane fuel cells (AEMFCs).[39] Moreover, since H and D have opposite signs in their neutron scattering lengths, one can enhance the contrast of electrolyte species by working with "compensated water" in which the neutron scattering from water is effectively eliminated.

In summary, in this section, we have presented recent progress in *operando* XANES and EXAFS in both homemade half cells as well as realistic MEA devices. We are confident that future developments will yield additional valuable insights for resolving the subtle changes in chemical environment and electronic structures on electrocatalyst surfaces and the tracking of fast kinetics under reaction conditions.

2.2. *Operando* Surface-Sensitive X-ray Scattering and Spectroscopic Techniques. Bulk X-ray scattering or diffraction has revolutionized the field of crystallography and developed into a standard technique for resolving crystal structures across the physical and life sciences. The use of X-ray scattering for determining surface atomic structures at the electrode−electrolyte interfaces was initially performed to investigate Pb underpotential deposition (UPD) on Ag(111) by Melroy et al.[40] and Cu UPD on Pt(111) in our early work.[41] Later, the first study of interfacial water structure at an electrified Ag(111) electrode was reported by Toney et al. using surface X-ray scattering in the 1990s.[42] Over the past three decades, *operando* surface X-ray diffraction (SXRD) has emerged as a powerful tool to interrogate the atomic-scale surface structural changes during lattice reconstruction/relaxation,[43−45] metal deposition/dissolution,[46] surface roughening/corrosion,[47] molecular/ionic adsorption, and interfacial water structures under electrochemical conditions.[42] SXRD measures the crystal truncation rods (CTRs) including both specular CTR, where the momentum transfer, Q, is along the surface normal direction, and off-specular (nonspecular) CTR in which the Q has additional in-plane contributions. The specular CTR (also referred as extended X-ray reflectivity) is particularly sensitive to the short-range ordering extending from the surface to the electrolyte along the surface normal direction. Combined with the off-specular CTR, the full picture of the three-dimensional surface structural changes can be identified, relative to the underlying bulk crystal surface. For instance, specular X-ray reflectivity of mica(001) (a layered alumino-silicate) showed that the first layer of water has a strong interaction with the oxide surfaces and an oxygen density twice as high as that of bulk water.[48] A strong oscillation in the oxygen density, within 10 Å in the direction normal to the oxide surfaces, suggests an interfacial ordering of water. An in-depth discussion of CTR studies of water/oxide interfaces on metal and oxide surfaces can be found in a recent review.[49] For a comprehensive review on SXRD and CTR measurements, the interested readers are referred to reviews by Lucas and others.[43−46] Here, we present selective examples to illustrate the unique capabilities of the SXRD and CTR techniques and briefly discuss other coupled structural and spectroscopic X-ray techniques.

We recently employed *operando* X-ray reflectivity to measure the specular CTR to study the electrochemically induced surface reconstruction of single-crystal $SrTiO_3$ (Figure 2A).[50] n-Type $SrTiO_3$ is particularly active for photocatalytic water splitting in alkaline media under UV light illumination. The area X-ray detector, optimized for high-energy X-rays (30 keV), enables the extraction of CTR intensities from the background signals (such as diffuse scattering). Absolute X-ray structure factors, $|F|^2$, were obtained at the $SrTiO_3$(001)-electrolyte interphases under precise control of electrochemical conditions (Figure 2A). The CTR measurements of $SrTiO_3$ exhibited significant structural changes when immersed in 0.1 M NaOH and trained under a positive potential (Figure 2B). *Ab initio* joint DFT (JDFT) calculations employed in this work provided an accurate description of the electron density of both the solid surfaces and contacting liquid, which enabled a direct comparison of calculated and measured $|F|^2$ values with no adjustable parameters. Immersing $SrTiO_3$ in 0.1 M NaOH (untrained) yielded a relaxed 1 × 1 double-TiO_2-terminated structure, based on JDFT best fitting results (black curve, Figure 2B). Training the $SrTiO_3$ in 0.1 M NaOH under 0.8 V vs Ag/AgCl (∼1.8 V vs RHE) induced a significant change in $|F|^2$ values, especially between the 001 and 002 peaks (red curve, Figure 2B). JDFT calculations indicated that the most likely structural change was the electrochemically induced formation of an anatase-like (Ti_2O_2) structure (Figure 2C). The anatase-like structure at the surface is oxygen deficient, capped by an OH adsorption layer, which is accompanied by the dissolution of at least one layer of Sr atoms from the surface, leaving a triple TiO_2 termination. This anatase-like surface structure, with an underlying $SrTiO_3$ host possesses an optimal biaxial tensile strain and has a smaller band gap than $SrTiO_3$, which is better matched to the solar spectrum and explains the 2−3 fold increase in water splitting activity after electrochemical training, relative to the untrained counterpart. Another benchmark OER catalyst, RuO_2 single crystals, were investigated by *in situ* X-ray off-specular oxygen CTR, first by Lister and Nagy,[51,52] and then by Shao-Horn, systematically with various crystal orientations in acidic media.[53,54] The position and configurations of O-containing intermediate species (e.g., H_2O, OH, O, OOH, etc.) at different Ru sites were assigned based on the best fitting from DFT simulations. A key intermediate of OOH species on coordinatively unsaturated Ru sites was identified and stabilized by OH_{ad} on neighboring bridge sites. The deprotonation of the OH and the removal of OO were proposed as the rate-determining step. It should be noted that the presence of H atoms is only speculated based on changes in the Ru−O bond lengths in CTR measurements and best fitted configurations from DFT simulations since the X-ray scattering of H atoms is very weak. In addition to the extensive CTR analysis under constant applied potentials, it is possible to investigate electrochemical reaction kinetics in potentiodynamic measurements. By monitoring the scattered X-ray intensity at selective reciprocal lattice positions, the surface structural changes can be directly

https://dx.doi.org/10.1021/acscatal.0c04789
ACS Catal. 2021, 11, 1136−1178

correlated to electrochemical signals during CV cycles.[55,56] This time-resolved CTR method has provided valuable insights into the dynamic CO adsorption on single-crystal metal or metallic alloy surfaces[57,58] and the stability of bimetallic alloys (e.g., Pt_3Ni) under oxidative potentials in acid.[59]

While SXRD serves as a powerful technique for probing structural changes at/near the surface, *operando* X-ray standing waves (XSWs) provide atomic-scale insights on the cross section of solid−liquid interfaces with depth resolution and can simultaneously resolve elemental information when coupled with fluorescence detection or photoelectron spectroscopy. XSWs are generated from the interference between incident X-ray and strong reflected X-ray beams at the Bragg condition (Figure 2D).[60−63] The periods of XSWs can be tuned with layered synthetic microstructures (LSMs) of high-Z/low-Z elements. The scale of LSMs can be adjusted from Å to nm to meet the spatial resolution requirements of experiments, and the incident angle of XSWs serves as a "built-in ruler" which can provide an Å-level vertical resolution. As the incident beam angle is scanned across the strong Bragg reflection, the XSWs scan different atomic layers at the surface, across the electrochemical double layer (EDL), and further extend to the solution layer (Figure 2D). Our early studies employed *operando* XSWs, combined with X-ray fluorescence detection, to investigate the solid/liquid interfaces on Pt/C LSMs under electrochemical conditions.[60] The XSW experiments involved the adsorption of iodide followed by the electrodeposition of copper onto the Pt/C LSMs. As shown in Figure 2E, the maxima in the copper fluorescence yield occurred at a higher incident angle, relative to that of iodide, suggesting that the copper layer is closer to the Pt surface (0.7 Å) than that of the iodide (4.0 Å). Given that the iodide layer was deposited prior to the copper electrodeposition, this provided unambiguous evidence that the iodide layer was displaced by the electrodeposited copper. Since the XSWs can extend well beyond the surface adsorption layer, theoretical fits of the iodide fluorescence yield profiles unveiled a noticeable contribution from iodide in the diffuse layer.[60] The observed depth-resolved iodide distribution can be regarded as a phase transition where iodide in the electrolyte, following a concentration gradient in the diffuse layer, is incorporated into an ordered crystalline iodine ad-lattice on the Pt surface. Additionally, XSWs have been coupled with surface EXAFS to investigate the Cu electrodeposition on Pt (111) in the presence of halides.[61] Recently, Fadley et al. coupled *operando* XSWs with ambient pressure X-ray photon emission spectroscopy (AP-XPS) to investigate the cation distribution in alkaline media on polycrystalline Fe_2O_3 films (∼6 Å surface roughness) deposited on Si/Mo LSMs (Figure 2F).[64] It provided direct evidence that Na^+ was about 4 Å closer to the oxide surface than Cs^+ given that the relative XPS intensity of Na^+ showed a 0.04° positive shift in the incident angle. This observation offered supporting evidence for the cation effect on the ORR activity proposed by Stamenković et al. The lower ORR activity of Pt(111) in NaOH, relative to CsOH, was ascribed to the stronger interaction of Na^+ with OH_{ads}, which could inhibit the movement of reactants and possibly block the availability of Pt sites.[65] Similar cation effects on the HOR activity and CO oxidation kinetics in alkaline media were investigated by Koper et al.[66,67] The limitation of such a study relies on the generation of an ultrathin liquid layer (∼1 nm) so that soft X-rays (∼1 keV) can penetrate it, enabling AP-XPS measurements. In comparison, our previous *operando* XSWs utilized a regular thick electrolyte owing to the use of a high-energy X-ray (9.2 keV).[60] Nonetheless, the *operando* XSWs study described here enables the use of polycrystalline oxide films deposited on LSMs, which clears the restriction of using single-crystal metals or oxides and can have promising and broad applications for studying the EDL on realistic nanosized catalyst surfaces.

Besides the aforementioned surface-sensitive structural X-ray scattering studies, it is worthwhile to highlight recent progress on spectroscopic X-ray techniques and other coupled X-ray techniques, enabling the measurement of ejected photoelectrons. Traditionally, X-ray photoelectron spectroscopy (XPS) requires ultrahigh vacuum (UHV) for soft X-ray to probe surface chemical species. Watanabe et al. developed the electrochemical XPS (EC-XPS) to transfer Pt electrodes, in contact with electrolyte under applied potential, to a UHV chamber and subsequently freeze-evacuate the bulk electrolyte, so that only surface adsorbates remained.[68] Although this EC-XPS method provides information for identifying and quantifying different O-containing species, subtle changes are likely to occur during the sample transfer and may not (and likely does not) reflect real-time changes in the electrolyte. Instead, *in situ* ambient-pressure XPS (AP-XPS) has been recently employed to track the dynamic evolution of O-containing intermediates at an electrode surface under a gas pressure of (1−100 Torr), close to reaction conditions.[69,70] As shown in Figure 2G (left), the electrochemical AP-XPS setup simulates a PEMFC operating in H_2-O_2 mode with Pt/C as both the anode and cathode, which are separated by a Nafion membrane. The gas cell of the AP-XPS is filled with O_2 at ∼1 Torr, and the Pt/C cathode is hydrated by the H_2O migrating from the humidified hydrogen anode. From the O 1s spectra, two types of OH_{ads} were identified at 0.9 V vs SHE. One located at 531 eV is ascribed to hydrated OH_{ads} interacting strongly with H_2O_{ads} through an H-bonded network, and the other at ∼530 eV is nonhydrated OH_{ads} interacting weakly with O_{ads} (Figure 2G, middle upper inset). Combined with DFT and Monte Carlo simulations, the coverage of H_2O_{ad}, OH_{ad}, and O_{ad} was calculated as a function of computed electrochemical potentials vs SHE (Figure 2G, right). H_2O_{ad} is the dominant species at E < 0.65 V, while OH_{ad}, generated from H_2O oxidation, surpasses H_2O_{ad} as the main adsorbed species at E > 0.78 V. The coverage of O_{ad} significantly increases at E > 0.9 V due to the further oxidation of OH_{ad}. The total coverage of OH and H_2O is similar at 0.85 V and sums up to ∼0.6, close to the expected maximum two-thirds coverage for coadsorbed H_2O_{ad} and OH_{ad} in a hexagonal planar configuration on the Pt surface.[71] The nonhydrated OH_{ad}, at potentials close to the reversible potential of the ORR, may enhance the OH_{ad} activity due to its weak interaction with H_2O_{ad}, but possibly give rise to an increased energy barrier for the activation of O_2 to $HO_{2(ad)}$ due to the poor proton conducting pathways at high pH. However, one needs to remain cautious about the insights from AP-XPS since the O_2 gas pressure used here is still three orders of magnitude lower than the typical atmospheric operating pressure and the relatively high humidity (50−100%) in present fuel cell tests.

X-ray spectroscopy and scattering have evolved into two well-established categories of techniques, capable of providing complementary chemical and structural information under electrochemical reaction conditions. Aiming for a more complete picture of the electrocatalysis processes, coupling two or multiple X-ray techniques can take advantage of both

https://dx.doi.org/10.1021/acscatal.0c04789
ACS Catal. 2021, 11, 1136−1178

spectroscopic and structural information acquired simultaneously so as to optimize the use of precious synchrotron beam time.[72] Previously, combining XSWs with XRF or XPS provided chemical information on electrode/electrolyte interfaces with atomic-scale depth resolution (Figure 2D−F). Here, we will illustrate another representative example of combining small-angle X-ray scattering (SAXS) with XAS to illustrate the capability of coupled X-ray techniques for elucidating the degradation mechanism of fuel cell electrocatalysts. Early studies by Meyer et al. employed *in situ* SAXS to quantify the particle size distributions (PSDs) and geometric surface area of Pt nanoparticles during potential cycling.[73,74] They found that higher anodic potentials and longer time periods at high potentials (square/trapezoidal vs triangular potential profiles) would lead to a faster particle size growth, corresponding to a higher oxide coverage after potential cycles. They proposed that the primary degradation mechanism was dissolution of small particles and reprecipitation of dissolved Pt onto larger particles (i.e., Ostwald ripening). Recently, a coupled SAXS and XAS study revisited the degradation process of Pt nanoparticle fuel cell catalysts during potential cycles (Figure 2H).[75] The experiment included the setups for both XAS and SAXS on the same translation table, enabling a facile switch between XAS and SAXS modes within 2 min. Figure 2H (lower left) exhibits the SAXS measurements of PSDs of Pt nanoparticles after potential cycles between 0.5 and 1.5 V vs RHE at 50 mV/s. The average particle sizes grew from 2.4 nm with a narrow PSD to 3.4 nm with a growing tail of larger particles after 250 cycles, following the Ostwald ripening growth mechanism. The surface area calculated from SAXS suggested a 30% loss after 250 cycles, which is consistent with the electrochemical surface area (ECSA) measured from CV profiles. In addition to the SAXS study, the XANES studies provided spectroscopic information on the oxidation state and coordination environment of Pt nanoparticles under the same reaction conditions. The difference in white line intensity of XANES Pt L_3 (often referred to as "$\Delta\mu$" by Mukerjee and Ramaker et al.) can reflect subtle changes in density of unoccupied Pt d orbitals.[76] As shown in Figure 2H (lower right), as the particles grow during 0−250 potential cycles, there is a decrease in $\Delta\mu$ values, suggesting a lower density of unoccupied Pt d orbitals and thus a less oxidized surface, which is consistent with the lower oxide coverage estimated from CV profiles. Larger Pt nanoparticles tend to have a relatively lower oxide coverage due to its weaker interaction with OH, relative to smaller ones. Such a coupled structural and spectroscopic X-ray strategy offers new possibilities to perform thorough investigations of more complex bimetallic alloy or oxide electrocatalysts under realistic fuel cell reaction conditions.

In summary, the use of *operando* X-ray spectroscopy, such as XAS and AP-XPS and surface-sensitive X-ray scattering, such as CTR and XSW, offer a rare glimpse at the dynamic spectroscopic and structural changes of electrocatalytic processes at electrode/electrolyte interfaces. We anticipate that advances in spatially and temporally resolved spectroscopy will further our understanding of the intriguing, yet complex, multimetallic alloy or oxide surfaces. Coupling two or more X-ray techniques provides complementary chemical and structural information under similar reaction conditions and enables resolving the changes in structure, composition, and distribution of interfacial species at charged surfaces, which will contribute to the elucidation of overall electrochemical reaction mechanisms.

3. SCANNING AND TRANSMISSION ELECTRON MICROSCOPY (STEM)

The *operando* X-ray methods described above provide macroscopic-level structural and spectroscopic information on large ensembles of bulk or nanosized electrocatalysts. The recently developed aberration-corrected scanning/transmission electron microscopes (S/TEM), equipped with electron energy loss spectroscopy (EELS) and energy dispersive X-ray spectroscopy (EDX), offer invaluable complementary microscopic-level insights for establishing structure/composition-reactivity correlations of electrocatalysts. STEM with EELS and EDX can provide sub-Ångström spatial resolution (down to single atoms) with a tremendous amount of elemental/compositional information and electronic structure of electrocatalysts. STEM-based characterizations have emerged as an indispensable technique for advancing our understanding of energy materials and their dynamic evolution during electrochemical reactions at the nanometer and atomic scales. In this section, we will review STEM studies of several representative nanosized electrocatalysts and emphasize the correlations between catalyst activity and microstructures and elucidating the catalyst degradation mechanism during fuel cell reactions.

While TEM has been instrumental in the development of solid-state electrocatalysts, historically, TEM characterization of materials in liquids and/or gases has faced a longstanding challenge due to the operational requirement of high vacuum conditions ($\sim 10^{-10}$ bar). With differential pumping apertures around the specimen area, gas pressures of a few mbar could be studied using dedicated environmental TEMs.[77−79] Recent advances in TEM instrumentation and microchips, with thin, but robust, electron-transparent windows, have enabled *in situ*/*operando* liquid-cell and gas-phase S/TEM with nanometer and even atomic-scale spatial resolution in realistic liquid or gas environments under electrochemical conditions. The previous atomic-scale *ex situ* STEM measurements have provided a baseline understanding of nanosized electrocatalysts and necessary guidance for further *in situ* TEM experiments. Later in this section, we will introduce the recent progress as well as challenges of *in situ* liquid-cell and gas-phase environmental TEM for directly visualizing (electro)chemical reactions at electrode/electrolyte interfaces.

3.1. *Ex Situ* STEM Studies of Electrocatalysts at the Atomic Scale. Electrocatalytic reactions are particularly sensitive to the morphology and surface composition of nanosized catalysts, where the electronic structure and atomic arrangement often dictate electrocatalytic performance. A number of notable reviews have summarized the design and development of highly active catalysts, emphasizing the chemical composition, atomic and compositional structures, working environment, and others.[80−82] It is widely recognized that a variety of modern tools are required to fully understand the design criteria and reaction mechanism, among which S/TEM and X-ray based methods are of paramount importance as they provide information at both microscopic and macroscopic levels.[83−85] The improvement in the catalytic activity of precious-metal-based catalysts in acidic media can be divided into two aspects: one strategy relies on enhancing the intrinsic activity via electronic, ligand, and/or strain effects, such as ordered intermetallics, core−shell structures, and shape-controlled octahedral and rhombic dodecahedral nano-

https://dx.doi.org/10.1021/acscatal.0c04789
ACS Catal. 2021, 11, 1136−1178

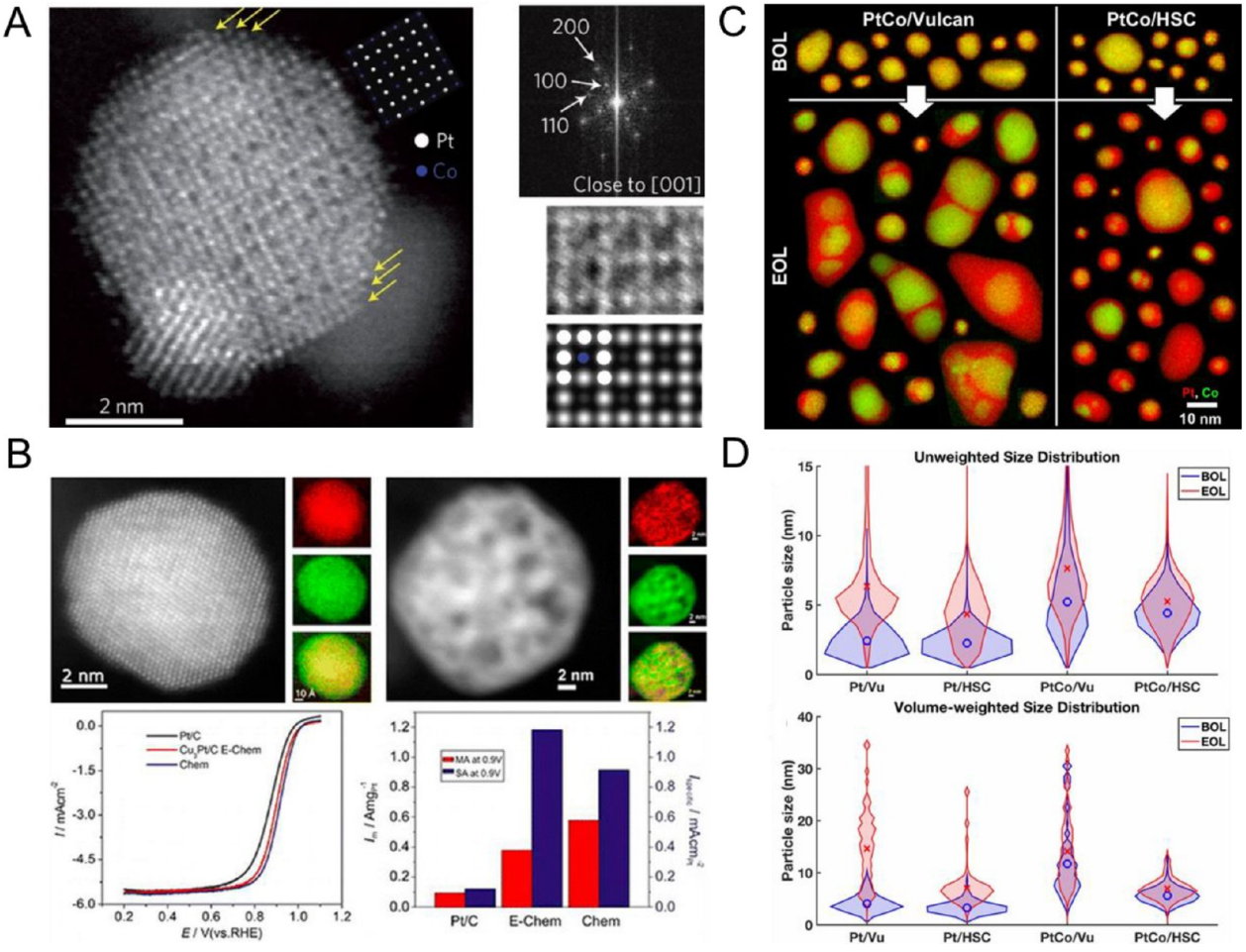

Figure 3. *Ex situ* atomic-scale STEM and EELS characterizations of nanosized electrocatalysts. (A) Left: high-angle annular dark-field (HAADF) STEM image of a Pt_3Co ordered intermetallic nanoparticle annealed at 700 °C, with yellow arrows indicating the Pt-rich shell. A smaller particle (lower left) overlaps the larger particle in projection. The inset shows the projected unit cell along the [001] axis. Right top: Diffractogram of the central particle in left figure. Right middle: A crop of the super lattice feature from right top figure, showing brighter Pt columns at the corners and dimmer Co columns at the center. Right bottom: The simulated ADF-STEM image of $L1_2$ ordered Pt_3Co along [001] by a simple incoherent linear imaging model. (B) Top: STEM images and EELS mapping of Cu_3Pt/C intermetallic nanoparticles after electrochemical/chemical dealloying. Left bottom: ORR polarization curves in 0.1 M $HClO_4$. Right bottom: Mass activity and specific activity at 0.9 V vs RHE. (C) STEM-EELS mapping of PtCo NPs before and after aging. (D) Particle size distribution plots with/without considering volume weighting factor. (A) is reprinted with permission from ref 94. Copyright by the authors 2013 Springer Nature. (B) is reprinted with permission from ref 110. Copyright by the authors 2012 American Chemical Society. (C−D) are reprinted with permission from ref 116. Copyright by the authors 2019 The Electrochemical Society.

particles (NPs). The second is to increase the stable exposed electrochemical surface area (ECSA) by forming highly dispersed NPs or porous nanocomposites. The recent development of alkaline exchange membrane fuel cells (AEMFCs) enables the use of nonprecious metal electrocatalysts for the sluggish ORR in alkaline media.[86−91] Because of its great complexity in microstructures and the identification of active sites, the design strategy for nonprecious metal catalysts is still under active exploration. This includes varying nitrogen-rich precursors and ligands for M−N−C catalysts as well as control over crystal lattice and doping for transition metal oxides. Their crystal, elemental, and atomic structures can profoundly affect the activity and long-term structural stability associated with electrochemical performance during operation. In order to facilitate progress in developing novel electrocatalysts, there are various key steps to consider, regardless of physical and chemical features. The first is to identify the active sites contributing to electrocatalytic activity; the second is systematically tracking their microstructures for a full understanding of the influence of synthesis procedures. Finally, since catalyst structural degradation likely takes place during fuel cell operation, resulting in performance decay, monitoring the structural evolution under applied potentials and establishing correlations with activities, offers valuable guidance for further performance and stability enhancements. We will select several examples to illustrate the capabilities of *ex situ* S/TEM for understanding the structure/activity correlations of electrocatalysts at the atomic scale (*vide infra*).

Significant efforts have been devoted to exploring and understanding the structural descriptors for the challenging ORR in PEMFCs and AEMFCs. Early catalyst studies attempted to correlate ORR activities to electronic structures (d-band vacancies or d-band center), oxygen adsorption energy, or Pt−Pt bond distance (lattice strain), etc. The use of S/TEM and EELS/EDX can provide valuable insights for these structural descriptors and advance our understanding of structure−activity relationships. Early theoretical work by Nørskov et al. suggested that the single most active element,

https://dx.doi.org/10.1021/acscatal.0c04789
ACS Catal. 2021, 11, 1136−1178

Pt, is located at the top of the volcano plot of ORR activity as a function of oxygen adsorption energy and on the volcano plot, the location of Pt is 0.2 eV off from the peak point.[92,93] Stamenković et al. systematically investigated a variety of single-crystal Pt_3M alloys and identified Pt_3Co and Pt_3Ni as two most active catalyst candidates, owing to their optimized downshift of d-band centers (i.e., weakened oxygen adsorption energy), relative to Pt.[36,37] It should be kept in mind that volcano plots are oversimplified models and cannot predict reaction rate nor electrode potentials (kinetics), nor identify the rate-determine step(s). More experimental inputs from *in situ/operando* spectroscopic measurements are required to establish more accurate design rules for optimizing ORR activity. After over a decade of development, Pt−Co bimetallic alloy nanoparticle electrocatalysts have emerged as one of the most active and efficient electrocatalysts for the ORR in PEMFCs. Pt−Co, with different compositions and structures, are nowadays manufactured at scale for practical PEMFC engines in fuel cell electric vehicles. In 2013, we reported on the atomic architecture of Pt_3Co ordered intermetallic NPs, of which the $L1_2$ ordered structure was directly viewed at the atomic scale with HAADF-STEM through the [001] zone axis (Figure 3A).[94] Since the intensity of an annular dark field (ADF) STEM image is proportional to the atomic number ($I \propto Z^{1.7}$), heavier elements exhibit brighter intensity than lighter elements, which provides an opportunity to directly distinguish/identify different elements in bimetallic alloys. In this case, Pt atomic columns, at the corners, appear much brighter than Co atomic columns at the centers, which is fully consistent with the simulated image contrast on the same zone axis (Figure 3A, right medium/bottom). In comparison, commonly used bright-field (BF) TEM or STEM imaging is based on the phase contrast of electrons and is more sensitive to light elements such as C and O, although the image contrast in BF mode is subjected to complications arising from sample thickness variations, tilting, and/or the level of defocusing. For the physical principles of S/TEM imaging and EELS, interested readers are referred to our early review.[95] The diffractogram in Figure 3A (right top) reveals the existence of a (110) peak, which is a characteristic feature only belonging to the Pt_3Co ordered intermetallic rather than the disordered alloy. The identified ordered intermetallic core, surrounded by a 2−3 atomic-layer-thick Pt-rich shell, was found to be responsible for the 2−3-fold increase in activity and enhanced durability for the ORR in acid, relative to the disordered Pt_3Co alloy. Efforts and improvements have been made to optimize the electrochemical activity of Pt−Co NPs, such as introducing N-doped porous carbons and increasing the metal loading on carbon supports to lower the catalyst layer thickness, so as to enhance the mass transport in PEMFCs.[96,97]

Along with Pt−Co NPs, another important family of nanosized ORR electrocatalysts, Pt−Ni alloys, with either specially controlled morphologies/architectures or a rationally designed elemental distribution, has been reported, where STEM, equipped with EELS/EDX, enabled tracking their structural evolution from the synthesis to postannealing treatments. Following Stamenković's report on the extraordinary ORR activity of single-crystal Pt_3Ni (111),[36,37] Strasser, Fang, and others reported on the synthesis of monodisperse octahedral nanoparticles with shape-controlled {111}-bounded facets.[98−100] Pt_3Ni with various morphologies have been reported, including octahedrons, cubes, truncated octahedrons, and nanoframes, with their shapes and lattice structures clearly resolved with S/TEM. Octahedral Pt_3Ni exhibited much higher ORR activity than cubic Pt_3Ni or polycrystalline Pt/C in RDE measurements.[98−100] The construction of solid rhombic dodecahedra with a diverse elemental distribution and later conversion into hollow/excavated nanoframes PtNi were elaborated by Yang et al.,[101,102] benefiting from their extensive STEM studies on the anisotropic growth of alloy nanocrystals.[103] Xia et al. monitored the Pt/Ni elemental ratios at different positions with EDX quantitative analysis,[104] and Shao et al. evaluated various heating conditions on the growth of octahedral Pt−Ni NPs to fully understand the compositional and structural transitions from a spherical Pt core to an octahedral Pt−Ni as the temperature increased.[105] Chattot et al. implemented a combination of S/TEM and EDX to unravel the mechanism and kinetics of the formation of hollow PtNi/C nanoparticles and temporally resolve the formation and growth of nanocrystals.[106,107] Despite the excellent initial ORR activities of these shape-controlled or hollow nanocrystals in RDE measurements, their long-term stability, especially at oxidation potentials at or beyond 1 V, needs to be carefully examined before the implementation in realistic MEA tests in PEMFCs. Preliminary MEA tests of octahedral Pt−Ni nanoparticles by Kongkanand et al. showed a noticeable loss of the distinct shapes and performance decay after short-time tests in PEMFCs.[108,109] The future development of shape-controlled nanosized electrocatalysts relies on improving the morphological/structural stability and especially enhancing the interaction between the nanocrystals and the carbon supports to mitigate the particle aggregation commonly observed for shape-controlled nanocrystals.

The impact of postsynthesis treatments, in particular, the effects of chemical and electrochemical acid leaching and different atmospheres, was comprehensively studied with STEM. Figure 3B compares representative STEM and EELS mapping of $PtCu_3$ NPs undertaking electrochemical cycling and chemical etching processes, respectively.[110] The composite maps of Pt and Cu, as well as the speckle pattern observed from the Z-contrast STEM image, clearly demonstrate that the electrochemical leaching leads to a Pt-rich surface as indicated by the observed greenish shell, while the chemical etching counterpart yields voids and divots with nanoporosity with the appearance of dark dots. The higher mass activity of the chemically treated NPs is likely attributed to the formation of nanovoids with large ECSAs, despite the fact that the loss of Cu counterbalances the benefit of Pt lattice contraction as shown in the lower specific activity, relative to the electrochemically treated counterpart. A recent report by our group showed that the electrochemical dealloying of Pd−Ni or Pd−Mn NPs in acid led to a stable structure with a thin Pd-rich shell, which was highly active and stable during the ORR in alkaline media.[111] These etching processes could improve precious-metal utilization efficiency and, more importantly, leach out the 3d metals in advance of MEA tests to minimize the detrimental impact of dissolved 3d metal ions in contaminating/poisoning the polymer membrane. Similarly, STEM was employed by Strasser et al. for an in-depth investigation of the dependence of nanoporosity on particle size and the gas atmosphere used in an annealing treatment, on the classic Pt−Ni system.[112] The internal structures of particles treated in H_2SO_4 under air and N_2 environments were analyzed with BF-TEM, building the correlation among chemical composition, porosity, and particle size. The threshold of particle size for forming the porous structure,

https://dx.doi.org/10.1021/acscatal.0c04789
ACS Catal. 2021, 11, 1136−1178

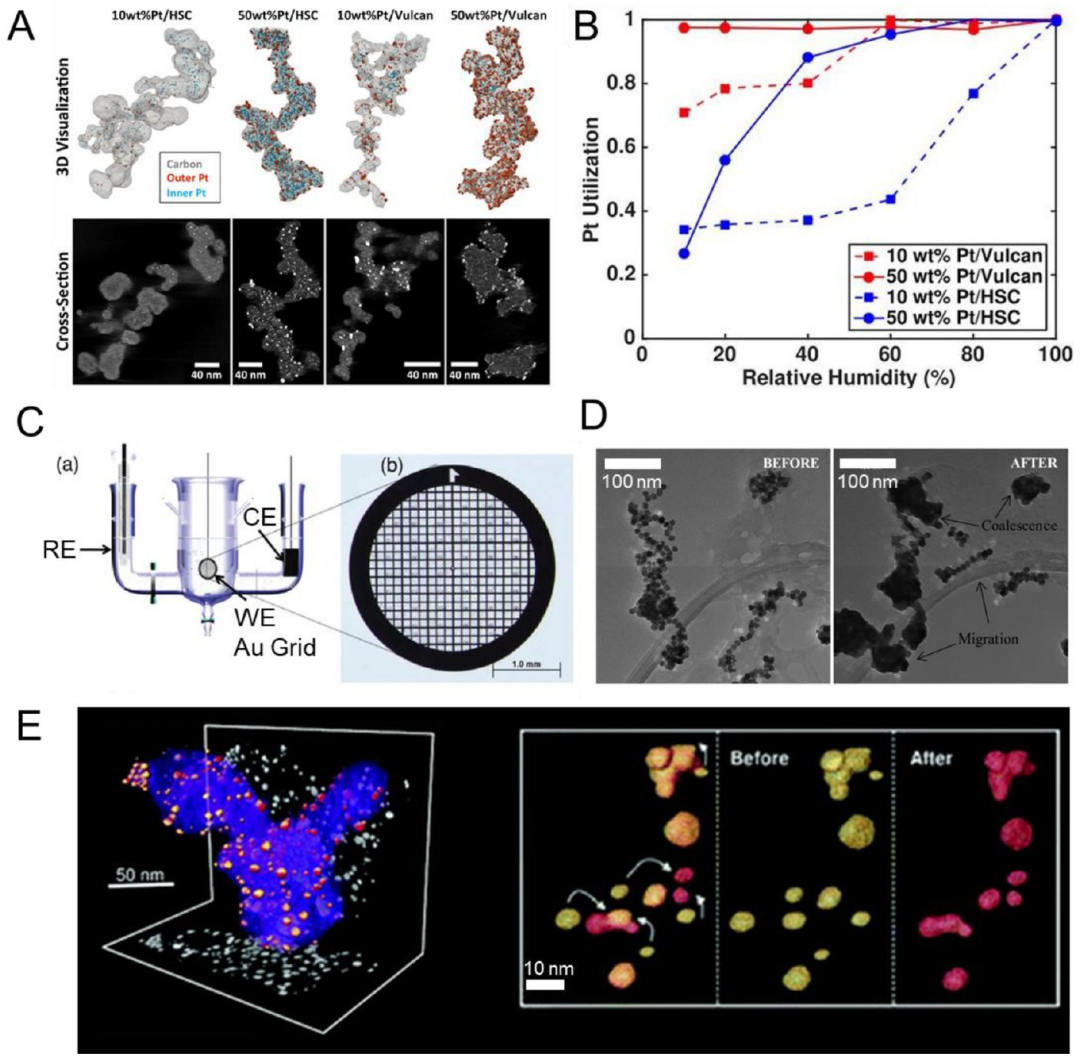

Figure 4. Quantitative STEM tomography and identical-location S/TEM (IL-S/TEM) studies of electrocatalyst degradation. (A) Top: 3D visualizations of carbon supported Pt NPs, with exterior Pt in red and interior Pt in blue. Bottom: Cross sections of 3D reconstructions perpendicular to the imaging axis. (B) Pt utilization with different types of carbon supports and metal loadings measured by CO-stripping in MEAs with varied relative humidity (RH%). (C) Schematic of three-electrode electrochemical cell and the indexed carbon-coated gold TEM grid. (D) IL-TEM studies of hexagonal Pt nanocrystals at the same location before and after the electrochemical aging process. (E) Left: One-to-one correspondence of 3D reconstructed catalyst NPs before (gold) and after (red) electrochemical aging, and its projection on the *x* and *z* directions. Right: Nanocatalyst particle coalescence and migration trajectory indicated by arrows. (A–B) are reprinted with permission from ref 123. Copyright by the Authors. 2018 The Electrochemical Society. (C–E) are reprinted with permission from ref 131. Copyright by the authors 2012 American Chemical Society. (D) Reprinted with permission from ref 132. Copyright by the authors 2015 American Chemical Society.

when treated under air, was determined by TEM while Ni contents were determined by EDX. In contrast, Pt–Ni particles treated under N_2 never showed porosity regardless of the particle size, indicating that the difference in the surface diffusion rate of Pt and Ni with/without the presence of air controlled the potential of forming the porous structure.

In practice, nanosized electrocatalysts are typically assembled in MEAs and can experience substantial changes in structures/compositions and performance degradation after long-term operation. S/TEM continue to play an essential role in elucidating the degradation mechanism, such as Ostwald ripening, coalescence, particle detachments, carbon corrosion, etc.[113−115] To identify the primary degradation mechanism and understand the impact of different carbon supports in MEA performance, we employed STEM-EELS with automated data processing and achieved more statistically robust results by acquiring images and interpreting data from thousands of NPs for each specimen.[116,117] Figure 3C shows a series of STEM-EELS maps of Pt–Co NPs supported on both Vulcan and high-surface-area carbon (HSC), at both the beginning and end of life (BOL/EOL) in MEA cathodes before/after 30 000 trapezoidal voltage cycles between 0.6 and 0.95 V.[116] Ostwald ripening results in an increase in the thickness of the Pt shell, while collisions and coalescence induce multicore NPs, since the original cores will be retained. The STEM-EELS at the BOL/EOL clearly shows that irregular and multicore particles are more commonly observed in Vulcan-supported NPs, while HSC particles are mostly spherical with a thick Pt layer and single core. A statistical analysis of the PSDs, taking the local diameter approximation and volume weighting into consideration, gives violin plots of particle size distributions of Pt and PtCo NPs supported on Vulcan and HSC before and after voltage cycling (Figure 3D). The mean size for BOL and EOL distributions is indicated with blue 'o' markers and red 'x'

https://dx.doi.org/10.1021/acscatal.0c04789
ACS Catal. 2021, 11, 1136−1178

markers, respectively. This methodology allows more comprehensive and practical microanalysis and addresses the traditional limitations of microscopic statistics. Figure 3D in the top and bottom are based on the simple numerical (unweighted PSDs) and volume weighting models (weighted PSDs), respectively. For Vulcan-supported NPs, a growing long tail of large particles is observed, which is more pronounced in plots considering the volume-weighted factor. In comparison, the particle sizes of Pt/HSC and PtCo/HSC maintain a symmetric distribution with a relatively uniform upward shift. The direct and visual evidence from STEM/EELS and statistical particle size distribution with the consideration of volume-weight correlation strongly suggests that coalescence occurs on Vulcan-supported NPs but rarely for HSC NPs, while Ostwald ripening occurs regardless of support. We anticipate that optimization of carbons with rationalized porous networks can be an effective approach to mitigate coalescence and degradation. This microscopic methodology can shed light on the structural and electrochemical stability, over long-term operation, of fuel cell devices.

Besides the nanoparticle electrocatalysts described above, it is worth noting that electron microscopy is indispensable to help identify and visualize catalytic sites, especially for nonprecious metals and atomically dispersed catalysts. For example, Zelenay et al. employed STEM and EELS to unambiguously demonstrate the existence and distribution of single Fe sites on a nitrogen-doped carbon matrix as ORR catalysts in PEMFCs.[118] Recently, we employed STEM and EELS to unambiguously resolve single Fe atoms, as active sites, in an adenosine-derived Fe−N−C nanotube electrocatalyst, which delivered a record high peak power density of ∼500 mW/cm^2 for an M−N−C-type oxygen cathode in AEMFCs.[119] EELS on individual Fe atoms at a low beam voltage of 80 keV avoided the undesirable beam damage and confirmed that bright spots under the STEM must be Fe rather than other trace amounts of impurity heavy elements. STEM-EELS have been employed to investigate the atomic structures of metallic−organic frameworks (MOFs) derived Co−Fe alloys for the ORR in alkaline media, and STEM-EDX analysis has been used to thoroughly investigate their possible degradation mechanisms.[120] The same techniques have also been used to scrutinize the atomic structures of ultralow Pt-loading catalysts on Co−N−C supports to explore the origin of their ORR activity enhancement in acid.[121] These single-atom electrocatalysts have recently gained increasing attention, due to their maximal utilization of metal atoms and great structural tunability from a variety of carbon-based precursors. However, moving beyond just visualizing single metal atoms by STEM, it remains a great challenge to resolve the electronic structures and coordination environment by EELS, with minimal beam damage, and EXAFS can provide complementary structural information in some cases. A recent comprehensive review on single-atom electrocatalysts by Chen et al. can be found in this journal.[122]

Aside from the characterization ability of morphological and elemental identification with two-dimensional information at the atomic scale, STEM tomography enables the direct visualization of the 3D structure and more accurate quantitative analysis of both active nanoparticles and porous carbon supports. For example, we have utilized STEM 3D tomography, under cryogenic conditions to minimize beam damage, to study the distribution of Pt nanoparticles on both the outside and the inside of mesoporous carbon supports. The reconstruction 3D models clearly identify the internal spatial distribution of Pt NPs, as shown in Figure 4A.[123] The 3D segmented tomography of solid carbon and hollow carbon supported Pt NPs with varied loading was gained from the conventional cross-sectioned STEM images shown below. It enables determining the correlation between the morphology of nanosized catalysts, internal pore regions, and pore accessibility. The Pt/C specimens were rotated perpendicular to the optical axis, and the STEM images were acquired over a tilt range of −75° to +75° within every 2° increment, and further reconstructed with their 2D cross-sessions labeled interior Pt in blue and exterior Pt in red (Figure 4A). It is clearly evident that the exterior Pt is dominant for Vulcan, while the majority of Pt is embedded inside of HSC, especially for the high-Pt-loading samples. Coupled with the high-throughput quantitative analysis, the 3D tomography enables the calculation of the specific surface area and interior Pt fraction and demonstrate a consistent trend with electrochemical results. The Pt utilization efficiency shown in Figure 4B at different working conditions further reveals that essentially all Pt NPs are accessible to protons in liquid, while in a low humidity environment, only exterior Pt NPs contribute to the surface catalysis reaction since the narrow pores preclude the infiltration of ionomers, which is crucial for proton transportation.

Its high spatial resolution makes TEM an indispensable tool to study the morphology and 3D structure of electrocatalysts. However, improving the spatial resolution poses an intrinsic limitation on the statistical analysis of inhomogeneous nanosized electrocatalysts, hampering a rigorous comparison of changes at the same location before and after electrochemical reactions. This challenge was circumvented with the introduction of identical location TEM (IL-TEM) such as the early studies by Mayrhofer, Arenz et al.[124,125] The IL-STEM and IL-tomography, although not truly *in situ*, was further developed as a high-throughput and nondestructive method for more rigorous and direct tracking of local structural changes.[126−128] The analysis of the impact of various working protocols and atmospheres on electrocatalysts offers the opportunity to differentiate degradation mechanisms. The left panel in Figure 4C presents an electrochemical cell with an Au TEM grid as the working electrode (WE). Other similar setups were reported in the literature.[129,130] The grid includes labeled and indexed windows, making it possible to perform STEM/EELS and electron tomography on the identical location of samples before and after the electrochemical aging/cycling and learn about the degradation process with one-to-one correspondence from assorted particles. We have employed IL-TEM to investigate the morphological evolution of nanosized electrocatalysts during operation.[131] Nanosized electrocatalysts were loaded on the carbon-coated gold indexed TEM grid prior to the electrochemical experiment, and the potential scan region was limited to 1.4 V, before the oxidation of the Au grid. IL-TEM provided convincing evidence of rapid transformation and agglomeration of shaped-controlled nanoparticles into blunted counterparts and clusters after a few potential cycles. Figure 4D compares the TEM images of a fresh hexagonal Pt nanoparticle sample to that after potential cycles.[131] The loss of hexagonal shapes and coalescence of particles is clearly evident. The morphological transition was also tracked with IL-TEM imaging after every 25 cycles and correlated with CV results, from which it was established that the distinct shapes were lost after first 25 cycles between 0.05

https://dx.doi.org/10.1021/acscatal.0c04789
ACS Catal. 2021, 11, 1136−1178

and 1.3 V. The disappearance of the electrochemical features near 0.37 V, after potential cycles, matches well with the transition of the hexagonal Pt/C to the round, isotropic agglomerates which lose (100) and (111) planes. This study underscores that special attention must be paid to the electrochemical stability of shape-controlled nanoparticles, especially at oxidizing potentials. As shown in Figure 4E, we further employed IL-STEM tomography to analyze the aggregation and movement of individual Pt_3Co NPs during potential cycles between 0.6 and 1.0 V. Figure 4E (left panel) shows the reconstruction tomography of particles before and after electrochemical aging.[132] They are overlapped with fresh NPs labeled in gold and aged counterparts in red. Small movements could be clearly noticed due to the fine alignment enabled by a large set of fiduciary particles. Most of particles were found to stand still, and a few of them migrated, coalesced, and finally merged (Figure 4E, right panel). The comparison of reconstructed images before and after aging enables tracking of particles with the movement path indicated by white arrows, as exemplified in the right panel. These findings point out that particle migration accounts for a larger proportion of the sintering process. More precise conclusions of particle coalesce can be obtained by IL-STEM 3D tomography by excluding possible misleading information caused by merely observing the 2D projected TEM images.

There have been other reports using IL-TEM with different customized setups. Chorkendorff et al. fixed a sample-loaded TEM grid to the end of an RDE glassy carbon disk, which enabled an evaluation of the ORR activity through rotating disk electrode (RDE) measurements.[133] Although the results were qualitative, they provided a straightforward evaluation of different coarsening factors on electrocatalytic activity. Maillard et al. employed an Au TEM grid as the working electrode to enable samples on the IL-TEM grids to undergo the same electrochemical treatments as conventional measurements.[134] They performed a systematic study of the effects of oxidizing, reducing, and neutral atmospheres on the degradation behavior of Pt/C nanoparticles during fuel cell operation. A more practical investigation was conducted by Dekel et al., who compared the degradation mechanism, using IL-TEM, in aqueous electrolytes and solid alkaline exchange membrane (AEM) electrolytes.[135] The latter one is closer to a real/practical working environment, yielding more relevant and representative information. The indexed grid was fabricated in the AEM dry cell, in the absence of water. Unlike in the liquid cell, where Pt/C exhibited severe particle detachment and agglomeration, only mild Ostwald ripening of particles was observed in the dry cells. The results suggest that although liquid electrolyte is commonly employed in RDE measurements to evaluate the aging performance of catalysts candidates, key effects may be overlooked when catalysts are parts of an MEA with humidified gas reactants.

To summarize, IL-TEM has become a critical technique in the field of nanocatalysis due to its unique and irreplaceable functions, as it enables investigating the evolution of nanoparticles during aging tests. By probing the identical zones of particles before, during and after the tests, direct and unambiguous information, about the sequential changes of the particles, can be tracked and analyzed. We anticipate that future developments of the IL-TEM technique will require: (1) specialized and reliable setup and sample holders to allow convenient tests with no electrochemical or mechanical interference; (2) statistics on multiple selected locations to ensure the true representativeness of the system, which may require automated imaging to ensure the efficiency of the experiments. As a class of important supplementary methods to understand electrocatalysts, IL-TEM techniques offer a promising bridge between conventional *ex situ* TEM and challenging *in situ* TEM experiments (*vide infra*).

3.2. *In Situ* Electrochemical Liquid-Cell TEM. Numerous energy-related chemical reactions involve electro-(chemical) processes at solid/liquid interfaces, in general, and electrode−electrolyte, in particular. Electrocatalytic reactions at solid/liquid interfaces are often accompanied by potential-dependent morphological, compositional, and structural changes of the catalysts during operation, which, in turn, play an important role in the electrocatalyst's activity, selectivity, and durability. *In situ* liquid-cell TEM can shed light on the fundamental understanding of electrocatalytic processes and catalyst degradation mechanisms under native environments without freezing or drying the samples. *In situ* liquid cell TEM is well positioned to provide unique insights on the interfacial electrocatalytic process with nanometer-scale, or higher, resolution, composition, and chemical bonding information.[136−141] Optimizing spatial and temporal resolution in liquid-cell TEM needs to consider the strong beam−sample interactions in liquids so as to minimize the beam effect on the (electro)chemical reactions.[142,143]

The pioneering electrochemical liquid-cell TEM work by Ross et al. employed a homemade liquid cell with a two-electrode system to study the electrochemical deposition of Cu clusters on Au via TEM imaging.[136] Recently, *in situ* liquid-cell S/TEM have been used to investigate the stability of nanosized fuel cell catalysts under electrochemical conditions,[144−147] dis/charge mechanisms of electrode materials in lithium ion batteries,[144,148−152] and structural evolution of Cu-based catalysts during the electrochemical reduction of CO_2.[153,154] Liquid cell TEM has been widely used to study beam-induced growth and structural evolution of Pt-, Pd-, and Au-based nanoparticles,[155−159] as well as their corrosion processes in the presence of etching reagents like O_2, halides, or Fe^{3+},[160−162] where, it should be noted, that the electron beam has served as an active reactant and made the reaction mechanisms significantly different from traditional (electro)chemical processes. Liquid cell TEM also has broader applications to the observation of growth and self-assembly of soft materials, such as proteins, polymers, and MOFs.[163−167] Biological samples and many energy materials, such as polymer membranes/ionomers in fuel cells, sulfur cathodes in Li−S batteries, and others, share similar beam-sensitive characteristics, especially when immersed in liquid electrolyte. Thus, the liquid-cell TEM studies of electrocatalysts can benefit tremendously from the extensive liquid-cell and cryogenic TEM studies of biological samples over the past several decades.[167] It is beyond the scope of this review to provide a comprehensive description of all those active areas. The interested readers are referred to the recent book edited by Ross et al.[139] as well as other reviews on liquid-cell electron microscopy.[140,141] Although liquid-cell TEM has been widely used to study chemical phenomena or beam-induced particle growth/corrosion in liquids, very few studies have demonstrated reliable electrochemical results in liquid-cell TEM, which can be compared to standard electrochemical measurements. In this review, we concentrate on *in situ* liquid-cell TEM studies with S/TEM imaging and EELS/EDX spectroscopic capabilities to reliably quantify electrochemical

https://dx.doi.org/10.1021/acscatal.0c04789
ACS Catal. 2021, 11, 1136−1178

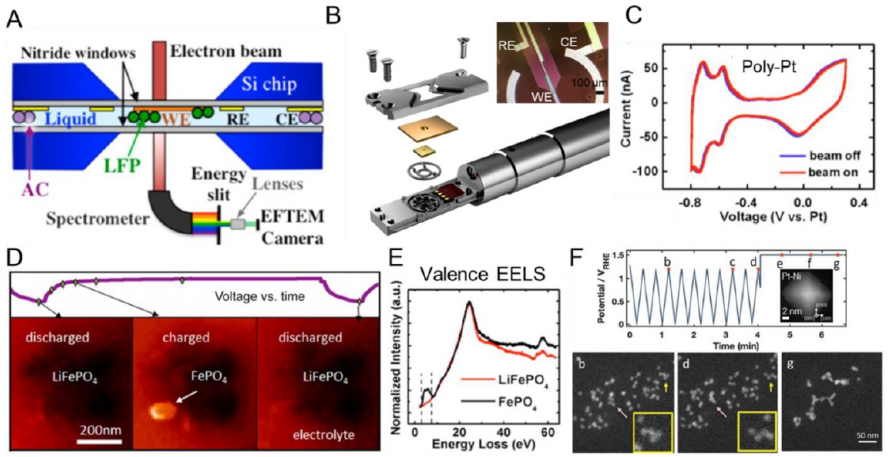

Figure 5. *In situ* electrochemical liquid-cell S/TEM and EELS studies. (A) A cross-sectional view of an *in situ* electrochemical TEM holder with SiN_x windows encapsulating a fluid layer. The working electrode (WE) is made of carbon, while the reference and counter electrodes (RE, CE) are made of Pt. (B) Schematic of the layered structure of a Protochips Poseidon liquid-cell holder. Inset: optical image of the three-electrode microchip loaded with Pt/C nanoparticles (C). CV profiles of polycrystalline Pt films in acidic media when the electron beam is on and off. (D) *In situ* dis/charging processes of the $LiFePO_4$ cathode in 0.5 M Li_2SO_4 solution as shown in the 5 eV spectroscopic EF-TEM images. (E) valence EELS of dry $LiFePO_4$ and the delithiated counterpart $FePO_4$, showing a distinct peak for $LiFePO_4$ but not for $FePO_4$. (F). *In situ* HAADF-STEM imaging of a Pt−Ni catalyst during electrochemical potential cycling between 0.0 and +1.2 V vs. RHE for 20 cycles at 100 mV/s in 0.1 M $HClO_4$, followed by a step into high potential. Panels b−d correspond to the points in the upper panel. Insets in (b−d) show enlarged fractions of particles aligning on their facets. (A, C−E) are reprinted with permission from ref 144. Copyright by the authors 2014 American Chemistry Society. (B) Schematic Copyright of Protochips Inc. Inset Copyright by the authors. (F) is reprinted with permission from ref 145. Copyright 2019 Royal Society of Chemistry.

processes and discuss the major challenges facing rigorous electrochemical measurements in liquid-cell TEM.

Figure 5A presents a cross section of a typical *in situ* liquid-cell TEM with a three-electrode chip and EELS spectrometer for chemical analysis.[144] The electrochemical chip is contained within two electron-transparent SiN_x windows (~50 nm thick), which are able to seal a liquid pocket and withstand the UHV environment inside the TEM chamber and enable a microfluidic flow to constantly supply fresh electrolyte. Figure 5B shows the layered structure of a Protochips Poseidon liquid-cell TEM holder, and the inset shows an optical image of the electrochemical chip we designed with Protochips. The three-electrode configuration follows the design rules of working, reference, and counter electrodes (WE, RE, and CE) in a standard electrochemical measurement. The CE has a large surface area, relative to the working electrode, to enable a rapid polarization, while the RE serves as a stable reference point for measuring and controlling the potential of the WE. The distance between RE and WE is small so as to minimize the IR drop in a sub-micrometer thin electrolyte layer. In the present study, both the RE and CE are made of Pt for its chemical stability and wide application in nanofabrication, while the WE is made of carbon to enable the electron beam to image interesting metal or metal oxide particles with minimal background scattering. In order to show that the customized microchip is capable of yielding well-established electrochemical results, we performed CVs of a Pt film in acidic electrolyte (~500 nm thick), which showed the characteristic behavior of poly-Pt with two pairs of hydrogen adsorption/desorption peaks ({110} facets at −0.75 V and {100} facets at −0.6 V vs Pt) as well as the broad Pt oxidation/reduction peaks (Figure 5C). Negligible changes in CV profiles were detected when the electron beam was turned on, indicating minimal (if any) beam damage effects on the electrochemical measurement, since the CV measurement is extremely sensitive to trace levels of contaminants or changes on the surface or in solution at the submonolayer level. Further thinning the electrolyte (~150 nm) caused significant ohmic drop in the CV measurements, indicating an inherent compromise between the optimal spatial resolution and the quantitative electrochemistry, which presents a great challenge for EELS or EDX analysis in liquids. Thus, it is highly recommended to obtain the well-established CV profiles of Pt before exploring unknown electrochemical redox couples in liquid-cell TEM. A report by Mayrhofer et al. showed that the CV of Pt could be severely interrupted by electrolyte decomposition and Pt redeposition at large beam doses.[140] Zaluzec showed that the electron beam has a significant impact on the open circuit potential (OCP) of the WE in pure H_2O due to capacitive charging of electrode by the beam but a negligible effect in 1 mM H_2SO_4 with sufficient ions to rapidly reach charge equilibrium, indicating that the electrochemical signals should be closely monitored when the beam is turned on.[168] Unocic et al. reported that it is important to have a well-defined electrode geometry and microfluidic conditions, and ensure that the WE is thin (<50 nm) and highly conductive to ensure a uniform current density distribution for quantitative electrochemical measurements.[169,170] One may notice that the potentials in Figure 5C are presented against a Pt pseudo RE, relying on the metastable redox couple of PtO_x/Pt. Given that the position of the characteristic Pt {110} is often located at ~0.1 V vs RHE, we estimate the potential difference between the Pt pseudo-RE and SHE to be about 0.8 V so that an electrochemist's mind can be easily "calibrated" to the commonly used RHE scale. In practice, we notice a potential drift of ~50 mV during extended CV potential cycles, which comes from an intrinsic limitation of the chip design in which all three electrodes are immersed in the same electrolyte, since it is challenging to incorporate a salt bridge to separate the RE from the WE and a glass frit to separate the CE from the WE in the highly confined space of a liquid-cell holder, as commonly used in standard electrochemical measurements. Thus, the potential of

https://dx.doi.org/10.1021/acscatal.0c04789
ACS Catal. 2021, 11, 1136−1178

a Pt RE can drift when the CV measurements change the electrolyte composition and the current at the CE produces trace amounts of soluble hydrogen or oxygen gas, which can diffuse to the RE and alter the nature of the Pt RE to, for instance, Pt−H/Pt (i.e., a Pt RHE). Thus, the lower/upper limits of the CV should be constantly monitored and carefully adjusted, to avoid undesirable hydrogen or oxygen evolution reactions. An active area under investigation is to search for more stable REs to replace the Pt pseudo-RE.

With a rigorous electrochemical analysis established, we performed a liquid-cell TEM study tracking the de/lithiation dynamics of $LiFePO_4$, an important cathode material in Li-ion batteries (Figure 5D). Besides the morphological information provided by S/TEM imaging in liquids, EELS or EDX in liquids can provide compositional and bonding information. EELS was employed in this study since EDX is not suitable for light elements like lithium. Core-loss EELS is widely used to provide chemical fingerprints whereby the incident beam excites a core−electron to unoccupied orbitals above the Fermi level. In comparison, valence EELS (below 50 eV) provides unique electronic structure information by studying the electron interacting with weakly bound outer-shell valence electrons, which surveys the same electronic levels as UV−vis spectroscopy. Core-loss EELS suffers from multiple scattering and can be overwhelmed by the plasma peak of the liquid when the liquid thickness is more than 2−3 mean free paths (200−300 nm), making it practically impossible to analyze in electrochemical liquid-cell TEM with a ∼500 nm thick liquid layer. In contrast, the valence EELS can tolerate liquids up to 6−7 mean free paths (600−700 nm) given its large scattering cross sections and low background from the liquid plasmon peak. An in-depth discussion of EELS in liquids can be found in the work by Holtz et al.[146] As shown in Figure 5E, the valence EELS of delithiated $FePO_4$ exhibits a pronounced feature at 5 eV, which is not present in the lithiated $LiFePO_4$. This peak enables a quick spectroscopic mapping of the state of lithiation, indicating the depth of dis/charge. In addition, UV−vis, together with JDFT calculations, identified a unique feature at ∼6 eV as belonging to $LiSO_4^-$, which can be used to track the concentration gradient of the Li_2SO_4 electrolyte. Thus, energy-filtered TEM (EF-TEM) images with a window of 2.5−7.5 eV are capable of monitoring the dynamic lithium distribution in both the electrode and electrolyte. During the charging process, a bright nanoparticle was detected in the 5 eV EF-TEM at a dose rate of ∼500 e/(nm^2·s), corresponding to a delithiated $FePO_4$ nanoparticle. Other nearby particles were overall brighter than discharged states, indicating a partially delithiated state (Figure 5D, lower left/middle). The 5 eV EF-TEM image in the solution region also showed brighter intensity after the charging process, corresponding to the formation of $LiSO_4^-$. During the discharging process (Figure 5D, lower middle/right), the bright particles disappeared due to the formation of $LiFePO_4$, and the surrounding solution also showed lower intensity due to the depletion of $LiSO_4^-$ and Li^+. $LiFePO_4$ nanoparticles exhibited great structural inhomogeneity and two competing lithiation mechanisms, core−shell and anisotropic growth, could occur in parallel. This study represents a general approach to employ *in situ* liquid-cell S/TEM and EELS to perform rigorous electrochemical measurements and provide valuable insights on the dynamics of charge/ion transfer kinetics at electrode/electrolyte interfaces.

In situ electrochemical liquid-cell TEM has provided important clues for the stability of fuel cell catalysts under electrochemical conditions.[145,147] As previously discussed in the IL-TEM study (Figure 4D), it is critical to understand the structural stability of shape-controlled nanocrystals before their implementation in realistic fuel cell devices. The activation and degradation processes of octahedrally shaped Pt−Ni alloys (Figure 5F, inset), a family of highly active ORR electrocatalysts in acidic media, were investigated using the *in situ* electrochemical liquid-cell TEM. The structural stability of both the catalysts and carbon supports can face significant challenges at high oxidation potentials, which can occur in the startup/shutdown conditions in PEMFCs, reaching potentials as high as ∼1.6 V vs RHE due to the existence of H_2/air interface at the anode side.[115] Figure 5F shows the time-resolved morphological changes of the octahedral Pt−Ni NPs (∼8 nm) as a function of potential cycles. During CV cycles between 0.05 and 1.2 V vs RHE, mild particle coalescence and aggregation were observed (panels b and d). An aggressive potential hold at 1.4 V for several minutes led to severe particle motion and aggregation (panel g), which is likely due to the oxidation and corrosion of carbon and which can induce the detachment of particles from the weakly bound carbon supports. The shape-controlled NPs, including those in the present study, are often loaded on carbon supports after their synthesis, rather than being directly grown onto it, resulting in weak catalyst−support interactions, when compared to the intimate catalyst−support interactions that arise from impregnation methods. Previously, we performed an *in situ* electrochemical liquid-cell TEM study of Pt_3Co nanoparticles on carbon supports synthesized by an impregnation method, where only mild particle coalescence was observed, despite significant carbon corrosion at high potentials.[147] Similar mild catalyst coalescence and carbon corrosion were also observed in Pt−Fe alloys prepared by impregnation methods.[171] Those *in situ* liquid-cell TEM studies offer an important lesson about reducing the surface mobility of catalyst nanoparticles by enhancing particle-support interactions. Several strategies have been proposed to mitigate these issues, such as enhancing the chemical interactions by doping carbon with foreign elements (e.g., nitrogen),[96] and designing porous carbon structures for confining the particle motion and increasing the contact area for nanoparticles. For instance, Figures 3C and 4A demonstrate that the Ketjen Black-based HSC carbon can significantly mitigate Pt_3Co particle coalescence/aggregation and confine the particle in its highly rich interior mesopores, compared to the traditionally used less porous solid Vulcan-type carbon, in MEA tests. Designing corrosion-resistant support materials to replace carbon and oxidation-resistant alloy catalysts will be key to developing electrocatalysts for long-term fuel cell operation.

Electrochemically induced structural evolution offers a highly controlled strategy to tune the nucleation and growth kinetics of nanocrystals and can yield single-crystal NPs with a variety of low and high-index facets,[172] Although the structural evolution mechanism and stability of shape-controlled nanocrystals, before/after electrochemical treatment, have been explored by IL-TEM as shown in Figure 4C−D, the time-resolved dynamical changes of electrocatalysts are largely unknown and call for the use of *in situ* liquid-cell TEM methods. A notable example is the dynamic structural evolution of Cu-based electrocatalysts during the electrochemical reduction of CO_2, such as from irregular Cu nanocrystals to well-defined nanocubes with (100) facets, which results in a dramatic increase in selectivity for ethylene, a

https://dx.doi.org/10.1021/acscatal.0c04789
ACS Catal. 2021, 11, 1136−1178

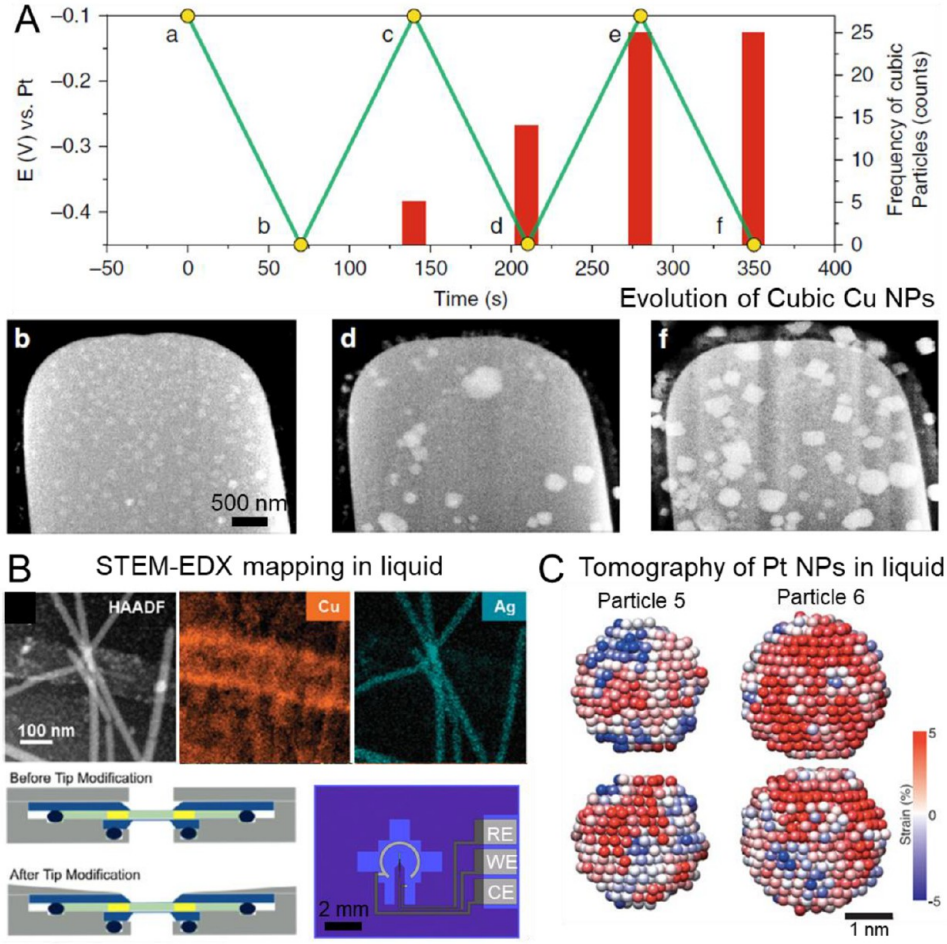

Figure 6. *In situ* electrochemical liquid-cell S/TEM, EDX mapping, and tomography in liquids. (A) *In situ* STEM imaging of the growth and morphological evolution of Cu_2O nanocubes in CO_2-saturated 0.1 M $KHCO_3$ solution. (B) HAADF-STEM-EDX mapping of nanocomposites in water (~200 nm thick). Lower left: The tip modification necessary for X-rays to reach EDX detector. Lower right: The perpendicular configuration of the WE, optimizing the viewing area for EDX detector. (C) 3D atomic-scale strain maps of ligand-coated Pt NPs in a graphene-encapsulated static liquid cell. (A) is reprinted with permission from ref 153. Copyright 2020 Springer Nature. (B) is reprinted with permission from ref 178. Copyright 2014 Royal Society of Chemistry. Lower right panel: Copyright of Protochips Inc. Panel (C) is reprinted with permission from ref 179. Copyright 2020 American Association for the Advancement of Science.

valuable chemical feedstock, over methane.[173−176] Figure 6A shows an *in situ* liquid-cell TEM study of the electrodeposition of cubic copper oxide (Cu_2O) from $CuSO_4$ solution and its subsequent morphological evolution during potential cycles in CO_2-saturated $KHCO_3$ solution in the presence of chloride.[153] At the beginning, both cubic and noncubic NPs were observed (Figure 6A, panels b and d). With extended potential cycling, the fraction of cubic NPs progressively grew as shown in the red histogram and panel f, while noncubic NPs electrochemically dissolved during the positive-going scans. Analysis of nanoparticle growth at different potentials during the CV cycles suggests that cubic Cu_2O achieved an average particle size of ~400 nm after several potential cycles. Control experiments, in the absence of chloride, indicated that chloride was necessary for the formation of cubic Cu_2O by stabilizing the {100} facets against oxidative dissolution while {111} and {110} facets experienced faster dissolution under the same conditions. Treating the electrochemically prepared Cu_2O cubes at the more negative potential of −0.7 V vs Pt RE, led to the transition from cubic to an irregular needle-like morphology. Interestingly, a recent liquid-cell TEM study by Yang et al.[154] reported the transformation from irregular Cu NPs (~7 nm) to cubic Cu_2O (~20 nm) under a negative biasing potential of −0.6 V vs carbon pseudo-RE in 0.1 M $KHCO_3$, in the absence of chloride, while a larger Cu NP precursor (15−20 nm) did not undergo similar morphological changes under the same conditions. These two *in situ* liquid-cell TEM studies reveal that the starting precursors (solution or Cu NPs), electrochemical testing protocols (triangular or constant potentials), and electrolyte composition all have a significant impact on the final morphology and structure of the electrochemically shape-selected nanocrystals.

Finally, two recent reports are highlighted here to illustrate the latest technical breakthroughs in the development and application of *in situ* liquid-cell TEM. Having discussed the significant challenges facing EELS analysis in Figure 5E, it is realistic to perform EDX elemental analysis in liquids due to the high penetration depth of X-rays. Figure 6B presents STEM-EDX elemental maps of nanocomposites of Cu, Ag and other elements. An EDX spatial resolution of ~15 nm was reported by Zaluzec et al. in a liquid thickness of ~200 nm.[177,178] Ultimately, the liquid thickness needs to be optimized to enable the proper electrochemical reactions. In addition, the EDX spatial resolution is limited primarily by the

https://dx.doi.org/10.1021/acscatal.0c04789
ACS Catal. 2021, 11, 1136−1178

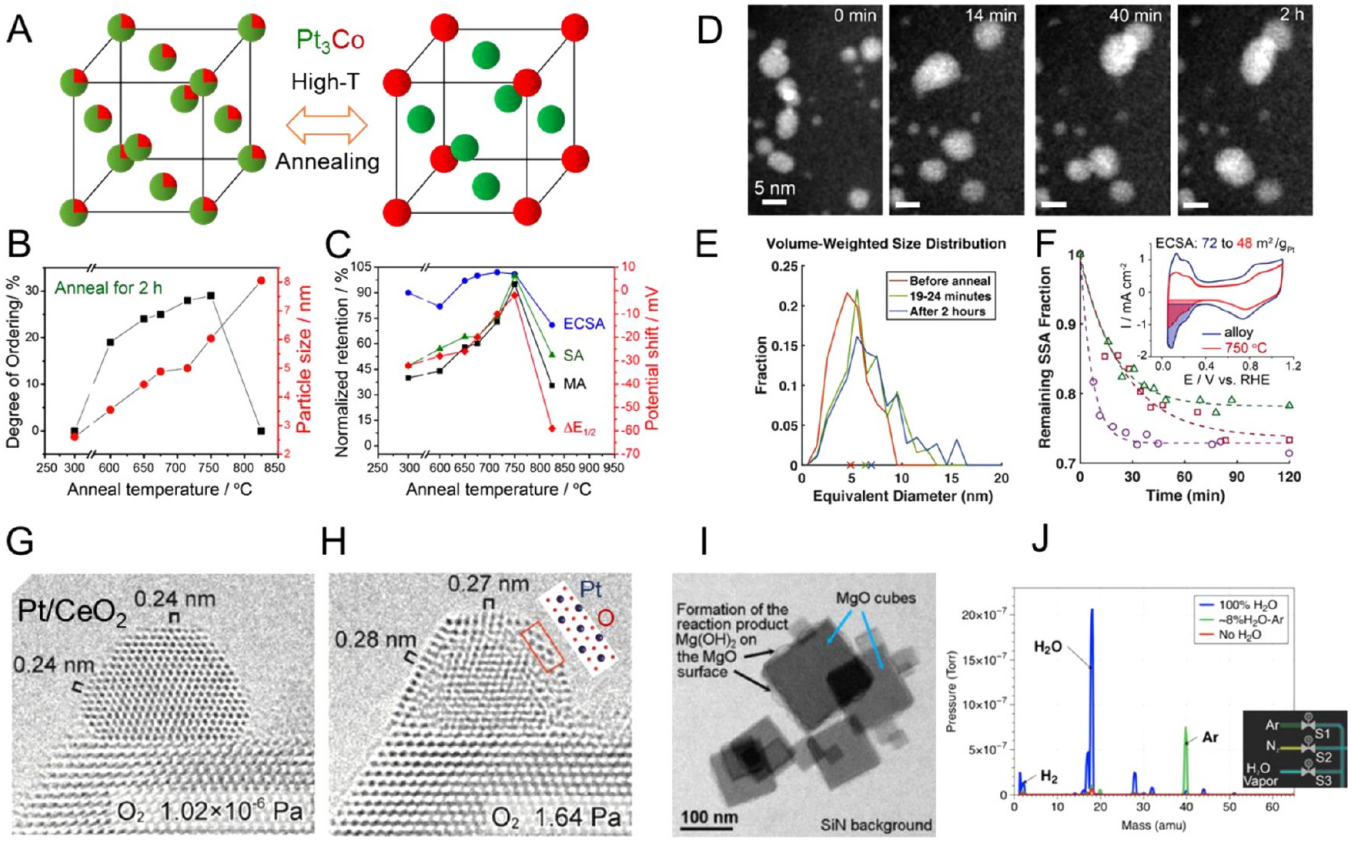

Figure 7. *In situ* environmental S/TEM under controlled temperatures and gas phases (A) Schematic of the disorder−order phase transition of Pt_3Co under high-temperature annealing. (B). The degree of ordering and domain size of Pt_3Co NPs, quantified by *in situ* heating XRD, as a function of the annealing temperature (C) The durability of Pt_3Co/C catalysts in terms of the retention of MA, SA, ECSA as well as the half-wave potential shift after 2000 CV cycles from 0.6 to 1.0 V vs RHE in 0.1 M $HClO_4$. (D) In situ heating STEM tracking of the morphological changes of Pt_3Co/C at 750 °C, showing particle migration and coalescence during a 2 h annealing process. (E) Volume-weighted particle size distribution of thousands of Pt_3Co NPs, reflecting the relative contribution of larger particles more clearly. (F) Relative SSA loss of Pt_3Co estimated from STEM images of three different regions during annealing. Inset shows the ECSA of Pt_3Co/C before and after annealing, measured from CV profiles. (G−H) In situ gas-phase atomic-scale HR-TEM images of Pt/CeO_2, showing the surface oxidation at elevated oxygen pressure. Inset shows the crystal model of α-PtO_2 (I−J) BF-STEM image of cubic MgO crystals with surfaces covered by $Mg(OH)_2$ after exposure to flowing water vapor at ∼16 Torr at 250 °C. (J) Comparison of mass spectra of the gas cell with/without ∼16 Torr water vapor and ∼8% H_2O in air at room temperature. Inset shows gas lines built for mixing different types of gases. (A−F) are reprinted with permission from ref 205. Copyright by the authors 2019 National Academy of Sciences. (G−H) are reprinted with permission from ref 220. Copyright 2014 Royal Society of Chemistry. (I−J) are reprinted with permission from ref 222. Copyright 2020 Microscopy Society of America.

maximum beam dose allowed to avoid beam damage. Achieving a high-quality EDX map will require the redesign of the liquid-cell holder and electrochemical chip. As shown in the lower panels of Figure 6B, the holder tip needs to be modified to overcome the shadowing problem and enable the X-rays to reach the EDX detector at a normal tilting angle of ∼30°. The viewing window for the WE ("line of sight") will need to be adjusted from a parallel to perpendicular configuration, relative to the holder direction, to maximize the WE area accessible to the EDX detector (Figure 6B, lower right). It is equally important to equip the STEM with a dual or quadruple EDX detector with a large solid angle of 0.5 Steradian or above, in order to lower the beam dose and acquisition time to avoid or minimize beam damage. With the continuous development of EDX instrumentation and liquid-cell holders, it is reasonable to anticipate that *in situ* liquid-cell STEM-EDX will be capable of resolving the dynamic changes in chemical composition(s) under working electrocatalytic conditions. Finally, while the aforementioned flow-type liquid-cell TEM (Figure 5A) provides invaluable insights into nanometer-scale chemical dynamics, it is often very challenging to achieve atomic-scale resolution in a liquid layer whose thickness ranges from 100 to 500 nm. A recent study by Ercius and co-workers demonstrated the atomic-scale 3D tomography of Pt NPs in a static liquid cell encapsulated by two thin graphene sheets.[179] The tight sealing of Pt NPs in a liquid pocket (a few nanometers) can be achieved by the strong interactions between the two graphene sheets, which minimizes the electron scattering by the liquid or graphene window and enables atomic-scale resolution. As shown in Figure 6C, 3D strain maps of two Pt nanoparticles, based on precise measurements of interatomic distances in 3D tomography, exemplify the structural complexity of ligand-coated nanocrystals synthesized by the widely used colloidal method. It shows, in three dimensions, that the surface of Pt NPs can have a compressive or tensile strain at different locations as well as internal defects and gain boundaries. The nonuniform coating of polyvinylpyrrolidone (PVP) ligands was proposed to induce localization of electron density around the surface Pt atoms and thus cause local deviation of the atomic

https://dx.doi.org/10.1021/acscatal.0c04789
ACS Catal. 2021, 11, 1136−1178

lattices and surface strain. The static liquid-cell STEM approach offers the possibility of performing atomic-scale STEM imaging, spectroscopic analysis in liquids (as commonly used in a vacuum) and complementary information down to the nanometer-scale in electrochemical liquid-cell TEM studies.

In summary, *in situ* electrochemical liquid-cell TEM is a fasting-growing technique that is providing unprecedented time-resolved information on dynamic changes in morphology, structure and composition of electrocatalysts under reaction conditions. Liquid-cell TEM will continue to enable us to explore new frontiers in electrochemistry, such as reaction kinetics at elevated temperatures[180] and imaging electrochemical polymerization process.[181] Further development on liquid-cell TEM will continue to improve the spatiotemporal resolution for tracking fast reaction kinetics using newly developed electron detectors with fast readout and enhanced electron sensitivity for low-dose STEM.[182,183]

3.3. *In Situ* Environmental TEM under Controlled Temperature and Gas Phases. Environmental-TEM (E-TEM) enables the *in situ* study of the dynamical behavior of nanosized (electro)catalysts under controlled temperature and gas environments.[184,185] Traditional E-TEM involves a dedicated differential pumping system to study catalysts under a mTorr-level pressure or lower and medium temperatures.[186,187] More recently, *in situ* gas-phase S/TEM techniques have returned to an early approach of employing a flow-type gas cell encapsulated by thin and robust SiN_x windows, similar to the design of liquid-cell holders in Figure 5A. The *in situ* gas-phase S/TEM enables the study of nanoscale catalysts during reaction conditions under a variety of gas environments at temperatures up to 1000 °C and pressures up to 1 atm. Since the electron beam is scattered much less in gases than in liquids, *in situ* gas-phase environmental TEM enables the use of regular STEM and EELS to achieve atomic-scale spatial resolution with minimal impact due to beam damage. Such studies can provide valuable insights and guidance for the design, synthesis, and mechanistic understanding of catalysts for a variety of gas-phase (electro)catalytic reactions, such as hydrogen fuel cells and ammonia production. *In situ* heating TEM under variable gas environments has provided new information on the thermal stability of Pt-based catalysts,[188−191] surface reconstruction and elemental distribution of Pt-based catalysts under O_2, H_2 or CO,[192−195] shape and facet evolution of metal nanoparticle catalysts,[196−198] and 3D tomography of *in situ* structural evolution[199−203] Recently, *in situ* gas-phase STEM-EDX was able to distinguish elemental segregation and surface reconstruction of bimetallic alloys, such as Pd−Cu alloys during catalyst activation and operation.[204] Here, we will select three examples to illustrate the recent progress on *in situ* heating and gas-phase TEM for electrocatalysts.

Pt-based intermetallics exhibit superior electrocatalytic activity, particularly for the sluggish ORR in PEMFCs. As-synthesized, Pt-based metal alloy NPs generally form as disordered alloys, which suffer from a rapid loss of activity during electrochemical cycling due to the dissolution of the non-Pt element and subsequent changes in both the particle morphology and crystal structure. After postsynthesis annealing at high temperatures, the disordered alloy can be transformed into the ordered intermetallic phase, which can show significantly enhanced durability and activity,[205−219] as shown in the example of Pt_3Co in Figure 7A.[205] It is critical to understand the order−disorder phase-transition behavior of nanocrystals, which will enable us to develop better annealing protocols to increase the degree of ordering of the NP catalysts and, by extension, boost fuel cell performance. We employed *in situ* heating TEM, together with *in situ* heating XRD, to quantify the degree of ordering in Pt_3Co nanoparticles, for the first time, and study the order−disorder phase transition and morphological changes during real-time high-temperature annealing (Figure 7A−F). *In situ* heating, synchrotron-based XRD was performed to investigate the impact of a variety of annealing conditions on the degree of ordering of large ensembles of Pt_3Co NPs based on the characteristic {110} ordering peak, which only exists in the ordered intermetallic phase, not in the disordered alloy (Figure 7B). As the temperature was increased from 600 to 750 °C, the degree of ordering increased progressively and reached the maximum level of ∼30%, indicating ∼1/3 of the Pt_3Co NPs had transformed to the ordered intermetallic while the rest (2/3) remained as disordered alloys. As the temperature was further increased from 750 to 800 °C, the degree of ordering dropped sharply to zero since the disordered phase is a more stable phase once the temperature passes beyond the order−disorder phase transition temperature (ODPT), based on the phase diagram. Monte Carlo simulations suggest that smaller particles tend to have a lower ODPT and thus are prone to lose their ordered structures at temperatures higher than that for larger particles, which is consistent with the correlation between higher degree of ordering and larger particles when temperature is below 750 °C (Figure 7B). Comprehensive stability measurements in RDE suggest a strong positive correlation between a higher degree of ordering and more durable electrocatalysts in all performance metrics, MA, SA, ECSA retention and the half-wave potential shift (Figure 7B,C). *In situ* heating STEM was employed to directly visualize the morphological changes (Figure 7D). Significant particle collisions and coalescence on the carbon support were also observed, with some particles moving by over 10 nm and experiencing pronounced particle size growth. In contrast, several ∼2 nm particles remained fixed near their initial positions with little/no noticeable change in size throughout the experiment. This observation argues against Ostwald ripening as a significant contributor to particle coarsening. Figure 7E exhibits the volume-weighted PSDs of thousands of Pt_3Co NPs, using an automated algorithm, showing that the larger particles account for a significant fraction of the Pt_3Co volume, potentially responsible for the loss of ECSA. The relative Pt_3Co specific surface area (SSA) loss was calculated to be ∼33% based on STEM images, which is consistent with the loss in electrochemical surface area (ECSA) measured by cyclic voltammetry (CV) (Figure 7F, inset). STEM images confirm the formation of both fully and partially ordered NPs at the atomic scale. The annealed Pt_3Co/C nanoparticles, with an optimal degree of ordering achieved at 750 °C, exhibited significantly enhanced durability with <5% loss in power density at 0.67 V, relative to 15% loss for the disordered alloy, after 30 000 potential cycles in MEA tests. The results highlight the importance of understanding the annealing process to optimize electrocatalytic activity. *In situ* heating TEM enabled the direct visualization of nanoparticle growth and coalescence, the quantitative analysis of surface area, and the formation of both fully and partially ordered nanoparticles at the atomic scale. This strategy of combing *in situ* heating STEM and *in situ* heating XRD highlights the importance of

https://dx.doi.org/10.1021/acscatal.0c04789
ACS Catal. 2021, 11, 1136−1178

close coupling between two techniques at different length scales for better understanding of the structure−activity relationship(s) of electrocatalysts.

Figure 7G−H present an example of *in situ* gas-phase TEM studies of the dynamic oxidation and reduction of Pt NPs supported on a CeO_2 substrate (Figure 7G,H).[220] Takeda et al. resolved the atomic-scale HR-TEM image of the Pt NPs, which remained stable under a very low O_2 pressure of 10^{-6} Pa at a dose rate of $\sim 10^5$ e/(nm^2·s) (Figure 7G). The surfaces of the Pt NPs were oxidized as clearly evidenced by the expansion in lattice *d*-spacings, which is consistent with the theoretical values of α-PtO_2 (Figure 7H and the simulated model in the inset). It is interesting to note that the surface Pt oxides could be reduced readily by CO as well as the electron beam in a vacuum, indicating the non-negligible beam irradiation, which could be mitigated by employing a lower dose rate of $\sim 10^3$ e/(nm^2·s). The surface oxidation process of Pt NPs could be suppressed in the presence of water vapor, which was attributed to the generation of reducing species such as H_2 produced by beam irradiation. Another gas-phase TEM study, by the same group, on Au NPs during the CO oxidation process, showed that the atomic-scale CO-induced surface reconstruction preferentially occurred at {100} facets while leaving the {111} facets intact. These studies illustrate the capability of gas-phase TEM for capturing atomic-scale structural changes, while underscoring beam effects on the structural stability of nanosized catalyst surfaces.[221] Furthermore, in a recent development, an *in situ* gas-phase TEM was coupled to an online mass spectrometer (MS) for analysis of trace amounts of a variety of gas products (ppm-level), which can be tremendously valuable for many electrocatalytic reactions, such as the electrochemical reduction of CO_2 or N_2, as well as the oxidation of alcohols or NH_3, etc. Figure 7 I,J features a very recent study by Unocic et al. on a model system of cubic MgO crystals and their transition to $Mg(OH)_2$ under controlled relative humidity (RH%) and temperatures.[222] The RH% could be adjusted from 2% up to 100% at a pressure of ∼17 Torr, and the temperature could be controlled from 25 up to 900 °C in the presence of water vapor. Figure 7J shows that the online coupled MS is able to distinguish water vapor in a mixture with Ar, using H_2 as the carrier gas. Despite still being at an early stage, the MS-coupled *in situ* gas-phase TEM shows the potential to simultaneously investigate the structural and spectroscopic changes of (electro)catalysts with STEM-EELS and detect gas/volatile reaction products with an online MS. For instance, *in situ* gas-phase TEM can simulate the practical working environment of an MEA by supplying both hydrogen and oxygen fuels under controlled humidity and temperatures.[223]

In summary, the strategy of using *in situ* gas-phase STEM, coupled with EELS/EDX and online MS, could serve as a generalized platform to better understand reaction mechanisms of a variety of heterogeneous catalysts at gas/solid interfaces. The combination enables the investigation of the morphological, compositional, and structural changes of catalysts and establish structure−activity correlations, at the atomic scale, which would, in turn, provide guidance for the deliberate design of high-performance electrocatalysts. High energy synchrotron-generated X-rays can penetrate electrocatalyst samples with μm-to-mm thickness while electron beams are most useful for analyzing samples thinner than 1 μm. For both high-energy X-rays and electrons, it is critical to minimize the beam damage, so as to probe the dynamic structural/compositional changes without affecting the measurements. While X-rays interact more weakly with the sample, they interact more weakly for both useful imaging events, and harmful damaging events. For imaging, what matters is the ratio: X-rays produce a level of beam damage (inelastic scattering events) per useful elastic scattering event, that is 1−2 orders of magnitude higher than that for electrons across all wavelengths and energies.[167] This becomes a problem at high spatial resolution, where the imaging resolution is dose-limited by counting statistics. Thus, X-rays and electrons can serve as complementary techniques to resolve the dynamics of electrocatalytic reactions at different length scales.

4. SCANNING ELECTROCHEMICAL MICROSCOPY (SECM)

Scanning electrochemical microscopy (SECM) is beginning to see use outside dedicated electrochemistry groups. The instrumentation is comparatively simple, inexpensive, and commercially available, while the technique offers unique and powerful functionality for electrocatalysis applications.[224−226] The idea for a scanning electrochemical probe was conceived by Bard and co-workers in 1986, inspired by their work on STM in a liquid environment.[227] They realized that by controlling the probe and substrate potentials independently (akin to ring-disk measurements), interfacial reactions at the substrate electrode could be measured by electrochemically detecting reaction products at the probe. This is known as the substrate generation tip collection (SG/TC) mode of SECM. The next step in the development of SECM was the feedback mode (FB).[228] The FB mode relies on a chemical mediator (kinetically facile redox couple added to the electrolyte) to facilitate communication between the probe and the substrate. As the probe to substrate separation distance decreases, the current at the probe is affected by the nature of the substrate. In the case of an insulating, inactive substrate such as glass, the current decreases (negative feedback) because the substrate blocks the diffusion of the mediator to the probe. This response is often used for probe positioning and topographical imaging. In the case of a conducting substrate such as platinum, the current increases (positive feedback) because nonlocal electron transfer regenerates the mediator at the substrate. In an intermediate case, adsorbates on the substrate can be titrated by the mediator, giving an initial positive feedback followed by a negative feedback response as adsorbates are depleted.[229] This notable advancement in SECM, known as the surface interrogation mode (SI-SECM), allows the quantification of reactivity and coverages of reaction intermediates on catalytic surfaces.[230]

Any quantitative experimental technique needs a solid theoretical and mathematical foundation. While analytical expressions exist to model feedback theory and current−distance curves,[231] increasingly complex SECM experiments in recent years utilize finite element analysis software such as COMSOL Multiphysics for modeling the physics of the SECM experiment to aid in the understanding of experimental results and extract quantitative information.

4.1. Fundamentals of SECM. SECM is a form of scanned probe microscopy. The instrumentation of SECM consists of a probe (or tip) electrode, a bipotentiostat to control the probe and substrate potentials independently, micropositioners to scan the probe in *xyz* directions, and a computer to control the system. Typically, a 4/3 electrode electrochemical cell is used (WE: probe, second WE: substrate, CE and RE) with an

https://dx.doi.org/10.1021/acscatal.0c04789
ACS Catal. 2021, 11, 1136−1178

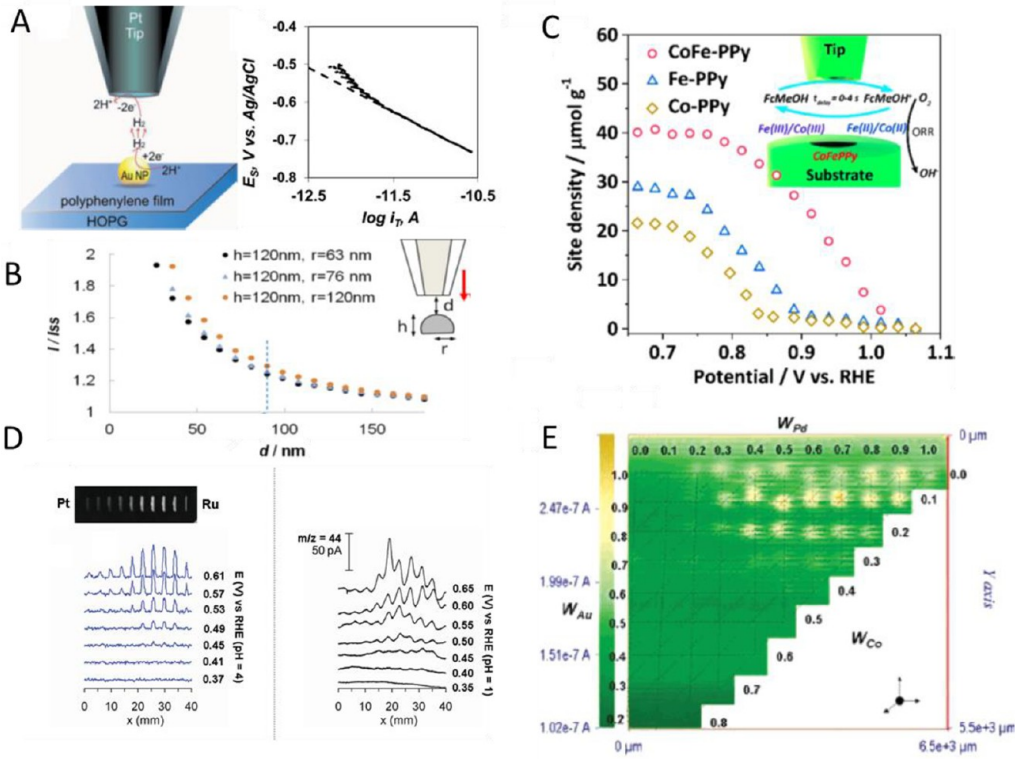

Figure 8. Scanning electrochemical microscopy (SECM). (A) (left) Schematic of a substrate generation tip collection (SG/TC) SECM experiment on a single gold nanoparticle (Au NP) to measure activity and extract kinetic information. The Au NP generates H_2, with the driving force being supplied by biasing the substrate (HOPG). The probe measures the HER activity by collecting (oxidizing) H_2. (right) A Tafel plot for the HER obtained at a single Au NP using this methodology. (B) Current−distance (approach) curves obtained at single platinum nanoparticles of varying sizes with all exhibiting extremely fast electron transfer rates. (C) The use of surface interrogation (SI) mode of SECM to detect the buildup of oxygen intermediates during ORR at novel electrocatalysts. (D) Coupled scanning differential electrochemical mass spectrometry (SDEMS) with SECM used for evaluating a bimetallic catalyst for methanol oxidation. (left, top) Image of Pt−Ru catalyst array. (left, bottom) Catalyst array activity measured at various bias potentials. (right) Corresponding CO_2 generation measured at various bias potentials. (E) Activity mapping of a compositional array of trimetallic Pd−Au−Co ORR electrocatalysts using the tip generation substrate collection (TG/SC) mode of SECM for high throughput screening. (A) is reprinted from with permission from ref 234. Copyright 2014 Wiley. (B−C) are reprinted from with permission from refs 237,241. Copyright 2016, 2019 American Chemistry Society. (D) is reprinted from with permission by the authors from ref 243. Copyright 2013 American Institute of Physics. (E) is reprinted from with permission by the authors from ref 242. Copyright 2005 American Chemistry Society.

environmental control (oxygen, temperature, etc.) if needed. The cell is designed to minimize convection, and sufficient supporting electrolyte is used to mitigate migration. In other words, in a SECM experiment we assume transport in the solution phase is dominated by diffusion. Often a mediator is added to the electrolyte. This is ideally a well-behaved (chemically inert but electrochemically active) species that undergoes a reversible outer sphere redox reaction (ex. ferrocene). The mediator can also be generated *in situ*. This is especially relevant for applications in electrocatalysis where the H^+/H_2 or O_2/OH^- redox couples are suitable mediators for the reaction of interest.

As an electrode, the probe consists of an exposed electronically conducting region surrounded by an insulating sheath. The two important characteristics of a probe for SECM is that the geometry of the exposed conducting (and nearby insulating) region should be well-defined, and the conducting region area should be "small". The criteria for "small" is that we require a steady state current response at the tip when polarized to perform a redox reaction in the bulk electrolyte. This occurs when diffusional distances (in the time frame of an experiment) are on the order of the size of the tip.[232] A 25 μm diameter platinum wire sealed in a glass capillary with the tip sharpened to form an inlaid disk geometry is a common example of a large SECM probe. The smaller the probe, the better the spatial and temporal resolution of the instrument, but the more difficult it is to control the geometry of the tip. A well-defined geometry is needed to get the most accurate quantitative information. Methods for fabricating ultramicroelectrodes (UME) and nanoelectrodes are described elsewhere.[233]

In most SECM experiments, the probe is biased to perform diffusion limited redox chemistry of solution species. Since the tip is small, a spherical concentration gradient develops in the vicinity of the tip where reactants are depleted. This concentration profile extends out 10 tip radii, after which conditions are indistinguishable from the bulk solution. The diffusion limited steady state current measured by the probe in the bulk solution is given by eq 1:

$$i_{ss} = 4nFCDa \quad (1)$$

where n is the number of electrons transferred, F is Faraday's constant, C is the concentration of the redox species in the bulk, D its diffusion coefficient, and a is the radius of the electrode. Dividing eq 1 by the area of the disk, we see that the transport limited current density is inversely proportional to

https://dx.doi.org/10.1021/acscatal.0c04789
ACS Catal. 2021, 11, 1136−1178

the radius of the electrode. Thus, $1/a$ is analogous to the square root of rotation rate in the RDE. In other words, using a tip that is twice as small allows one to measure kinetics that are twice as fast. In an RDE experiment, one would need to rotate the electrode four times as fast to achieve the same effect.

When the tip is closer than roughly 10 radii to the substrate, the probe current is affected by the electrochemical properties of the substrate. In the simplest case of an insulating inert substrate, the topology of the substrate physically blocks the diffusion of the mediator to the probe, resulting in a decrease in the current, otherwise known as negative feedback. Two common experiments are (1) recording the probe current as a function of separation distance or (2) the probe current as a function of lateral position. The first is known as a probe approach curve (PAC). For a flat insulating substrate, this can be used to characterize the geometry of the probe, especially useful for nano sized tips. The second is an imaging experiment used to map the topography of an insulating substrate, taller features blocking more diffusive current. Because of diffusional broadening, SECM cannot match the spatial resolution of other scanning probe microscopies such as AFM, though it has the advantage of being *in situ* and noncontact.

On the other hand, when the probe nears a conducting substrate held at open circuit, the current will generally increase. This surprising phenomenon can be explained as follows. The potential of the substrate is pined by the formal potential and concentration of the bulk mediator. In the vicinity of the probe, the concentration of the mediator is inverted (the opposite redox form dominates). Therefore, for a redox reaction at the probe, there is a slight overpotential for the reverse reaction at the substrate due to concentration differences. The electronic conductivity of the substrate allows nonlocal electron transfer to regenerate the mediator such that the probe sees an effective increase in the flux of reactant, and this corresponds to an increased current. Performing a PAC to a conducting surface or particle allows one to measure the electron transfer rate constant. For complex substrates, careful design of the experiment is necessary to decouple effects of positive and negative feedback.

The mediator can also be used as a reducing or oxidizing agent generated *in situ* by the probe and used to titrate reaction intermediates or facilitate electron transfer reactions at the substrate. After its interaction with the substrate, the mediator diffuses back to the probe to "report" the results. The probe current is related to kinetics of reactions at the substrate, and its integral is related to the quantity of active sites. The response is generally described in terms of dimensionless parameters, which can be used to extract rate constants and surface coverages for model systems. More complex systems require modeling using finite element analysis software. Some of the classic and fundamental SECM experiments have so far been described. However, SECM is most powerful when the user adapts the platform to suite the particular experimental needs. Below we describe several noteworthy examples of these principles being applied in the field of electrocatalysis.

4.2. Applications of SECM in Electrocatalysis. Nanoparticles (NPs) are commonly utilized for electrocatalysis to take advantage of high surface area, short transport distances, and sometimes favorable nanoscale effects. New insights into NP structure−activity relationships are needed to optimize catalyst performance. However, results from studies of bulk NP ensembles can be obscured by their broad size distributions, variations in morphologies, crystallographic orientations, and thus their intrinsic activities. Though significantly challenging, single NP experiments are needed to overcome these obstacles and provide a reliable and controlled environment to study structure−activity relationships. Recent advancements in SECM have opened the door to many such studies.

A modern application of the SG/TC mode of SECM, to study the hydrogen evolution reaction (HER) at a single 10−20 nm sized gold nanoparticle (Au NP) is shown schematically in Figure 8A (left).[234] This experiment, by the Mirkin group, necessitates a substrate that is flat, electrochemically inert, yet at the same time capable of making electrical connection to the Au NP. To achieve this, the authors utilized HOPG passivated with a layer of polyphenylene. The polyphenylene layer blocks redox reactions with the HOPG while still allowing electron transfer between the Au NP and the HOPG. In the terminology of SECM, negative feedback is observed over the insulating polyphenylene layer, while positive feedback is observed near the Au NP. This is an important detail, as it makes it possible to use the FB mode of SECM to image the substrate, find a nanoparticle, and position the probe for the experiment. Once the probe is positioned above the Au NP as in Figure 8A (left), the Au NP can be activated to perform the HER by biasing the substrate. The probe is maintained at a high enough anodic potential to perform a diffusion-limited HOR. In this configuration, the hydrogen produced by the Au NP is collected by the probe. The probe current is a direct measure of Au NP activity. By varying the driving force (bias potential), a Tafel plot for HER at a single Au NP is obtained (Figure 8A, right).

Although studies of hydrogen evolution at single NPs have been performed previously, notably, the pioneering work of Stimming,[235] the above-described work has achieved several advancements. First, the feedback mode of SECM made it possible to image the substrate and select a NP to study. In the Stimming experiment, the NP was both deposited and analyzed by the STM probe. The ability to decouple NP synthesis and analysis greatly expands control over the variables that affect NP activity. Second, in part due to the controlled probe geometry, SECM offers more quantitative information. In a follow up paper, the authors applied SECM theory and modeled the effects of various NP geometries to extract a collection efficiency correction for measured activity and to estimate NP size more accurately using the approach curve experiment.[236]

One of the primary variables of interest for elucidating structure−activity relationships is particle size. The approach curve experiment has been performed at variously sized single Pt NPs, shown in Figure 8B.[237] The probe, positioned above the NP, is approached closer while recording the probe current. Decreasing the tip to particle separation distance, d, allows faster kinetics to be interrogated since diffusion distances are reduced. Using this approach, Bard et al. measured a very high effective rate constant of HOR, $k_{\mathrm{eff}}^{0} >$ 2 cm/s. Importantly, the study also reports a minimal variation in HOR activity for the NP size range examined. Indeed, there are conflicting conclusions in the literature as to the effect of NP size on electrocatalytic activity. The authors point out that results can be affected by polydispersity in ensemble studies, artificial effects from techniques which are not *in situ*, or contaminants in poorly controlled single NP experiments. Advanced nanoscale SECM has made it possible to remedy many of these challenges and provide reliable data for elucidating structure activity relationships in electrocatalysis.

https://dx.doi.org/10.1021/acscatal.0c04789
ACS Catal. 2021, 11, 1136−1178

Specifically, SECM has been used to measure the geometric properties and catalytic activity of single NPs, even when deposited as an ensemble on a substrate.[234,237] Further, transport limitations are mitigated so that electron transfer kinetics are specifically measured *in situ* and with good control of environmental effects.

To gain a worthwhile fundamental understanding, kinetic studies must be taken further. Heterogeneous catalysis is often a multistep process that proceeds via adsorbed intermediates. Although adsorbates and surface structure are critical to electrocatalysis, there are very few *in situ* and surface selective techniques available to unveil such details. Spectroscopic methods, in general, provide a bulk measurement. Effects from catalyst crystal structure or electrolyte processes obscure surface information. In-depth data processing and interpretation are necessary to tease out surface information from the total signal. When compared to challenging *in situ*/*operando* TEM and X-ray methods, SECM, coupled with traditional electrochemical methods, serves as an ideal platform to investigate electrocatalysts under operating conditions. A major constraint, however, is the electrode serving as both the substrate and the measurement tool. For a controlled study, it is necessary to decouple electrode operation from the measurement on the electrode. By utilizing a second electrode, the probe, SECM retains the benefits of classic electrochemical methods and introduces additional and powerful capabilities. Specifically, the surface interrogation mode of SECM (SI-SECM) is highly surface selective and capable of quantifying both coverages and reactivity of adsorbates on catalytic surfaces. It has been utilized to elucidate incipient oxides on Au that are undetected by CV,[7] used to show that hydrogen coverage follows a Frumkin isotherm with respect to the applied potential on a Ni HER catalyst,[238] and applied to extended surfaces to identify multiple unique adsorbates during water oxidation on hematite.[239,240]

SI-SEM is best utilized as a tool in broader catalyst studies. A recent example is highlighted in Figure 8C.[241] The inset shows a schematic of the SI-SECM experiment. The catalyst ink was deposited on a small carbon substrate electrode to eliminate the nonlocal electron transfer, and the probe was positioned above and close to the catalyst. The substrate electrode was activated for the ORR in alkaline media at various potentials (x axis of Figure 8C), generating adsorbed intermediates. To measure their coverage, adsorbates were titrated with an oxidizing agent generated by the probe *in situ*. Ferrocene is oxidized by the probe, which, in turn, oxidizes the adsorbates. A positive feedback loop forms as adsorbates are depleted. Integrating the tip current (after subtracting the negative feedback background and accounting for collection efficiency) yields the active site density (y axis of Figure 8C).

This experiment was carried out for novel ORR catalyst structure/composition and used to investigate the synergistic effects of bimetallic catalysts. Specifically, it was found that Fe−Co bimetallic catalysts could achieve a significantly improved ORR performance, relative to either monometallic form and comparable performance to commercial Pt/C. SI-SECM results (Figure 8C) provide several important pieces of kinetic and mechanistic information to this end. First, it can be seen that adsorbates appear ∼100 mV before any appreciable ORR current is observed at the substrate in both CV and RDE experiments. An increase in the driving force corresponds to both an increase in activity and an increase in surface coverage of active sites. However, at a sufficiently high driving force, the coverage reaches a saturation value. Notably, the bimetallic catalyst exhibits both a lower onset potential for adsorbates and a higher saturation coverage. Introducing a time delay between the activation and titration steps provides information about the binding rate between Fe(II)/Co(II) and O_2 by plotting the logarithmic active site number against the delay time. A good linear fit confirms first-order reaction kinetics as expected for this process. It was found that the bimetallic catalyst exhibited a much faster binding rate to oxygen in contrast to monometallic catalysts. In conjunction with XPS, SEM, and other electrochemical data, the SI-SECM results were used to infer important mechanistic insights. Specifically, it suggested that the Fe(II) is the primary ORR active site with Co(II) serving as an inducer to modulate the electronic structure of iron.

Most strategies for moving away from Pt-based catalysts include delegating the various catalytic tasks to multiple metal centers. In the absence of complete structure−activity understanding, large catalyst libraries must be developed and screened for optimizing the ORR performance. This is generally a time-consuming, labor intensive process to prepare nanoparticles and evaluate their activity. One of the classic applications of SECM in electrocatalysis is for high-throughput screening of multicomponent catalyst arrays.[242] In this configuration, the probe is positioned close to a substrate onto which an ORR catalyst array is patterned. The probe electrode is biased to electrogenerate oxygen which diffuses locally to the substrate. Since the electrolyte is purged of oxygen, only the catalyst sample immediately below the probe will contribute to the substrate current. An activity map of Pd−Co bimetallic alloys, such as that shown in Figure 8E, is obtained in a matter of minutes by scanning the probe while maintaining a cathodic bias at the substrate. The optimal catalyst composition is easily seen as the sample containing 10−30% Co, which "lights up" the brightest in the ORR activity map measured in acidic media.

It is important to note that a promising catalyst, as measured by an activity map or even RDE experiment does, not always correspond to good performance or durability in a practical device, such as a fuel cell. Though there are many reaction and device specific reasons, an important general consideration is that high activity does not imply high selectivity. This is particularly important in complex or multi reactant catalysis such as methanol oxidation or CO_2 reduction. To this end, our group has coupled scanning differential electrochemical mass spectrometry (SDEMS) with SECM.[243] While SECM measures catalyst electrochemical activity, SDEMS is used to identify and measure gaseous reaction products and by-products. In a single high throughput scan, both catalyst activity and selectivity can be measured. This is exemplified for a binary Pt−Ru catalyst array for the methanol oxidation reaction pictured in Figure 8D (top left). The array was produced by simultaneously sputtering Pt and Ru onto a Ti-coated Si wafer. The composition ranged from 80:20 Pt/Ru at x = 0 to 20:80 Pt/Ru at x = 40 mm. The activity line scan is shown (left), while SDEMS monitored CO_2 evolution at m/z = 44 (right). The peak intensities correlate very well to the position of the catalyst and between both measurements, validating the methodology. Importantly, it can be seen that the maximum activity occurs at a higher Ru composition compared to the maximum of CO_2 production. This experiment highlights that activity alone does not tell the complete story; measurement of reaction products is also an

https://dx.doi.org/10.1021/acscatal.0c04789
ACS Catal. 2021, 11, 1136−1178

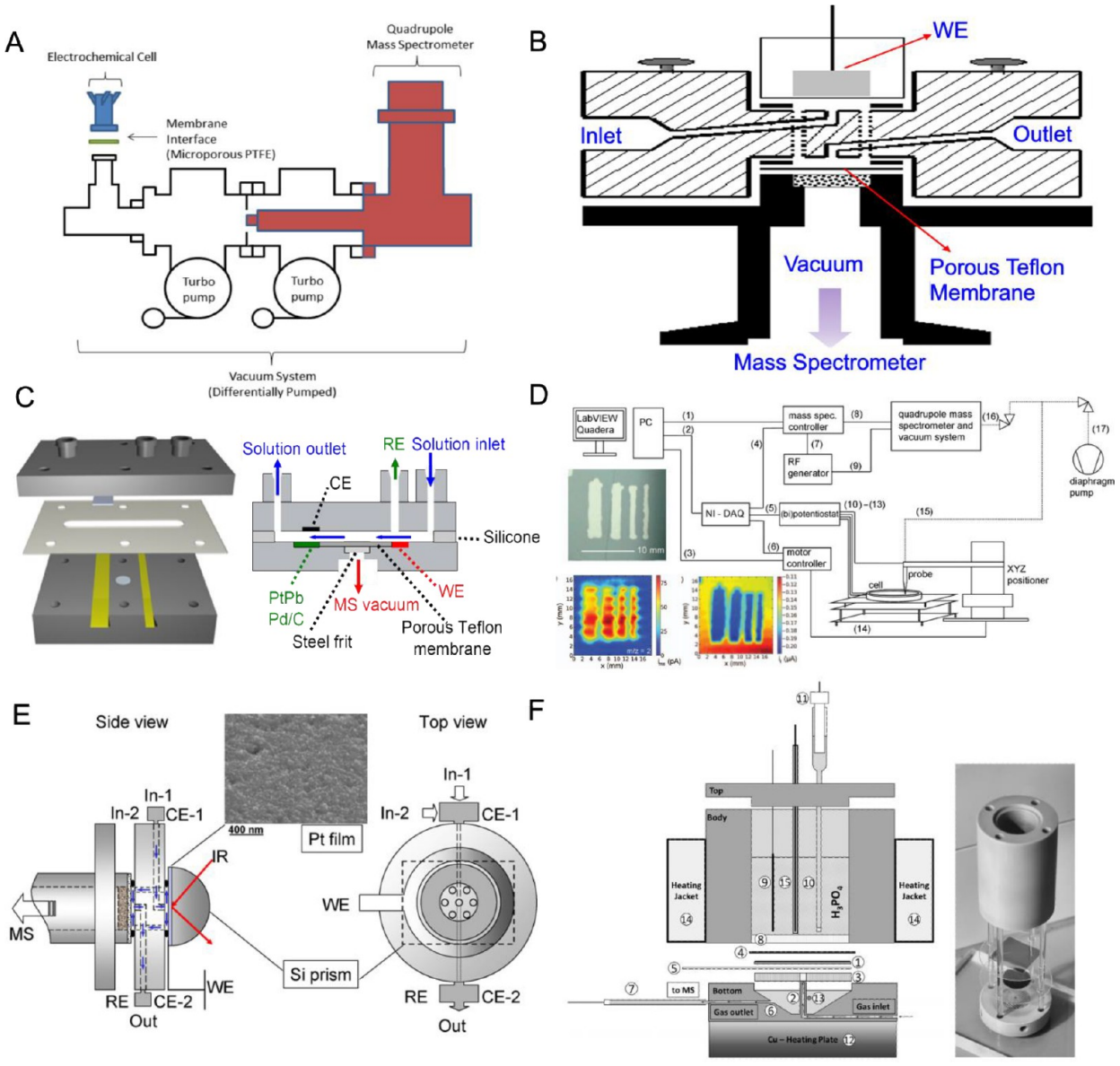

Figure 9. Differential electrochemical mass spectrometry (DEMS) configuration and cell designs. (A) Schematic of a DEMS setup. (B) Cross-sectional view of a dual-thin layer flow DEMS cell; WE represents the thin-film working electrode while counter and reference electrodes are not shown. (C) An outlook (left) and schematic (right) of a double-band-electrode channel flow DEMS cell. (D) A block diagram of SDEMS-SECM system; The bottom left part shows a photograph of Pt strips on a Ti/Si substrate and their corresponding DEMS (m/z = 2) and SECM mapping results. (E) Side and top view of DEMS setup coupled with ATR-FTIR spectroscopy; The In-1 and In-2 represent two inlets for electrolyte while CE-1 and CE-2 are connected to two counter electrodes; The RE and Out stand for reference electrode and electrolyte outlet. (F) Schematic diagram (left) and photo (right) of a high-temperature DEMS cell: (1) working electrode, (2) gas inlet nozzle, (3) supporting sieve, (4) membrane, (5) electric contact, (8) glass filter, (9) counter electrode, (10) Luggin capillary (11) reference electrode (13) and (15) thermocouples. (A) is reprinted with permission from ref 257. Copyright 2012 Springer. (B, C) are reprinted with permission from refs 258, 263, respectively. Copyright by the authors 2020, 2010 American Chemistry Society. (D) is reprinted with permission from ref 243, respectively, Copyright 2013, American Institute of Physics. (E, F) are reprinted with permission from refs 259,268. Copyright 2007, 2015 Elsevier.

important metric for assessing catalyst selectivity. Coupled SECM and SDEMS is thus a powerful tool for both catalyst screening and fundamental studies.

In summary, SECM is an advanced *in situ* electroanalytical technique with high spatial resolution, making it well suited for applications in electrocatalysis. It is worth mentioning that related electrochemical probe/pipet techniques exist, with new ones emerging.[244,245] Of these, scanning electrochemical cell microscopy (SECCM) has recently enabled several novel and exciting electrocatalysis studies.[246−248] Introduced by the Unwin group in 2010,[249] SECCM is showing significant promise as it begins to mature. Compared to spectroscopy and microscopy, SECM, SECCM, and related techniques are still in their infancy. As they become more widely accessible to general research groups, electrochemical probe techniques will likely make a large impact in electrocatalysis research.

5. DIFFERENTIAL ELECTROCHEMICAL MASS SPECTROSCOPY (DEMS)

Bruckenstein and Gadde reported the first application of mass spectrometry in an electrochemical system in the 1970s by collecting electrochemically generated oxygen via a hydro-

https://dx.doi.org/10.1021/acscatal.0c04789
ACS Catal. 2021, 11, 1136−1178

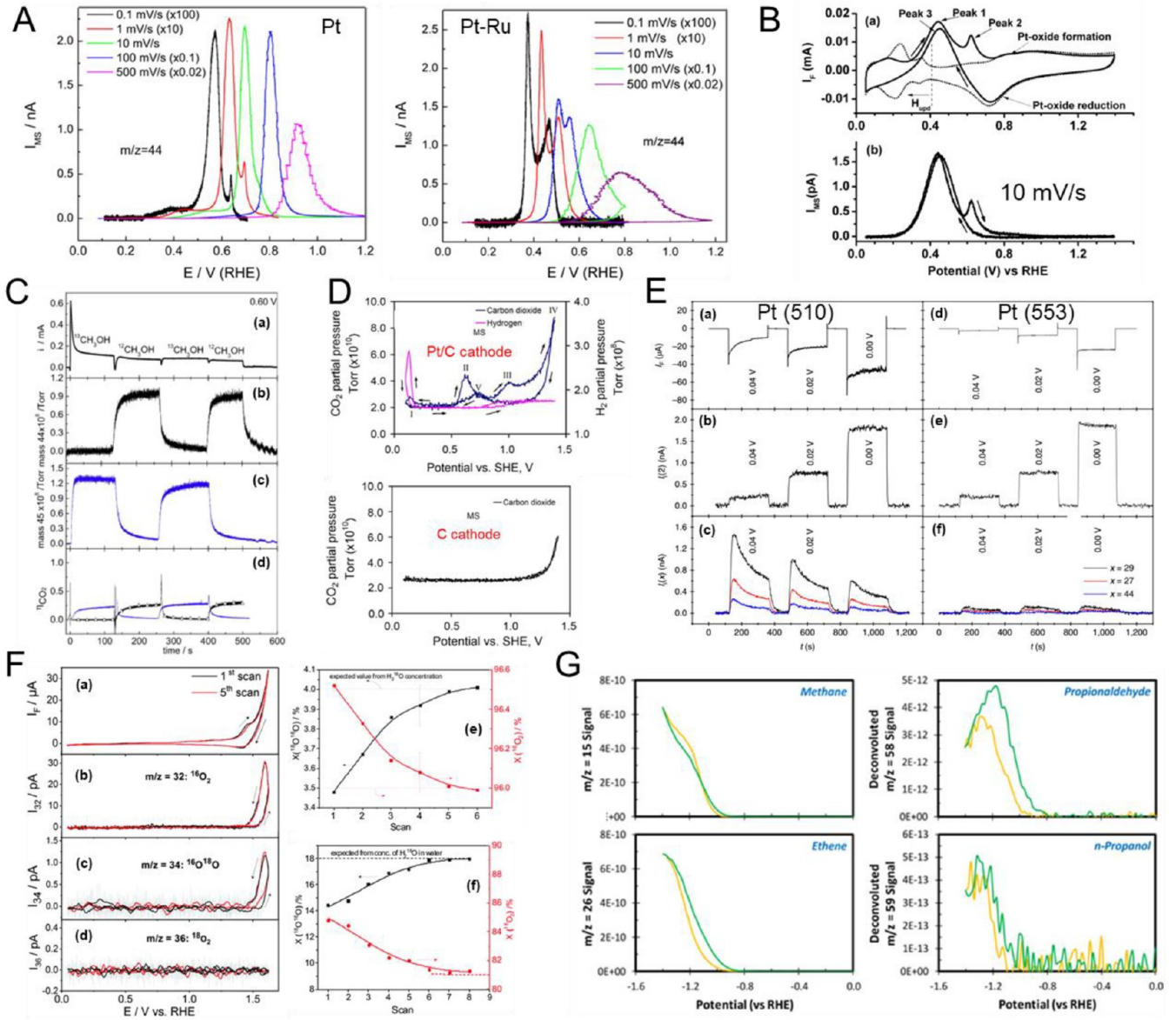

Figure 10. Applications of DEMS in electrocatalytic reactions. (A) Scan rate dependent mass spectrometric cyclic voltammograms (m/z = 44) for the oxidation of preadsorbed CO on Pt and on a Ru-modified Pt polycrystalline electrode (θ = 0.25) in 0.1 M H_2SO_4. (B) Cyclic voltammograms and corresponding CO_2 mass signals (m/z = 44) for formate oxidation on a Pt electrode sputtered on a porous Teflon membrane, in 0.1 M HCOONa and 1 M NaOH at a scan rate 10 mV/s. (C) Time response of methanol oxidation on a Pt film electrode at 0.6 V in 0.1 M $^{12}CH_3OH/^{13}CH_3OH$ and 0.5 M H_2SO_4. (D) DEMS spectra for CO_2 formation with Pt/C and carbon as cathode, respectively. (E) Potential-step induced faradaic current and mass signals (m/z = 2, 29, 27, and 44) on Pt (510) and Pt(553) in 0.1 M acetone and 0.1 M H_2SO_4 solution. (F) DEMS results of oxygen evolution at Co_3O_4 particles (40 μm) in 0.5 M KOH solution containing 2 wt % $H_2{}^{18}O$ (a–d); calculated $^{18}O^{16}O$ content as a function of scan numbers obtained from Co_3O_4 particles (40 μm) (e) Co_3O_4 particles (50 nm) (f). (G) DEMS results of partial CO_2 reduction products, including methane, ethylene, propionaldehyde, and n-propanol in CO_2-saturated 0.1 M $CsHCO_3$ solution with scan rate of 1 mV/s; CO_2, H_2, CO, acetaldehyde, ethanol and allyl alcohol are not shown here. (A, B) are reprinted with permission from refs 254, 280, respectively. Copyright by the authors 2015, 2012 American Chemistry Society. (C) is reprinted with permission from ref 265. Copyright 2017 Elsevier. (D) is reprinted with permission from ref 306. Copyright 2009 Elsevier. (E) is reprinted with permission from ref 315, respectively, Copyright 2019, Springer Nature. (F) is reprinted with permission from ref 318, Copyright 2017 Royal Society of Chemistry. (G) is reprinted with permission from ref 323, Copyright 2018 American Chemistry Society.

phobic porous Teflon electrode and then analyzing it with a mass spectrometer.[250] Later, Wolter and Heitbaum used a similar inlet system but improved the vacuum system with two differentially pumped stages, which significantly reduced time constant to less than 1 s.[251] This improvement enabled online detection of gas evolution rates during cyclic voltammograms. The term "differential" was introduced to stress the difference from the former integrating approach developed by Bruckenstein and Gadde.

5.1. DEMS Configuration and Cell Designs. A typical DEMS instrument is composed of an electrochemical cell, vacuum system (two differential pumps), and quadrupole mass spectrometer (Figure 9A).[257] A microporous Teflon membrane is commonly employed to interface the electrochemical cell with the vacuum system to allow transport of the gas

https://dx.doi.org/10.1021/acscatal.0c04789
ACS Catal. 2021, 11, 1136–1178

molecules or volatile products into the vacuum chamber while preventing electrolyte leakage. As the key component in DEMS setup, the electrochemical cell has been tailored with four general configurations for different working conditions, namely, conventional cell, thin-layer cell, dual thin-layer flow cell, and capillary inlet.[252−257] The conventional cell exhibits a fast response but requires a porous working electrode deposited onto the porous PTFE membrane. To mitigate this limitation, a thin-layer cell was developed that enabled the use of bulk electrodes. A derivative of the thin-layer cell, the dual thin-layer flow cell (Figure 9B),[258] consists of two separate chambers and can be coupled to other analytical tools, such as infrared spectroscopy[259] and the electrochemical quartz crystal microbalance (EQCM).[260] A capillary inlet configuration is typically used for scanning DEMS (SDEMS),[261] in which a probe (PTFE tubing covered by Teflon film) connected to the vacuum system is scanned to sample the region above the surface of the bulk working electrode. While this design enables measurements of local activity and combinatorial screening, it suffers from slow response and challenges in quantification.[262]

In addition to the above-mentioned prototypes, the research community has witnessed impressive developments of DEMS. We recently developed a double-band-electrode channel flow DEMS cell,[263] comprising a working and detecting electrode separated by a porous PTFE membrane (Figure 9C), with a configuration similar to a rotating ring-disk electrode (RRDE). As volatile species can be monitored by mass spectrometry, this DEMS cell provides additional opportunity to selectively probe nonvolatile products with the detecting (downstream) electrode. We also developed an exchangeable-tip scanning probe that coupled both scanning DEMS and scanning electrochemical microscopy (SDEMS-SECM) (Figure 9D).[243,264] While the SDEMS part could spatially resolve the generation of volatile species on the surface of a substrate electrode, the SECM portion could function as a detector to examine the overall electrochemical activity of the surface and ensure the leveling of the sample (critical for quantification). This technique proved effective for combinatorial screening of efficient electrocatalysts for direct alcohol fuel cells (Figure 9D inset and Figure 8D). Behm et al.[259] designed a novel setup based on attenuated total reflection-infrared spectroscopy (ATR-FTIRS) and dual thin-layer flow cell (Figure 9E), which allowed online examination of both adsorbed intermediate species and volatile reaction products. The application of this technique for mechanistic studies has been demonstrated in the oxidation of CO and methanol.[259,265]

Although the aforementioned designs have improved understanding of reaction kinetics and mechanisms, they posed additional challenges for *operando* characterization of fuel cells under operating conditions. Pastor et al. demonstrated the use of a new DEMS cell configuration to study the alcohol oxidation reaction with a gas diffusion electrode usually used in fuel cells.[266] While the use of a gas diffusion electrode represents an improvement over typically used thin film electrodes, the experimental conditions are still far removed from real operating devices under elevated temperatures with humidified gas reactants. Behm et al.[267] built a thin-layer channel flow cell with a poly-ether-ether-ketone (PEEK) polymer, enabling studies at high temperatures and pressures of up to 120 °C and 3 bar, respectively. Nevertheless, this device could only work with liquid electrolytes. In an attempt to develop a DEMS setup that could work under conditions close to the high temperature polymer electrolyte fuel cells, Niether et al.[268] proposed a new experimental DEMS cell which enabled the study of gas-phase reactions at temperatures between 120 and 180 °C (Figure 9F).

5.2. Applications of DEMS in Electrocatalytic Reactions. Starting from its introduction, DEMS has been widely employed in the electrochemical community, especially for electrocatalytic reactions. As mentioned above, DEMS can provide unique chemical identification of volatile reaction products not only for qualitative analysis but also semi-quantitative or even quantitative measurements. Quantitative DEMS analysis offers deeper insights into reaction selectivity and reaction mechanisms.[269] However, the key to such studies hinges on the choice of an appropriate calibration protocol, which can bridge the ionic mass signals and corresponding faradaic current. Here, we provide a brief overview of the applications of DEMS in electrocatalysis. Interested readers are referred to other reports for a detailed description of the techniques.[256,270]

Fuel cells represent one of the most promising energy conversion devices for their high energy conversion efficiency and pollution-free emission.[271] Liquid fuels based on formic acid and alcohols (methanol and ethanol) have been intensively investigated since they are inexpensive and easy to handle and transport.[272] Since oxidation of these small organic molecules (SOMs) involves formation of volatile products, e.g., CO_2, DEMS provides a unique perspective to investigate the reaction kinetics and mechanisms.

Since the oxidation of carbon-containing liquid fuels involves the unavoidable formation of adsorbed CO species (CO_{ads}),[273] it is essential to elucidate the reaction kinetics and mechanisms of CO oxidation for designing effective CO-tolerant electrocatalysts.[274] Recently, we observed the presence of multiple peaks when investigating the potentiodynamic oxidation of preadsorbed CO on the surface of Pt and Pt−Ru electrodes with DEMS (Figure 10A).[254] The peak splitting became more evident when the sweep rate was decreased to 0.1 mV/s. This observation could only be captured by DEMS since the faradaic current signals for CO oxidation are complicated by the pseudocapacitive responses, and the resulting faradic currents at such a low sweep rate are essentially unmeasurable. Assisted with simulations, the peak multiplicity was proposed to originate from competitive adsorption of CO and OH species, leading to suppressed CO repopulation from less active sites to more active sites on different facets or regions.[254]

DEMS has also played a key role for studying the mechanism of the formic acid oxidation reaction (FAOR). In an ^{18}O labeling experiment by Wolter et al.,[275] DEMS provided direct evidence for the dual pathway mechanism of the FAOR, in which direct oxidation, without loss of oxygen, and indirect oxidation, via a strongly adsorbed intermediate, occur in parallel. Additionally, the reaction kinetics of the FAOR have been extensively investigated on Pt single-crystal electrodes under different reaction conditions[276] and with different secondary adsorbed metal modifications.[277−279] Despite intensive studies in acidic media, the formate oxidation reaction in alkaline media remained largely unexplored. We reported on a mechanistic study of the oxidation of formate on Pt in 1 M NaOH.[280] As shown in Figure 10B, the use of DEMS enabled deconvolution of formate oxidation signals (CO_2 formation) from the cyclic voltametric features of Pt (H-

https://dx.doi.org/10.1021/acscatal.0c04789
ACS Catal. 2021, 11, 1136−1178

region, double layer region, and Pt oxide formation/reduction) as the $HCOO^-$ oxidation is rather sluggish.

The oxidation of methanol is more kinetically challenging as the reaction involves six electrons, resulting in multiple intermediates and reaction products.[272] The broad distribution of intermediates and products also provides an opportunity for *operando* DEMS studies. DEMS has been used to elucidate the nature of adsorbates[281] and identify the reaction pathways of methanol oxidation.[282,283] As presented in Figure 10C, the combination of DEMS with electrochemical ATR-FTIR provided rich kinetic information as it enabled online quantification of the total amount of CO_2 generated from the methanol oxidation as well as the amount of CO_2 produced via CO_{ads} from the indirect pathway.[265] Those results indicated that a significant amount of CO_2 was produced via non-CO_{ads} pathway and that the contribution of CO_{ads} to CO_2 decreased as the potential increased from 0.60 to 0.75 V. DEMS has been used to investigate multiple factors that could influence the methanol oxidation reaction (MOR), including cocatalytic effects of Pt-electrodes modified by other elements,[284] the effects of composition,[285] particle size,[286] temperature,[269] anion adsorption,[287] mass transport,[288−290] and the influence of reactive side products.[291]

The scission of the C−C bond in ethanol is kinetically extremely challenging, resulting in significantly low current efficiency and wide distribution of products.[256,292] Hence, DEMS plays a key role in detecting and analyzing the incomplete products of ethanol oxidation, providing valuable information for mechanistic studies and catalyst optimization. Early DEMS studies have focused on the oxidation of adsorbed ethanol.[293−295] Similar to the oxidation of methanol, DEMS has been widely applied to study the impact of multiple factors on reaction mechanisms, kinetics and selectivity, e.g., surface structure,[296] doping modifications,[297] H- and OH-adsorbates on the electrode,[298] pH,[299] mass transport,[300] and others. Compared to acidic media, C−C bond scission was reported to be less demanding in alkaline media.[301] The electro-oxidation of ethanol at different catalyst metals (Pt, Pd, Au, and Ni) has been systematically investigated with DEMS in alkaline media.[302]

In addition to the challenging kinetics of oxidation of liquid fuels, the corrosion of the carbon support is another important issue affecting the long-term durability of fuel cells.[303,304] Since CO_2 is a major product during the corrosion of carbon, DEMS presents clear advantages for monitoring carbon corrosion in hydrogen fuel cells.[305] Lane et al.[306] reported that the presence of Pt catalysts could catalyze the corrosion of carbon supports at potentials as low as 0.5 V, as revealed by DEMS results (Figure 10D). This observation pointed toward the critical importance of choosing the proper support/substrate to enhance catalyst durability. Behm et al.[307] employed DEMS to examine the formation of CO_2 during CV scans on two different carbons under different treatments, and found that the graphitized carbon with low porosity and oxygen content, was most resistive toward corrosion. Other DEMS studies have also provided insights into mechanisms of carbon corrosion and guidance on designing more durable supports.[308−310]

Besides fuel cells, DEMS has also been used for the elucidation of other electrocatalytic reaction mechanisms, including oxidation/reduction of other small molecules.[311−315] Recently, Koper et al.[315] studied the surface structure-sensitivity of acetone reduction on different Pt single crystal electrodes. The DEMS results for acetone reduction on Pt(110) steps (Figure 10E) revealed that it could be reduced to propane on a Pt(510) $[(n + 1)(111) \times (110), n = 5]$, as evidenced by the strong fragment signals at m/z = 29, 27, and 44. In contrast, only negligible propane signals were observed on a Pt(553) $[(n - 1)(111) \times (110), n = 5]$ stepped surface, indicating that the main product on Pt(553) should be 2-propanol, which was further supported by *in situ* FTIR measurements. Such a reaction selectivity was ascribed to the medium and low generalized coordination numbers on Pt(510) and Pt(553), respectively.

Water oxidation in alkaline media represents an important reaction for solar fuel-based energy conversion, but the reaction mechanisms still remain debatable.[316,317] On the basis of DEMS results with ^{18}O isotope labeling (Figure 10F), Baltruschat et al.[318] proposed that the oxide layer of Co_3O_4 nanoparticles participates in the oxygen evolution reaction (OER) via a lattice oxygen exchange process and only about 10−30% of the surface atoms participate in the OER active sites. As reported by Strasser et al.,[319] DEMS enabled the *operando* quantitative deconvolution of charges injected into Ni−Fe hydroxide electrocatalysts for the OER. Nocera et al.[320] observed the emergence of a significant amount of CO_2 with O_2 evolution during water oxidation, suggesting that the glassy carbon electrode is likely corroded under water oxidation conditions.

CO_2 reduction is another interesting, though challenging, topic given the broad range of reaction products, especially when using copper electrocatalysts.[321] However, product quantification has relied heavily on gas chromatography (GC) for gaseous products, and high-performance liquid chromatography (HPLC) or nuclear magnetic resonance (NMR) for liquid products, making it essentially impossible to capture transient reaction kinetics. Recently, Mayrhofer et al.[322] reported a real-time observation of the gaseous products of CO_2 reduction with a thin-layer flow cell DEMS cell, which was used for rapid screening of bimetallic electrocatalysts. Nevertheless, species detection was limited to only gas products and the ill-defined collection efficiency made quantification difficult. Bell et al.[270,323] developed a DEMS cell that allows real-time monitoring and rapid quantification of reactants and products generated in the vicinity of the cathode to probe the local reaction kinetics and mechanisms, including CO_2, H_2, CO, methane, ethylene, acetaldehyde, ethanol, allyl alcohol, propionaldehyde, and *n*-propanol (Figure 10G).

In summary, DEMS is playing a growingly important role in *operando* characterization of electrocatalytic reactions, representing a powerful technique for online and real-time identification and quantification of reaction species. With the development of novel DEMS cell designs and coupling to other advanced analytical tools, DEMS is enabling additional insights for elucidating reaction mechanisms and kinetic information, essential for electrocatalyst design and optimization. However, as a technique, DEMS has some limitations/challenges that need to be carefully taken into account when designing the experiment and analyzing the data. (i) The use of a flow cell configuration can introduce mass transport effects on the quantification of reaction kinetics of methanol and ethanol oxidation[289] as well as their columbic efficiencies.[288] An appropriate flow rate needs to be selected in order to not only minimize signal tailing, but also maximize signal-to-noise ratio. Additionally, since reaction intermediates, which can go through desorption/readsorption processes, are less likely to be readsorbed under fast mass transport conditions,[288] great

https://dx.doi.org/10.1021/acscatal.0c04789
ACS Catal. 2021, 11, 1136−1178

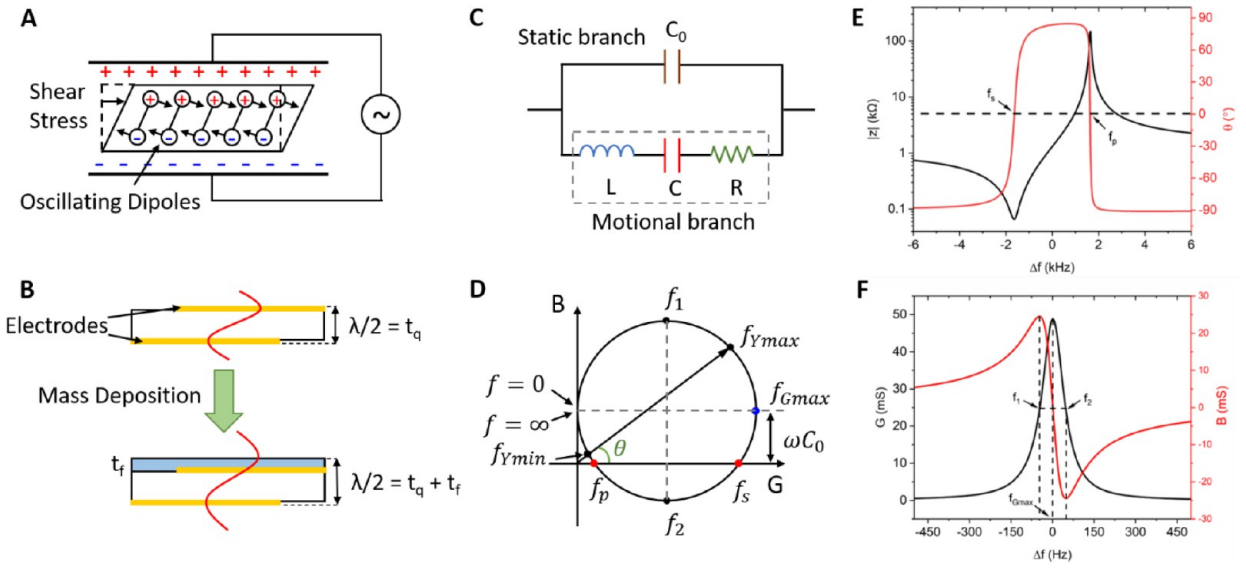

Figure 11. Principles of electrochemical quartz microbalance (EQCM). (A) Schematic of the converse piezoelectric effect for an AT-cut quartz crystal; (B) illustration of the mass change detection at the quartz crystal by shifting the resonant frequency; (C) Butterworth-Van-Dyke (BVD) model of the QCM; (D) admittance locus for a QCM resonator based on the BVD model; (E) a typical Z−θ plot and (F) a typical B−G plot in the resonance region of a bare quartz crystal electrode in air. All color figures in (A−D) were replotted by the authors and adapted from black figures from ref 327 with permission. Copyright 1992 American Chemistry Society. (E−F) are from data by the authors.

attention needs to be paid when comparing DEMS results with other coupled techniques involving stationary electrolytes, i.e., gas chromatography and infrared spectroscopy. (ii) Since the electrolyte composition exerts a significant influence on the ionization probability of a given species, the concentration effects of organic fuels on the calibration constants need to be taken into account when using DEMS for quantitative analysis.[290] Meanwhile, changes in the electrolyte composition can alter background signals and affect the determination of calibration constants. A constant solution composition should be maintained during DEMS measurements and calibration processes. (iii) For electrocatalytic reactions involving gaseous reactants on bulk electrodes, DEMS capabilities could be compromised by the formation and accumulation of bubbles arising from the gas-saturated solution.[270] (iv) DEMS studies of the oxidation of organic fuels in base are often restricted by the formation of carbonate in alkaline media. Although a recent study reported the monitoring of CO_2 generated in base by electrolyte acidification,[308] it remains a great challenge to perform real-time tracking of CO_2 formation on bulk electrodes in alkaline media. In summary, further improvements and optimizations in device design need to be made to tackle the above-mentioned challenges and limitations facing DEMS, in order to enable *operando* measurements of electrocatalytic reactions.

6. ELECTROCHEMICAL QUARTZ CRYSTAL MICROBALANCE (EQCM)

The high sensitivity of the electrochemical quartz crystal microbalance (EQCM) enables the real-time measurement of mass changes during dynamic electrochemical processes at the electrode surfaces. Both faradaic and nonfaradaic process can be detected via this *in situ* technique. The capability of sensing ingress and egress of neutral species at the electrode interface, in addition to the electron transfer processes, greatly benefits mechanistic studies. Besides the gravimetric response, EQCM can also be influenced by the liquid environment that the electrode is in contact with. Insights of potential-dependent catalysts and solvent dynamics have been provided by fundamental studies conducted with the EQCM. Here, we focus on the utilization of the EQCM in studies of electrocatalytic processes with a brief introduction of the EQCM fundamentals. In particular, we will review the use of EQCM for monitoring catalyst deposition and displacement at the electrode surface, characterizing catalyst degradation processes, and studying the mechanisms for electrocatalysis that could not be examined solely by electrochemical responses. The discussion of the application of EQCM to other fields, such as mechanical and hydrodynamic characterization of energy storage electrodes, can be found in other review papers.[324,325]

6.1. Fundamental Principles of EQCM. The fundamental principle of the EQCM relies on the converse piezoelectric effect as depicted in Figure 11A. An alternating electric field leads to the reorientation of the dipoles, thus inducing the oscillation of the quartz crystal in shear mode. A standing wave can be established when the wavelength is equal to twice the thickness of the crystal. When a rigid film is deposited on the quartz crystal surface, it will oscillate with the crystal as an add-on thickness, illustrated in Figure 11B. As a result, the resonant frequency will decrease because of the increase in thickness. The mass change of the quartz crystal can be related to the frequency shift by the Sauerbrey equation:

$$\Delta f = -\frac{2f_0^2}{A\sqrt{\rho_Q \mu_Q}}\Delta m \tag{2}$$

where f_0 is the fundamental resonant frequency of the quartz crystal, A is the piezoelectrically active area, ρ_Q is the density of quartz and μ_Q is the shear modulus. The sensitivity constant is defined as $C_f = \frac{2f_0^2}{A\sqrt{\rho_Q \mu_Q}}$. The sensitivity of the quartz crystal electrode depends on the piezoelectrically active area and the initial resonant frequency governed by the thickness of the

https://dx.doi.org/10.1021/acscatal.0c04789
ACS Catal. 2021, 11, 1136−1178

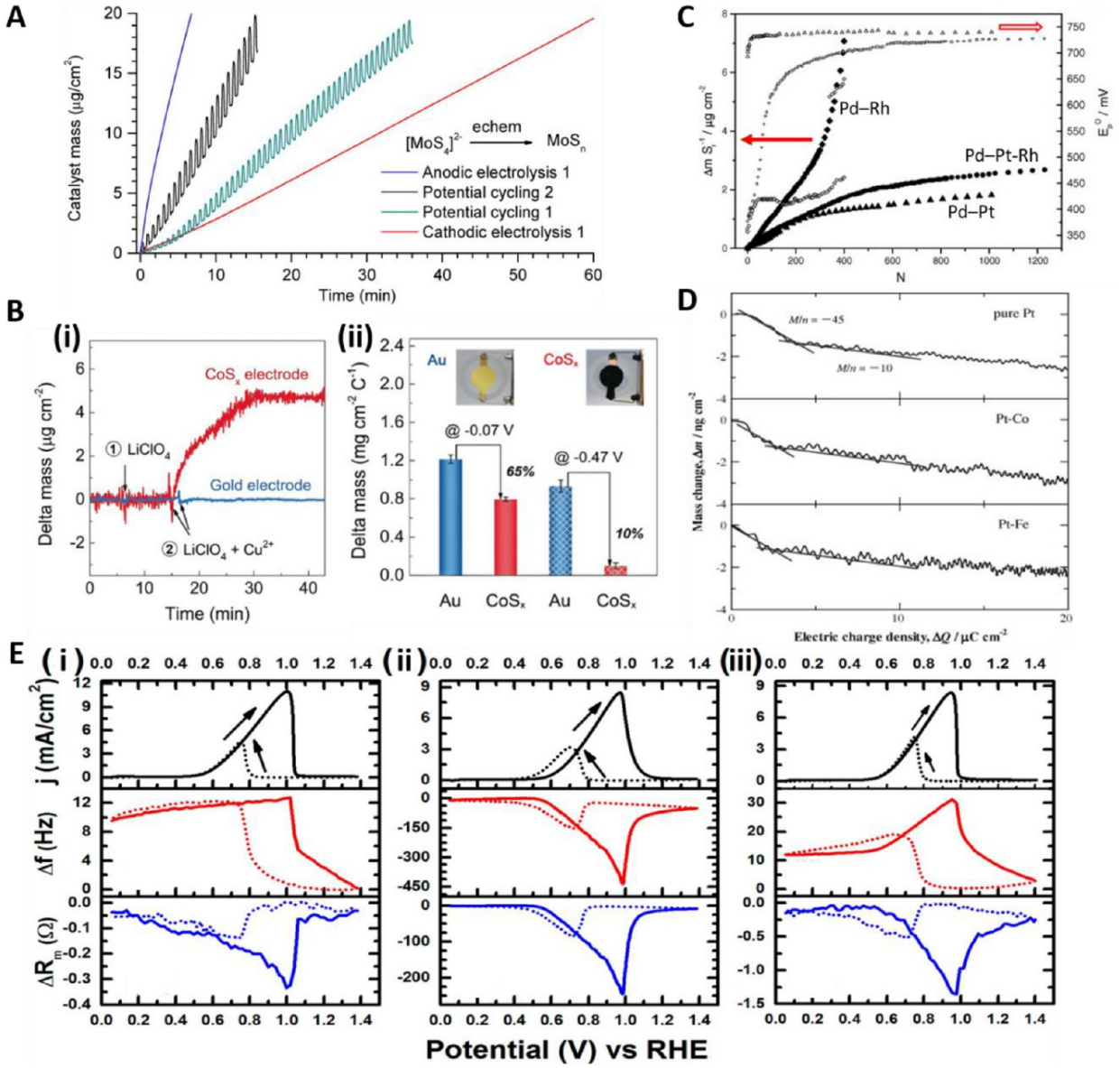

Figure 12. Applications of EQCM in electrocatalysis. (A) Comparison of the growth rate of molybdenum sulfide films using different deposition methods: anodic electrolysis at 0.7 V (blue) with 2 mM $[MoS_4]^{2-}$, potential cycling from 0.7 to −0.4 V with 3.9 mM $[MoS_4]^{2-}$ (black), potential cycling from 0.7 to −0.4 V with 2 mM $[MoS_4]^{2-}$ (green), cathodic electrolysis at −0.4 V with 2 mM $[MoS_4]^{2-}$ (red). Au substrate, $NaClO_4$ electrolyte (0.1 M), scan rate 50 mV/s for the deposition by potential cycling. (B) (i) Mass change of CoS_x-film coated and bare Au electrodes at open circuit after adding 0.5 mL of $LiClO_4$ (0.1 M) DMF solution with and without 3 mM Cu^{2+} ions; (ii) EQCM-determined average mass changes per coulomb passed on Au and CoS_x-film electrodes for 10 repetitions of chronoamperometry (CA) tests at −0.07 V and −0.47 V (vs NHE), respectively. Insets show the photos of Au and CoS_x-film electrodes. (C) Loss of electrode mass per unit of real surface area (solid symbols) and the changes in the potential of surface oxide reduction peak (open symbols) as a function of number of potential cycles over the range of −0.03−1.37 V (scan rate 0.1 V s^{-1}) for Pd alloys: (♦, ◊) Pd−Rh, (▲, Δ) Pd−Pt, (●, ○) Pd−Pt−Rh. (D) Relationship between the mass change and electric charge density after potential steps to the potentials at CO prepeak region at pure Pt, Pt−Co, and Pt−Fe electrodes with CO_{ad}. (E) Cyclic voltammetry with simultaneous frequency (Δf) and motional resistance (ΔR_m) change measurements in 0.1 M CH_3OH/0.1 M NaOH for (i) a bare Pt QCM electrode, (ii) a Pt QCM electrode modified with an ionomer film with dry thickness of 210 ± 13 nm, and (iii) a Pt QCM electrode modified with an ionomer film with dry thickness of 44 ± 13 nm. Scan rate: 20 mV/s. Solid line: forward scan. Broken line: reverse scan. (A) is reprinted with permission from ref 339. Copyright 2013 American Chemistry Society. (B) is reprinted with permission from ref 341. Copyright 2020 Wiley. (C, D) are reprinted with permission from refs 343, 353, respectively, Copyright 2006, 2011 Elsevier. (D) is reprinted with permission from ref 365. Copyright by the authors 2014 American Chemistry Society.

crystal. Both smaller area and thickness result in a higher sensitivity albeit at the expense of fragility of the crystal. The add-on mass should not be larger than 0.5% of the mass of the crystal to ensure the valid utilization of the Sauerbrey equation with a reasonable sensitivity.[326] For a typical 5 MHz AT-cut quartz crystal electrode, the sensitivity constant can reach 56.6 Hz·cm^2/μg with a detectable mass change at around 10 ng/cm^2.[327] The sensitivity constant can be measured experimentally for a specific quartz crystal by electrochemical deposition of thin layers of metals, such as Ag and Cu,[328−331] or with the specific adsorption of known species.[332] Galvanostatic deposition is usually employed. The sensitivity factor can be

https://dx.doi.org/10.1021/acscatal.0c04789
ACS Catal. 2021, 11, 1136−1178

obtained by dividing the measured Δf by the Δm calculated from the charge passed for the duration of deposition.

The use of Sauerbrey equation implies several assumptions. It assumes that the deposited mass is rigid, the frequency change caused by the mass change on the electrode is independent of the radial distance from the center of the crystal, and the deposited film is distributed evenly on the electrode. However, the EQCM measurement is often nonideal. Typically, the EQCM is operated with the quartz crystal electrode immersed in a liquid electrolyte, which damps the oscillation. The frequency can be affected by the viscosity and the density of the electrolyte. If the mass deposited on the electrode remains rigid and the viscosity and the density of the electrolyte do not change during the electrochemical process, the Sauerbrey equation is generally valid. If a polymer film is deposited on the electrode, the viscoelastic effects of the polymer film with absorbed electrolyte need to be considered. Since energy dissipation results from the nonideal behavior of the viscoelastic film, a quantitative analysis with the Sauerbrey equation is not reliable under such conditions. Consequently, the analysis with polymer films has to be conducted with great caution.

Studying the oscillation, with an equivalent circuit, greatly helps characterization of deposited polymer films in contact with a liquid. The electrical equivalent of the EQCM, also known as the Butterworth-Van-Dyke (BVD) model (Figure 11C), is composed of a motional arm, with an inductor (inertial component), a capacitor (energy storing component) and a resistor (energy dissipation component) in series, and a static arm with a capacitor connecting in parallel. The static capacitor models the capacitance of the quartz crystal system, including the crystal holder and the cabling. A rigid mass deposition to the quartz crystal electrode can be described by adding an inductance to the system, while a viscous film deposition or liquid contact would increase the motional resistance, besides the inductance of the system.

With an electrical equivalent model, impedance analysis can be employed to diagnose the viscoelasticity of a polymer film and provide guidance for choosing the optimal deposition thickness for EQCM measurements. The obtained impedance (Z) and its inverse, admittance (Y), can be expressed by eqs 3 and 4, respectively:

$$Z = |Z|e^{i\theta} \tag{3}$$

$$Y = G + iB \tag{4}$$

where θ is the phase angle, G is the conductance, and B is the susceptance. An admittance plot for the corresponding BVD model is depicted in Figure 11D. Each point on the admittance locus corresponds to the admittance at a certain frequency. The resonant frequency can be found at the cross section of the locus with the real axis ($\theta = 0$). The static capacitance shifts the locus upward, resulting in two resonant frequencies, f_s and f_p (red points in Figure 11D), also in the Z–θ plot (Figure 11E). The point of maximum conductance, G_{max}, is denoted as the blue point in Figure 11D. The reciprocal of G_{max} gives the motional resistance (R_m). Therefore, an increase of the motional resistance, caused by the deposition of a polymer film or the immersion of the crystal in liquid, would lead to a smaller radius of the admittance locus. A resonant state cannot be reached if the radius of the locus is so small that it no longer crosses the real axis. As a result, the admittance locus is a convenient tool to verify whether a deposited film in a liquid environment is appropriate for EQCM measurements. The quality factor, which describes the energy stored per energy lost during the oscillation, can be calculated from the frequency at G_{max} divided by the bandwidth f_2–f_1 (eq 5), where f_1 and f_2 are the frequency at B_{max} and B_{min} respectively (Figure 11D,F).

$$Q = \frac{f_{Gmax}}{f_2 - f_1} \tag{5}$$

Q can reach 10^5 for quartz crystals in air, while it often decreases to ~3000 for quartz crystals immersed in water (liquids). For a more detailed explanation of the physics and limitations of EQCM, readers are referred to the authoritative review by Buttry and Ward.[327]

6.2. Applications of EQCM in Electrocatalysis. As a gravimetric sensor with high sensitivity, EQCM is often used to control the electrochemical preparation of catalyst materials by deposition or displacement on the electrode.[333−342] Xie et al. synthesized uniform Pt thin-film catalysts for the methanol oxidation reaction, through galvanic displacement by Pt of electrodeposited insulating materials, such as $Mn(OH)_2$,[336] CuCl,[337] and $Cu(OH)_2$.[338] The EQCM was employed to identify those deposited insulating materials. Since the molar mass (M) per electron transferred (n) can be calculated by combining Faraday's law and the Sauerbrey equation (eq 6), the deposited material can be determined from the charge (ΔQ) and the corresponding mass change (Δm), with Faraday's constant (F).

$$\frac{M}{n} = \frac{\Delta m}{\Delta Q}F \tag{6}$$

For example, in one of their studies,[332] the M/n of the deposit was calculated to be 46 g/mol, close to the theoretical value of MnO_2 converted from Mn^{2+} (86.94/2 = 43.5), which verified that the decrease in frequency at around 0.9 V in the positive scan was due to the deposition of MnO_2 on the electrode.

EQCM studies can help optimize deposition conditions. For instance, the growth mechanism of molybdenum sulfide catalysts for the hydrogen evolution reaction (HER) was investigated with the EQCM with various $(MoS_4)^{2-}$ concentrations, potential cycling range and deposition method.[339] The oxidative deposition, reductive deposition and partial corrosion processes were identified, respectively, by the potential dependent mass change profiles. It was found that the film growth speed could be controlled by varying the deposition method due to the different processes involved at different potentials, as shown by the time dependent mass change profile in Figure 12A. During the activation process of the MoS_3 deposited by anodic electrolysis, the mass decrease corresponding to the removal of one equivalent of sulfur was also observed. The formation of amorphous MoS_{3-x} after the activation, was postulated as the active material during the HER catalysis, which was further confirmed by XPS measurements.

The displacement process at the electrode can also be identified by the EQCM with eq 6. He et al. recently reported on a Cu_2S electrocatalyst for the reduction of CO_2 that was converted from a CoS_2 template via an electrochemically driven cation exchange method.[341] The mass changes at the open circuit potential, −0.07 V and −0.47 V, were compared on a gold electrode and a CoS_2 coated electrode. At open circuit (Figure 12B(i)), the mass increase on the unbiased

https://dx.doi.org/10.1021/acscatal.0c04789
ACS Catal. 2021, 11, 1136−1178

CoS_2 coated electrode indicated the physical adsorption of Cu^{2+} ions on the CoS_2 surface. When a potential was applied to the CoS_2 coated electrode, the mass increase was far lower than the theoretical mass increase for the Cu deposition process (eq 7). The difference in mass change per charge transferred on the electrode with and without CoS_2 (Figure 12B(ii)) verified the displacement process. Different processes were also proposed on the electrode at −0.07 V (loss of S^{2-}; eq 8) and −0.47 V (loss of S^{2-} and cation exchange; eqs 8−10), according to the results presented in Figure 12B(ii).

$$Cu^{2+} + 2e^- \rightarrow Cu \quad (7)$$

$$2Cu^{2+} + S_2^{2-} + 4e^- \rightarrow Cu_2S + S^{2-} \quad (8)$$

$$Co^{2+} + 2e^- \rightarrow Co \quad (9)$$

$$2Cu^{2+} + Co \rightarrow 2Cu^{+} + Co^{2+} \quad (10)$$

Catalyst degradation can be directly detected by the EQCM by monitoring the mass change during consecutive potential cycles or long-term potentiostatic measurements. The dissolution of electrodeposited noble metals and their alloys during cyclic voltammetry in acidic media was systematically studied by Łukaszewski et al.[343] The potential range, scan rate and the type of metal had a significant impact on the extent of dissolution. They found that Pt is more resistant to dissolution than Pd and Rh. Figure 12C presents the loss of mass and the change of oxide reduction peak potential with increasing potential cycles for different Pd alloys.[343] The alloys containing Pt exhibited a slower mass change after many cycles. This correlated with the enriched Pt content on the surface that was more difficult to be stripped, as determined from the peak potential of oxide reduction. The EQCM study of the dissolution of catalysts was further applied to electrodeposited Ru,[344] a sputtered Pt alloy,[345] drop-cast Pt/C nanoparticles[331,346] and non-noble metal catalysts.[347,348] Thereinto, Moore et al.[331] demonstrated via EQCM with potential cycling and potential holds, that the addition of IrO_2 to Pt/C mitigated the degradation of Pt/C catalyst at high potentials in proton exchange membrane fuel cells, because with IrO_2, the oxygen evolution reaction would proceed, instead of the carbon corrosion and Pt dissolution. More recently, Luo et al. reported a Y-stabilized ZrO_2 (YSZ) catalysts for the nitrogen reduction reaction with insights into the deactivation mechanism.[349] Unlike the dissolution case, a mass increase of the ZrO_2 catalyst was observed by the EQCM after long-term stability tests with drastically decreased catalytic activity, while both the mass and the activity of YSZ catalyst were stable. The mass increase was ascribed to the filling of O vacancies in the nanocomposite, which lowered the nitrogen reduction activity. The O-vacancy active sites of C@ZrO_2 catalyst were approximately quantified as 0.672 μg/mg by EQCM.

In electrocatalysis, the use of EQCM not only facilitates the characterization of catalyst evolution on the electrode during the preparation or degradation processes, but also enables mechanistic studies of catalytic processes including intermediate adsorption and solvent dynamics in catalyst or membrane materials. The mass change detection on the electrode enables the tracking of electrochemically inert neutral species involved in the interfacial electrocatalysis, which cannot be carried out by other methods for intermediate detection, such as rotating-ring disk electrode voltammetry and others.

The EQCM has been specifically applied to studies of electrochemical reactions with intermediate adsorption, such as the oxidation of CO and small organic molecules adsorbed on noble metal and alloy catalysts,[250,335,350−356] the adsorption of oxygen species and anions on Pt-based electrodes during the oxygen reduction reaction,[357,358] and others. Combining the EQCM with double-potential chronoamperometry, Uchida et al. were able to quantitatively analyze the elementary steps of CO oxidation on Pt alloy electrodes.[353] Potential steps were employed to analyze the prepeak and the main peak of CO oxidation, respectively. By plotting the mass change vs the increase in charge density, M/n values of the processes can be calculated, according to eq 6. Figure 12D presents an example for the analysis of the elementary reactions at potentials within the CO prepeak on Pt, Pt−Co, and Pt−Fe. A steep drop followed by a gradual decrease were found on all three surfaces, suggesting a similar mechanism. The M/n values of the two steps were determined to be −45 and −10, which can be ascribed to the loss of $COOH_{ad}$ with one electron transferred (eq 11) and the oxidation of CO_{ad} with the loss of two electrons (eq 12), respectively. They proposed that the removal of the small amounts of $COOH_{ad}$ provides vacant sites that promote the second step, which involves the supply of H_2O. The less negative slope for the second step might be due to the adsorption of H_2O and ClO_4^- from the solution.

$$Pt\text{-}COOH_{ad} \rightarrow Pt + CO_2 + H^+ + e^- \frac{M}{n} = -45 \quad (11)$$

$$Pt\text{-}CO_{ad} + H_2O \rightarrow Pt + CO_2 + 2H^+ + 2e^- \frac{M}{n} = -14 \quad (12)$$

The intercalation of ions and water molecules from the electrolyte into catalysts during electrocatalytic processes, which has no contribution to the electrochemical response, can also be detected by EQCM. In a study on electrodeposited cobalt for the oxygen evolution reaction by Hassan et al.,[359] different crystalline phases of deposited cobalt were distinguished by the different mass change behaviors during potential cycling. The greater mass increase of cobalt deposited without citrate, was attributed to the formation of α-$Co(OH)_2$, which has a larger interlayer spacing (7.9 Å) for the intercalation of H_2O and OH^-; than the more compact β-$Co(OH)_2$ (4.6 Å), derived from β-Co deposited with citrate. Similar studies have also been applied to the investigation of ion incorporation and phase transformation in the layered structures of Co or Ni materials in electrocatalysis.[360−364]

The EQCM also provides real-time information on the solvent and ion dynamics on polymer modified electrodes during electrochemical processes. We employed the EQCM to study the ion exchange processes of an anion exchange membrane designed for alkaline fuel cells.[365] Acoustic impedance analysis was conducted prior to the EQCM measurements to characterize the viscoelastic effects of the alkaline ionomer films immersed in water. The changes in both the frequency and motional resistance were monitored on a bare electrode and ionomer-coated electrodes (Figure 12E), during the methanol oxidation reaction, where CO_3^{2-} and $HCOO^-$ were locally generated at the electrode. The frequency change for the 210 nm film modified electrode (Figure 12E(ii)), due to the anion exchange in the film, was over 1 order of magnitude larger than that due to Pt-oxide formation at the bare electrode (Figure 12E(i)). Meanwhile,

https://dx.doi.org/10.1021/acscatal.0c04789
ACS Catal. 2021, 11, 1136−1178

the significantly greater decrease in motional resistance during methanol oxidation, on the 210 nm film modified electrode (Figure 12E(ii)), compared to that on a 44 nm film modified electrode (Figure 12E(iii)), reflected viscoelastic changes, i.e., deswelling of the thicker ionomer film driven by the Faradaic processes. It was inferred from the simultaneous decrease in frequency and motional resistance, that the incorporation of CO_3^{2-} and $HCOO^-$ into the ionomer film was accompanied by egress of water from the film.

In summary, as an *in situ* analytical technique with high sensitivity, the EQCM has been employed in a wide range of studies on various electrode interfaces, ranging from metal catalysts to polymer thin films under different environments. Nevertheless, the poor selectivity limits the mass change signal and restricts the quantitative analysis of more complicated processes. If more than one species is involved in the mass change process, the M/n value determined from eq 6 will not be adequate to identify nor distinguish them from each other. Hardwick et al. recently proposed an approach to deconvolve the contributions from multiple species by EQCM assisted by DFT calculations, which sample and screen the possible stoichiometric coefficients on an energy basis.[364] It is also highly valuable to combine EQCM with other *in situ* techniques for complementary information, such as DEMS,[260] *in situ* Raman spectroscopy, and others for characterizing reaction intermediates and elementary steps during electrocatalysis.

7. CONCLUSIONS

In this review, we have introduced various *in situ/operando* methods and their applications for understanding interfacial electrocatalysis. In particular, we have reviewed *operando* synchrotron-based XAS and surface-sensitive X-ray scattering for providing chemical and structural information on electrocatalysts at electrode−electrolyte interfaces for working electrocatalysts in realistic reactors and/or devices. Moving from macroscopic to microscopic levels, we introduced the applications of *ex situ* STEM and EELS/EDX, which can provide atomic-scale structural, compositional, and bonding information These *ex situ* measurements are instrumental for resolving the complex catalyst surfaces and provide valuable guidance for further *in situ* TEM experiments. *In situ* electrochemical liquid-cell STEM and EELS/EDX are helping unveil numerous important electrocatalytic reactions in solution phase with nanometer-scale or higher resolution. *In situ* liquid-cell STEM provides valuable insights for identifying the primary catalyst degradation mechanism(s) such as coalescence and/or Ostwald ripening of nanoparticles, dissolution/redeposition, and support corrosion under catalytically relevant reaction conditions. These studies will further our knowledge of how catalysts degrade over time and provide rational guidance criteria to deliberately design more active, selective and durable electrocatalysts. *In situ* heating and gas-phase TEM enables the investigation of gas-phase (electro)-catalytic reactions at the atomic scale under controlled temperature and gas environments. *Operando* X-ray and STEM in gas/liquid phases can serve as microreactors to investigate the dynamic structural evolution of materials during catalyst synthesis, catalytic reactions, and extended durability tests. SECM offers an opportunity for the direct probing of local activity and selectivity of individual heterogeneous nanoparticle electrocatalysts. DEMS and EQCM provide important mechanistic insights on catalyst selectivity and distinction of products and reaction intermediates, as well as stability during electrochemical reactions. The continuous improvement of *in situ/operando* methods will advance our fundamental understanding of the interfacial electrocatalysis and may lead to ground-breaking advances in sustainable and renewable energy applications.

AUTHOR INFORMATION

Corresponding Author

Héctor D. Abruña − *Department of Chemistry and Chemical Biology, Cornell University, Ithaca, New York 14853, United States;* orcid.org/0000-0002-3948-356X; Email: hda1@cornell.edu

Authors

Yao Yang − *Department of Chemistry and Chemical Biology, Cornell University, Ithaca, New York 14853, United States;* orcid.org/0000-0003-0321-3792

Yin Xiong − *Department of Chemistry and Chemical Biology, Cornell University, Ithaca, New York 14853, United States;* orcid.org/0000-0002-8560-0894

Rui Zeng − *Department of Chemistry and Chemical Biology, Cornell University, Ithaca, New York 14853, United States;* orcid.org/0000-0002-7577-767X

Xinyao Lu − *Department of Chemistry and Chemical Biology, Cornell University, Ithaca, New York 14853, United States;* orcid.org/0000-0002-2649-5721

Mihail Krumov − *Department of Chemistry and Chemical Biology, Cornell University, Ithaca, New York 14853, United States*

Xin Huang − *School of Applied and Engineering Physics and Cornell High Energy Synchrotron Source (CHESS), Cornell University, Ithaca, New York 14853, United States;* orcid.org/0000-0001-5404-4437

Weixuan Xu − *Department of Chemistry and Chemical Biology, Cornell University, Ithaca, New York 14853, United States*

Hongsen Wang − *Department of Chemistry and Chemical Biology, Cornell University, Ithaca, New York 14853, United States;* orcid.org/0000-0001-7926-2895

Francis J. DiSalvo − *Department of Chemistry and Chemical Biology, Cornell University, Ithaca, New York 14853, United States*

Joel. D. Brock − *School of Applied and Engineering Physics and Cornell High Energy Synchrotron Source (CHESS), Cornell University, Ithaca, New York 14853, United States*

David A. Muller − *School of Applied and Engineering Physics, Cornell University, Ithaca, New York 14853, United States; Kavli Institute at Cornell for Nanoscale Science, Ithaca, New York 14853, United States;* orcid.org/0000-0003-4129-0473

Complete contact information is available at: https://pubs.acs.org/10.1021/acscatal.0c04789

Author Contributions

#Y.Y. and Y.X. contributed equally. Y.Y. wrote the *in situ/operando* X-ray and S/TEM sections. Y.X. wrote the *ex situ* S/TEM sections and designed the TOC, and M.K. wrote the SECM section. R.Z. wrote the DEMS section and X.L. wrote the EQCM section. X.H. and H.W. revised the X-ray and DEMS sections, respectively, and W.X. performed editorial revisions. The manuscript was written through contributions of all coauthors under the guidance of H.D.A, D.A.M, J.D.B, and

https://dx.doi.org/10.1021/acscatal.0c04789
ACS Catal. 2021, 11, 1136−1178

F.J.D. All authors have given approval to the final version of the manuscript.

Notes

The authors declare no competing financial interest.

■ ACKNOWLEDGMENTS

This work was supported by the Center for Alkaline-Based Energy Solutions (CABES), an Energy Frontier Research Center (EFRC) program supported by the U.S. Department of Energy, under Grant DE-SC0019445. This work made use of facilities at the Cornell Center for Materials Research (CCMR) which are supported through the National Science Foundation Materials Research Science and Engineering Center (NSF MRSEC) program (DMR-1719875). This work is based upon research conducted at the Cornell High Energy Synchrotron Source (CHESS), which is supported by the National Science Foundation under Award No. DMR-1332208. This work was supported in part (R.Z., X.L., H.W.) by the Air Force Office of Scientific Research under Award No. FA9550-18-1-0420. MURI: Molecular Level Studies of Solid−Liquid Interfaces in Electrochemical Processes.

■ REFERENCES

(1) Abruña, H. D. *Electrochemical Interface: Modern Techniques for In Situ Interface Characterization*; VCH: New York, 1991, p 225.
(2) Abruña, H. D.; White, J. H.; Albarelli, M. J.; Bommarito, G. M.; Bedzyk, M. J.; McMillan, M. Is There Any Beam Yet? Uses of Synchrotron Radiation in the in Situ Study of Electrochemical Interfaces. *J. Phys. Chem.* **1988**, *92*, 7045−7052.
(3) Russell, A. E.; Rose, A. X-ray Absorption Spectroscopy of Low Temperature Fuel Cell Catalysts. *Chem. Rev.* **2004**, *104*, 4613−4635.
(4) Weckhuysen, B. M. Snapshots of a Working Catalyst: Possibilities and Limitations of *In Situ* Spectroscopy in the Field of Heterogeneous Catalysis. *Chem. Commun.* **2002**, 97−110.
(5) Bañares, M. A. Operando Methodology: Combination of In Situ Spectroscopy and Simultaneous Activity Measurements under Catalytic Reaction Conditions. *Catal. Today* **2005**, *100*, 71−77.
(6) Wang, Y.; Yang, Y.; Jia, S.; Wang, X.; Lyu, K.; Peng, Y.; Zheng, H.; Wei, X.; Ren, H.; Xiao, L.; Wang, J.; Muller, D. A.; Abruña, H. D.; Hwang, B. J.; Lu, J.; Zhuang, L. Synergistic Mn-Co Catalyst Outperforms Pt on High-Rate Oxygen Reduction for Alkaline Polymer Electrolyte Fuel Cells. *Nat. Commun.* **2019**, *10*, 1506.
(7) Yang, Y.; Wang, Y.; Xiong, Y.; Huang, X.; Shen, L.; Huang, R.; Wang, H.; Pastore, J. P.; Yu, S.-H.; Xiao, L.; Brock, J. D.; Zhuang, L.; Abruña, H. D. In Situ X-ray Absorption Spectroscopy of a Synergistic Co-Mn Oxide Catalyst for the Oxygen Reduction Reaction. *J. Am. Chem. Soc.* **2019**, *141*, 1463−1466.
(8) Xiong, Y.; Yang, Y.; Feng, X.; DiSalvo, F.; Abruña, H. D. A Strategy for Increasing the Efficiency of the Oxygen Reduction Reaction in Mn-Doped Cobalt Ferrites. *J. Am. Chem. Soc.* **2019**, *141*, 4412−4421.
(9) Wiltshire, R. J. K.; King, C. R.; Rose, A.; Wells, P. P.; Hogarth, M. P.; Thompsett, D.; Russell, A. E. A PEM Fuel Cell for in situ XAS Studies. *Electrochim. Acta* **2005**, *50*, 5208−5217.
(10) Imai, H.; Izumi, K.; Matsumoto, M.; Kubo, Y.; Kato, K.; Imai, Y. In Situ and Real-Time Monitoring of Oxide Growth in a Few Monolayers at Surfaces of Platinum Nanoparticles in Aqueous Media. *J. Am. Chem. Soc.* **2009**, *131*, 6293−6300.
(11) Erickson, E. M.; Thorum, M. S.; Vasić, R.; Marinković, N. S.; Frenkel, A. I.; Gewirth, A. A.; Nuzzo, R. G. In Situ Electrochemical X-ray Absorption Spectroscopy of Oxygen Reduction Electrocatalysis with High Oxygen Flux. *J. Am. Chem. Soc.* **2012**, *134*, 197−200.
(12) Casalongue, H. S.; Kaya, S.; Viswanathan, V.; Miller, D. J.; Friebel, D.; Hansen, H. A.; Nørskov, J. K.; Nilsson, A.; Ogasawara, H. Direct Observation of the Oxygenerated Species during Oxygen Reduction on a Platinum Fuel Cell Cathode. *Nat. Commun.* **2013**, *4*, 2817.
(13) Becknell, N.; Kang, Y.; Chen, C.; Resasco, J.; Kornienko, N.; Guo, J.; Marković, N. M.; Somorjai, G. A.; Stamenković, V. R.; Yang, P. Atomic Structure of Pt_3Ni Nanoframe Electrocatalysts by In Situ X-ray Absorption Spectroscopy. *J. Am. Chem. Soc.* **2015**, *137*, 15817−15824.
(14) Sasaki, K.; Marinkovic, N.; Isaacs, H. S.; Adzic, R. R. Synchrotron-Based In Situ Characterization of Carbon-Supported Platinum and Platinum Monolayer Electrocatalysts. *ACS Catal.* **2016**, *6*, 69−76.
(15) Gorlin, Y.; Lassalle-Kaiser, B.; Benck, J. D.; Gul, S.; Webb, S. M.; Yachandra, V. K.; Yano, J.; Jaramillo, T. F. In Situ X-ray Absorption Spectroscopy Investigation of a Bifunctional Manganese Oxide Catalyst with High Activity for Electrochemical Water Oxidation and Oxygen Reduction. *J. Am. Chem. Soc.* **2013**, *135*, 8525−8534.
(16) Kanan, M. W.; Yano, J.; Surendranath, Y.; Dincá, M.; Yachandra, V. K.; Nocera, D. G. Structure and Valency of a Cobalt-Phosphate Water Oxidation Catalyst Determined by in Situ X-ray Spectroscopy. *J. Am. Chem. Soc.* **2010**, *132*, 13692−13701.
(17) Bates, M.; Jia, Q.; Doan, H.; Liang, W.; Mukerjee, S. Charge-Transfer Effects in Ni-Fe and Ni-Fe-Co Mixed-Metal Oxides for the Alkaline Oxygen Evolution Reaction. *ACS Catal.* **2016**, *6*, 155−161.
(18) Risch, M.; Stoerzinger, K. A.; Han, B.; Regier, T. Z.; Peak, D.; Sayed, Y.; Wei, C.; Xu, Z.; Shao-Horn, Y. Redox Processes of Manganese Oxide in Catalyzing Oxygen Evolution and Reduction: An in Situ Soft X-Ray Absorption Spectroscopy Study. *J. Phys. Chem. C* **2017**, *121*, 17682−17692.
(19) Weir, M. G.; Myers, V. S.; Frenkel, A. I.; Crooks, R. M. In situ X-ray Absorption Analysis of ∼1.8 nm Dendrimer-Encapsulated Pt Nanoparticles during Electrochemical CO Oxidation. *ChemPhysChem* **2010**, *11*, 2942−2950.
(20) Osmieri, L.; Ahluwalia, R. K.; Wang, X.; Chung, H. T.; Yin, X.; Kropf, A. J.; Park, J.; Cullen, D. A.; More, K. L.; Zelenay, P.; Myers, D. J.; Neyerlin, K. C. Elucidation of Fe-N-C Electrocatalyst Active Site Functionality via In-Situ X-Ray Absorption and Operando Determination of Oxygen Reduction Reaction Kinetics in a PEFC. *Appl. Catal., B* **2019**, *257*, 117929.
(21) Tylus, U.; Jia, Q.; Strickland, K.; Ramaswamy, N.; Serov, A.; Atanassov, P.; Mukerjee, S. Elucidating Oxygen Reduction Active Sites in Pyrolyzed Metal-Nitrogen Coordinated Non-Precious-Metal Electrocatalyst Systems. *J. Phys. Chem. C* **2014**, *118*, 8999−9008.
(22) Strickland, K.; Miner, E.; Jia, Q.; Tylus, U.; Ramaswamy, N.; Liang, W.; Sougrati, M.-T.; Jaouen, F.; Mukerjee, S. Highly Active Oxygen Reduction Non-Platinum Group Metal Electrocatalyst Without Direct Metal-Nitrogen Coordination. *Nat. Commun.* **2015**, *6*, 7343.
(23) Glatzel, P.; Singh, J.; Kvashnina, K. O.; van Bokhoven, J. A. In Situ Characterization of the 5d Density of States of Pt Nanoparticles upon Adsorption of CO. *J. Am. Chem. Soc.* **2010**, *132*, 2555−2557.
(24) Glatzel, P.; Bergmann, U. High Resolution 1s Core Hole X-ray Spectroscopy in 3d Transition Metal Complexes—Electronic and Structural Information. *Coord. Chem. Rev.* **2005**, *249*, 65−95.
(25) Friebel, D.; Viswanathan, V.; Miller, D. J.; Anniyev, T.; Ogasawara, H.; Larsen, A. H.; O'Grady, C. P.; Nørskov, J. K.; Nilsson, A. Balance of Nanostructure and Bimetallic Interactions in Pt Model Fuel Cell Catalysts: In Situ XAS and DFT Study. *J. Am. Chem. Soc.* **2012**, *134*, 9664−9671.
(26) Friebel, D.; Miller, D. J.; O'Grady, C. P.; Anniyev, T.; Bargar, J.; Bergmann, U.; Ogasawara, H.; Wikfeldt, K. T.; Pettersson, L. G. M.; Nilsson, A. In situ X-ray Probing Reveals Fingerprints of Surface Platinum Oxide. *Phys. Chem. Chem. Phys.* **2011**, *13*, 262−266.
(27) Friebel, D.; Miller, D. J.; Nordlund, D.; Ogasawara, H.; Nilsson, A. Degradation of Bimetallic Model Electrocatalysts: An in Situ X-Ray Absorption Spectroscopy Study. *Angew. Chem., Int. Ed.* **2011**, *50*, 10190−10192.

https://dx.doi.org/10.1021/acscatal.0c04789
ACS Catal. 2021, 11, 1136−1178

(28) Viswanathan, R.; Hou, G. Y.; Liu, R. X.; Bare, S. R.; Modica, F.; Mickelson, G.; Segre, C. U.; Leyarovska, N.; Smotkin, E. S. *J. Phys. Chem. B* **2002**, *106*, 3458−3465.
(29) Mukerjee, S.; Srinivasan, S.; Soriaga, M. P.; McBreen, J. Role of Structural and Electronic Properties of Pt and Pt Alloys on Electrocatalysts of Oxygen Reduction. *J. Electrochem. Soc.* **1995**, *142*, 1409−1421.
(30) Roth, C.; Martz, N.; Buhrmester, T.; Scherer, J.; Fuess, H. In-Situ XAFS Fuel Cell Measurements of a Carbon-Supported Pt-Ru Anode Electrocatalyst in Hydrogen and Direct Methanol Operation. *Phys. Chem. Chem. Phys.* **2002**, *4*, 3555−3557.
(31) Greco, G.; Witkowska, A.; Minicucci, M.; Olivi, L.; Principi, E.; Dsoke, S.; Moretti, A.; Marassi, R.; Di Cicco, A. Di; Trieste, S. Local Ordering Changes in Pt-Co Nanocatalyst Induced by Fuel Cell Working Conditions. *J. Phys. Chem. C* **2012**, *116*, 12791−12802.
(32) Ishiguro, N.; Saida, T.; Uruga, T.; Nagamatsu, S.; Sekizawa, O.; Nitta, K.; Yamamoto, T.; Ohkoshi, S.; Iwasawa, Y.; Yokoyama, T.; Tada, M. Operando Time-Resolved X-ray Absorption Fine Structure Study for Surface Events on a Pt_3Co/C Cathode Catalyst in a Polymer Electrolyte Fuel Cell during Voltage-Operating Processes. *ACS Catal.* **2012**, *2*, 1319−1330.
(33) Ishiguro, N.; Kityakarn, S.; Sekizawa, O.; Uruga, T.; Sasabe, T.; Nagasawa, K.; Yokoyama, T.; Tada, M. Rate Enhancements in Structural Transformations of Pt-Co and Pt-Ni Bimetallic Cathode Catalysts in Polymer Electrolyte Fuel Cells Studied by in Situ Time-Resolved X-ray Absorption Fine Structure. *J. Phys. Chem. C* **2014**, *118*, 15874−15883.
(34) Higashi, K.; Samjeske, G.; Takao, S.; Kaneko, T.; Sekizawa, O.; Uruga, T.; Iwasawa, Y. The Relationship between the Active Pt Fraction in a PEFC Pt/C Catalyst and the ECSA and Mass Activity during Start-Up/Shut-Down Degradation by in Situ Time-Resolved XAFS Technique. *J. Phys. Chem. C* **2017**, *121*, 22164−22177.
(35) Tada, M.; Murata, S.; Asakoka, T.; Hiroshima, K.; Okumura, K.; Tanida, H.; Uruga, T.; Nakanishi, H.; Matsumoto, S.-i.; Inada, Y.; Nomura, M.; Iwasawa, Y. In Situ Time-resolved Dynamic Surface Events on the Pt/C Cathode in a Fuel Cell under Operando Conditions. *Angew. Chem., Int. Ed.* **2007**, *46*, 4310−4315.
(36) Stamenković, V. R.; Mun, B. S.; Arenz, M.; Mayrhofer, K. J. J.; Lucas, C. A.; Wang, G.; Ross, P. N.; Marković, N. M. Trends in Electrocatalysis on Extended and Nanoscale Pt-Bimetallic Alloy Surfaces. *Nat. Mater.* **2007**, *6*, 241−247.
(37) Stamenković, V. R.; Fowler, B.; Mun, B. S.; Wang, G.; Ross, P. N.; Lucas, C. A.; Marković, N. M. Improved Oxygen Reduction Activity on $Pt_3Ni(111)$ via Increased Surface Site Availability. *Science* **2007**, *315*, 493−497.
(38) Omasta, T. J.; Park, A. M.; Lamanna, J. M.; Zhang, Y.; Peng, X.; Wang, L.; Jacobson, D. L.; Varcoe, J. R.; Hussey, D. S.; Pivovar, B. S.; et al. Beyond Catalysis and Membranes: Visualizing and Solving the Challenge of Electrode Water Accumulation and Flooding in AEMFCs. *Energy Environ. Sci.* **2018**, *11*, 551−558.
(39) Citrin, P. H. X-ray Absorption Spectroscopy Applied to Surface Structure: SEXAFS and NEXAFS. *Surf. Sci.* **1994**, *299*, 199−218.
(40) Samant, M. G.; Toney, M. F.; Borges, G. L.; Blum, L.; Melroy, O. R. In Situ Grazing Incidence X-Ray Diffraction Study of Electrochemically Deposited Pb Monolayers on Ag(111). *Surf. Sci.* **1988**, *193*, L29−L36.
(41) Finnefrock, A. C.; Ringland, K. L.; Brock, J. D.; Buller, L. J.; Abruña, H. D. Nucleation and Ordering of an Electrodeposited Two-Dimensional Crystal: Real-Time X-Ray Scattering and Electronic Measurements. *Phys. Rev. Lett.* **1998**, *81*, 3459−3462.
(42) Toney, M. F.; Howard, J. N.; Richer, J.; Borges, G. L.; Gordon, J. G.; Melroy, O. R.; Wiesler, D. G.; Yee, D.; Sorensen, L. B. Voltage-Dependent Ordering of Water Molecules at an Eelectrode-Electrolyte Interface. *Nature* **1994**, *368*, 444−446.
(43) Grunder, Y.; Lucas, C. Surface X-ray Diffraction Studies of Single Crystal Electrocatalysts. *Nano Energy* **2016**, *29*, 378−393.
(44) Fuoss, P. H.; Brennan, S. Surface Sensitive X-ray Scattering. *Annu. Rev. Mater. Sci.* **1990**, *20*, 365−390.
(45) Feidenhans'l, R. Surface Structure Determination By X-Ray Diffraction. *Surf. Sci. Rep.* **1989**, *10*, 105−188.
(46) Huang, X.; Plaza, M.; Ko, P.; Abruña, H. D.; Brock, J. D. Relaxation of Asymmetric Crystallographic Tilt: *In situ* X-ray Diffraction Studies of Epitaxial Electrodeposition of Bismuth on GaAs (110). *J. Appl. Phys.* **2018**, *124*, 035301.
(47) Bommarito, G. M.; Acevedo, D.; Abruña, H. D. In Situ Monitoring of Electrochemically Induced Roughening with the Crystal Truncation Rod Technique. *J. Phys. Chem.* **1992**, *96*, 3416−3419.
(48) Cheng, L.; Fenter, P.; Nagy, K. L.; Schlegel, M. L.; Sturchio, N. C. Molecular-Scale Density Oscillations in Water Adjacent to a Mica Surface. *Phys. Rev. Lett.* **2001**, *87*, 156103.
(49) Kendelewicz, T.; Kaya, S.; Newberg, J. T.; Bluhm, H.; Mulakaluri, N.; Moritz, W.; Scheffler, M.; Nilsson, A.; Pentcheva, R.; Brown, G. E. X-ray Photoemission and Density Functional Theory Study of the Interaction of Water Vapor with the $Fe_3O_4(001)$ Surface at Near-Ambient Conditions. *J. Phys. Chem. C* **2013**, *117*, 2719−2733.
(50) Plaza, M.; Huang, X.; Ko, J. Y. P.; Shen, M.; Simpson, B. H.; Rodriguez-Lopez, J.; Ritzert, N. L.; Letchworth-Weaver, K.; Gunceler, D.; Schlom, D. G.; Arias, T. A.; Brock, J. D.; Abruna, H. D. Structure of the Photo-Catalytically Active Surface of $SrTiO_3$. *J. Am. Chem. Soc.* **2016**, *138*, 7816−7819.
(51) Lister, T. E.; Chu, Y. S.; Cullen, W. G.; You, H.; Yonco, R. M.; Mitchell, J. F.; Nagy, Z. Electrochemical and X-ray Scattering Study of Well Defined RuO_2 Single Crystal Surfaces. *J. Electroanal. Chem.* **2002**, *524*, 201−218.
(52) Nakamura, M. New Insights on Structural Dynamics of Electrochemical Interface by Time-Resolved Surface X-ray Diffraction. *Curr. Opin. Electrochem.* **2019**, *14*, 200−205.
(53) Rao, R. R.; Kolb, M. J.; Halck, N. B.; Pedersen, A. F.; Mehta, A.; You, H.; Stoerzinger, K. A.; Feng, Z.; Hansen, H. A.; Zhou, H.; Giordano, L.; Rossmeisl, J.; Vegge, T.; Chorkendorff, I.; Stephens, I. E. L.; Shao-Horn, Y. Towards Identifying the Active Sites on RuO_2 (110) in Catalyzing Oxygen Evolution. *Energy Environ. Sci.* **2017**, *10*, 2626−2637.
(54) Rao, R. R.; Kolb, M. J.; Giordano, L.; Pedersen, A. F.; Katayama, Y.; Hwang, J.; Mehta, A.; You, H.; Lunger, J. R.; Zhou, H.; Halck, N. B.; Vegge, T.; Chorkendorff, I.; Stephens, I. E. L.; Shao-Horn, Y. *Operando* Identification of Site-Dependent Water Oxidation Activity on Ruthenium Dioxide Single-Crystal Surfaces. *Nat. Catal.* **2020**, *3*, 516−525.
(55) Lucas, C. A.; Marković, N. M.; Grgur, B. N.; Ross, P. N. Structural Effects During CO Adsorption on Pt-Bimetallic Surfaces: I. The Pt(100) Electrode. *Surf. Sci.* **2000**, *448*, 65−76.
(56) Lucas, C. A.; Thompson, P.; Grunder, Y.; Marković, N. M. The Structure of the Electrochemical Double Layer: Ag(111) in Alkaline Electrolyte. *Electrochem. Commun.* **2011**, *13*, 1205−1208.
(57) Stamenković, V. R.; Arenz, M.; Lucas, C. A.; Gallagher, M. E.; Ross, P. N.; Marković, N. R. Surface Chemistry on Bimetallic Alloy Surfaces: Adsorption of Anions and Oxidation of CO on $Pt_3Sn(111)$. *J. Am. Chem. Soc.* **2003**, *125*, 2736−2745.
(58) Fowler, B.; Lucas, C. A.; Omer, A.; Wang, G.; Stamenković, V. R.; Marković, N. R. Segregation and Stability at $Pt_3Ni(111)$ Surfaces and $Pt_{75}Ni_{25}$ Nanoparticles. *Electrochim. Acta* **2008**, *53*, 6076−6080.
(59) Lucas, C. A.; Thompson, P.; Cormack, M.; Brownrigg, A.; Fowler, B.; Strmcnik, D.; Stamenković, V. R.; Greeley, J.; Menzel, A.; You, H.; Marković, N. R. Temperature-Induced Ordering of Metal/Adsorbate Structures at Electrochemical Interfaces. *J. Am. Chem. Soc.* **2009**, *131*, 7654−7661.
(60) Abruña, H. D.; Bommarito, G. M.; Acevedo, D. The Study of Solid/Liquid Interfaces with X-ray Standing Waves. *Science* **1990**, *250*, 69−74.
(61) Gomez, R.; Yee, H. S.; Bommarito, G. M.; Feliu, J. M.; Abruña, H. D. Anion Effects and the Mechanism of Cu UPD on Pt(111): X-ray and Electrochemical Studies. *Surf. Sci.* **1995**, *335*, 101−109.
(62) Abruña, H. D.; Bommarito, G. M.; Yee, H. S. X-ray Standing Waves and Surface EXAFS Studies of Electrochemical Interfaces. *Acc. Chem. Res.* **1995**, *28*, 273−279.

https://dx.doi.org/10.1021/acscatal.0c04789
ACS Catal. 2021, 11, 1136−1178

(63) Nemsak, S.; Shavorskiy, A.; Karslioglu, O.; Zegkinoglou, I.; Rattanachata, A.; Conlon, C. S.; Keqi, A.; Greene, P. K.; Burks, E. C.; Salmassi, F.; Gullikson, E. M.; Yang, S.-H.; Liu, K.; Bluhm, H.; Fadley, C. S. Concentration and Chemical-State Profiles at Heterogeneous Interfaces with Sub-Nm Accuracy from Standing-Wave Ambient-Pressure Photoemission. *Nat. Commun.* **2014**, *5*, 5441.
(64) Strmcnik, D.; Kodama, K.; van der Vliet, D.; Greeley, J.; Stamenković, V. R.; Marković, N. R. The Role of Non-Covalent Interactions in Electrocatalytic Fuel-Cell Reactions on Platinum. *Nat. Chem.* **2009**, *1*, 466−472.
(65) Stoffelsma, C.; Rodriguez, P.; Garcia, G.; Garcia-Araez, N.; Strmcnik, D.; Markovic, N. M.; Koper, M. T. M. Promotion of the Oxidation of Carbon Monoxide at Stepped Platinum Single-Crystal Electrodes in Alkaline Media by Lithium and Beryllium Cations. *J. Am. Chem. Soc.* **2010**, *132*, 16127−16133.
(66) Chen, X.; McCrum, I. T.; Schwarz, K. A.; Janik, M. J.; Koper, M. T. M. Co-Adsorption of Cations as the Cause of the Apparent PH Dependence of Hydrogen Adsorption on a Stepped Platinum Single-Crystal Electrode. *Angew. Chem., Int. Ed.* **2017**, *56*, 15025−15029.
(67) Smith, M. C.; Gilbert, J. A.; Mawdsley, J. R.; Seifert, S.; Myers, D. J. In Situ Small-Angle X-Ray Scattering Observation of Pt Catalyst Particle Growth During Potential Cycling. *J. Am. Chem. Soc.* **2008**, *130*, 8112−8113.
(68) Wakisaka, M.; Suzuki, H.; Mitsui, S.; Uchida, H.; Watanabe, M. Identification and Quantification of Oxygen Species Adsorbed on Pt(111) Single-Crystal and Polycrystalline Pt Electrodes by Photoelectron Spectroscopy. *Langmuir* **2009**, *25*, 1897−1900.
(69) Casalongue, H. S.; Kaya, S.; Viswanathan, V.; Miller, D. J.; Friebel, D.; Hansen, H. A.; Nørskov, J. K.; Nilsson, A.; Ogasawara, H. Direct Observation of the Oxygenated Species during Oxygen Reduction on a Platinum Fuel Cell Cathode. *Nat. Commun.* **2013**, *4*, 2817.
(70) Favaro, M.; Jeong, B.; Ross, P. N.; Yano, J.; Hussain, Z.; Liu, Z.; Crumlin, E. J. Unravelling the Electrochemical Double Layer by Direct Probing of the Solid/Liquid Interface. *Nat. Commun.* **2016**, *7*, 12695.
(71) Schiros, T.; Ogasawara, H.; Naslund, L.-A.; Andersson, K. J.; Ren, J.; Meng, S.; Karlberg, G. S.; Odelius, M.; Nilsson, A.; Pettersson, L. G. M. Cooperativity in Surface Bonding and Hydrogen Bonding of Water and Hydroxyl at Metal Surfaces. *J. Phys. Chem. C* **2010**, *114*, 10240−10248.
(72) Frenkel, A. I.; Wang, Q.; Marinkovic, N.; Chen, J. G.; Barrio, L.; Si, R.; Camara, A. L.; Estrella, A. M.; Rodriguez, J. A.; Hanson, J. C. Combining X-Ray Absorption and X-Ray Diffraction Techniques for in Situ Studies of Chemical Transformations in Heterogeneous Catalysis: Advantages and Limitations. *J. Phys. Chem. C* **2011**, *115*, 17884−17890.
(73) Smith, M. C.; Gilbert, J. A.; Mawdsley, J. R.; Seifert, S.; Myers, D. J. In Situ Small-Angle X-Ray Scattering Observation of Pt Catalyst Particle Growth During Potential Cycling. *J. Am. Chem. Soc.* **2008**, *130*, 8112−8113.
(74) Gilbert, J. A.; Kariuki, N. N.; Subbaraman, R.; Kropf, A. J.; Smith, M. C.; Holby, E. F.; Morgan, D.; Myers, D. J. In Situ Anomalous Small-Angle X-ray Scattering Studies of Platinum Nanoparticle Fuel Cell Electrocatalyst Degradation. *J. Am. Chem. Soc.* **2012**, *134*, 14823−14833.
(75) Povia, M.; Herranz, J.; Binninger, T.; Nachtegaal, M.; Diaz, A.; Kohlbrecher, J.; Abbott, D. F.; Kim, B.-J.; Schmidt, T. J. Combining SAXS and XAS To Study the Operando Degradation of Carbon-Supported Pt-Nanoparticle Fuel Cell Catalysts. *ACS Catal.* **2018**, *8*, 7000−7015.
(76) Arruda, T. M.; Shyam, B.; Ziegelbauer, J. M.; Mukerjee, S.; Ramaker, D. E. Investigation into the Competitive and Site-Specific Nature of Anion Adsorption on Pt Using In Situ X-ray Absorption Spectroscopy. *J. Phys. Chem. C* **2008**, *112*, 18087−18097.
(77) Hashimoto, H.; Naiki, T.; Eto, T.; Fujiwara, K. High Temperature Gas Reaction Specimen Chamber for an Electron Microscope. *Jpn. J. Appl. Phys.* **1968**, *7*, 946−952.
(78) Parsons, D. F. Structure of Wet Specimens in Electron Microscopy. *Science* **1974**, *186*, 407−414.
(79) Boyes, E. D.; Gai, P. L. Environmental High Resolution Electron Microscopy and Applications to Chemical Science. *Ultramicroscopy* **1997**, *67*, 219−232.
(80) Wang, C.; Marković, N.; Stamenković, V. Advanced Platinum Alloy Electrocatalysts for the Oxygen Reduction Reaction. *ACS Catal.* **2012**, *2*, 891−898.
(81) Zhao, Q.; Yan, Z.; Chen, C.; Chen, J. Spinels: Controlled Preparation, Oxygen Reduction/Evolution Reaction Application, and Beyond. *Chem. Rev.* **2017**, *117*, 10121−10211.
(82) Xiao, W.; Lei, W.; Gong, M.; Xin, H.; Wang, D. Recent Advances of Structurally Ordered Intermetallic Nanoparticles for Electrocatalysis. *ACS Catal.* **2018**, *8*, 3237−3256.
(83) Frenkel, A.; Rodriguez, J.; Chen, J. Synchrotron Techniques for In Situ Catalytic Studies: Capabilities, Challenges, and Opportunities. *ACS Catal.* **2012**, *2*, 2269−2280.
(84) Bordiga, S.; Groppo, E.; Agostini, G.; van Bokhoven, J. A.; Lamberti, C. Reactivity of Surface Species in Heterogeneous Catalysts Probed by *In Situ* X-ray Absorption Techniques. *Chem. Rev.* **2013**, *113*, 1736−1850.
(85) Li, X.; Wang, S.; Li, L.; Sun, Y.; Xie, Y. Progress and Perspective for In Situ Studies of CO_2 Reduction. *J. Am. Chem. Soc.* **2020**, *142* (21), 9567−9581.
(86) Yang, Y.; Xiong, Y.; Holtz, M. E.; Feng, X.; Zeng, R.; Chen, G.; DiSalvo, F. J.; Muller, D. A.; Abruña, H. D. Octahedral Spinel Electrocatalysts for Alkaline Fuel Cells. *Proc. Natl. Acad. Sci. U. S. A.* **2019**, *116*, 24425−24432.
(87) Yang, Y.; Zeng, R.; Xiong, Y.; DiSalvo, F. J.; Abruña, H. D. Cobalt-Based Nitride-Core Oxide-Shell Oxygen Reduction Electrocatalysts. *J. Am. Chem. Soc.* **2019**, *141*, 19241−19245.
(88) Wang, H.; Abruña, H. D. Single-Phase $Ru_{1-x-y}Mn_xCo_yO_2$ Nanoparticles as Highly Effective Oxygen Reduction Electrocatalysts in Alkaline Media with Enhanced Stability and Fuel-Tolerance. *Appl. Catal., B* **2020**, *277*, 119149.
(89) Wang, H.; Yang, Y.; DiSalvo, F. J.; Abruña, H. D. Multifunctional Electrocatalysts: Ru-M (M = Co, Ni, Fe) for Alkaline Fuel Cells and Electrolyzers. *ACS Catal.* **2020**, *10*, 4608−4616.
(90) Yang, Y.; Peng, H.; Xiong, Y.; Li, Q.; Lu, J.; Xiao, L.; DiSalvo, F. J.; Zhuang, L.; Abruña, H. D. High-Loading Composition-Tolerant Co-Mn Spinel Oxides with Performance beyond 1 W/cm^2 in Alkaline Polymer Electrolyte Fuel Cells. *ACS Energy Lett.* **2019**, *4*, 1251−1257.
(91) Yang, Y.; Zeng, R.; Xiong, Y.; DiSalvo, F. J.; Abruña, H. D. Rock-Salt-Type $MnCo_2O_3$/C as Efficient Oxygen Reduction Electrocatalysts for Alkaline Fuel Cells. *Chem. Mater.* **2019**, *31*, 9331−9337.
(92) Norskov, J.; Rossmeisl, J.; Logadottir, A.; Lindqvist, L.; Kitchin, J. R.; Bligaard, T.; Jonsson, H. Origin of the Overpotential for Oxygen Reduction at a Fuel Cell Cathode. *J. Phys. Chem. B* **2004**, *108*, 17886−17892.
(93) Greeley, J.; Stephens, I. E. L.; Bondarenko, A. S.; Johansson, T. P.; Hansen, H. A.; Jaramillo, T. F.; Rossmeisl, J.; Chorkendorff, I.; Nørskov, J. K. Norskov, J. Alloys of Platinum and Early Transition Metals as Oxygen Reduction Electrocatalysts. *Nat. Chem.* **2009**, *1*, 552−556.
(94) Wang, D.; Xin, H. L.; Hovden, R.; Wang, H.; Yu, Y.; Muller, D. A.; DiSalvo, F. J.; Abruña, H. D. Structurally Ordered Intermetallic Platinum-Cobalt Core-Shell Nanoparticles with Enhanced Activity and Stability as Oxygen Reduction Electrocatalysts. *Nat. Mater.* **2013**, *12*, 81−87.
(95) Muller, D. A. Structure and Bonding at the Atomic Scale by Scanning Transmission Electron Microscopy. *Nat. Mater.* **2009**, *8*, 263−270.
(96) Xiong, Y.; Yang, Y.; DiSalvo, F. J.; Abruña, H. D. Synergistic Bimetallic Metallic Organic Framework-Derived Pt-Co Oxygen Reduction Electrocatalysts. *ACS Nano* **2020**, *14*, 13069−13080.
(97) Xiong, Y.; Xiao, L.; Yang, Y.; DiSalvo, F. J.; Abruña, H. D. High-Loading Intermetallic Pt_3Co/C Core-Shell Nanoparticles as Enhanced Activity Electrocatalysts toward the Oxygen Reduction Reaction (ORR). *Chem. Mater.* **2018**, *30*, 1532−1539.

https://dx.doi.org/10.1021/acscatal.0c04789
ACS Catal. 2021, 11, 1136−1178

(98) Cui, C.; Gan, L.; Heggen, M.; Rudi, S.; Strasser, P. Compositional Segregation in Shaped Pt Alloy Nanoparticles and Their Structural Behaviour During Electrocatalysis. *Nat. Mater.* **2013**, *12*, 765−771.
(99) Zhang, J.; Yang, H.; Fang, J.; Zou, S. Synthesis and Oxygen Reduction Activity of Shape-Controlled Pt_3Ni Nanopolyhedra. *Nano Lett.* **2010**, *10*, 638−644.
(100) Wu, Y.; Cai, S.; Wang, D.; He, W.; Li, Y. Syntheses of Water-Soluble Octahedral, Truncated Octahedral, and Cubic Pt-Ni Nanocrystals and Their Structure-Activity Study in Model Hydrogenation Reactions. *J. Am. Chem. Soc.* **2012**, *134*, 8975−8981.
(101) Becknell, N.; Son, Y.; Kim, D.; Li, D.; Yu, Y.; Niu, Z.; Lei, T.; Sneed, B. T.; More, K. L.; Marković, N. M.; Stamenković, V. R.; Yang, P. Control of Architecture in Rhombic Dodecahedral Pt-Ni Nanoframe Electrocatalysts. *J. Am. Chem. Soc.* **2017**, *139*, 11678−11681.
(102) Chen, C.; Kang, Y.; Huo, Z.; Zhu, Z.; Huang, W.; Xin, H. L.; Snyder, J. D.; Li, D.; Herron, J. A.; Mavrikakis, M.; Chi, M.; More, K. L.; Li, Y.; Markovic, N. M.; Somorjai, G. A.; Yang, P.; Stamenkovic, V. R. Stamenković, V. R. Highly Crystalline Multimetallic Nanoframes with Three-Dimensional Electrocatalytic Surfaces. *Science* **2014**, *343*, 1339−1343.
(103) Niu, Z.; Becknell, N.; Yu, Y.; Kim, D.; Chen, C.; Kornienko, N.; Somorjai, G. A.; Yang, P. Anisotropic Phase Segregation and Migration of Pt in Nanocrystals en Route to Nanoframe Catalysts. *Nat. Mater.* **2016**, *15*, 1188−1194.
(104) Choi, S.; Xie, S.; Shao, M.; Odell, J. H.; Lu, N.; Peng, H.-C.; Protsailo, L.; Guerrero, S.; Park, J.; Xia, X.; Wang, J.; Kim, M. J.; Xia, Y. Synthesis and Characterization of 9 nm Pt-Ni Octahedra with a Record High Activity of 3.3 A/mg_{Pt} for the Oxygen Reduction Reaction. *Nano Lett.* **2013**, *13*, 3420−3425.
(105) Chang, Q.; Xu, Y.; Duan, Z.; Xiao, F.; Fu, F.; Hong, Y.; Kim, J.; Choi, S.; Su, D.; Shao, M. Structural Evolution of Sub-10 Nm Octahedral Platinum-Nickel Bimetallic Nanocrystals. *Nano Lett.* **2017**, *17*, 3926−3931.
(106) Chattot, R.; Asset, T.; Drnec, J.; Bordet, P.; Nelayah, J.; Dubau, L.; Maillard, F. Atomic-Scale Snapshots of the Formation and Growth of Hollow PtNi/C Nanocatalysts. *Nano Lett.* **2017**, *17*, 2447−2453.
(107) Chattot, R.; Le Bacq, O.; Beermann, V.; Kuhl, S.; Herranz, J.; Henning, S.; Kuhn, L.; Asset, T.; Guetaz, L.; Renou, G.; Drnec, J.; Bordet, P.; Pasturel, A.; Eychmuller, A.; Schmidt, T.; Strasser, P.; Dubau, L.; Maillard, F. Surface distortion as a unifying concept and descriptor in oxygen reduction reaction electrocatalysis. *Nat. Mater.* **2018**, *17*, 827−833.
(108) Kongkanand, A.; Mathias, M. F. The Priority and Challenge of High-Power Performance of Low-Platinum Proton-Exchange Membrane Fuel Cells. *J. Phys. Chem. Lett.* **2016**, *7*, 1127−1137.
(109) Kongkanand, A.; Muller, D. A.; et al. Achieving High-Power PEM Fuel Cell Performance with an Ultralow-Pt-Content Core-Shell Catalyst. *ACS Catal.* **2016**, *6*, 1578−1583.
(110) Wang, D.; Yu, Y.; Xin, H. L.; Hovden, R.; Ercius, P.; Mundy, J. A.; Chen, H.; Richard, J. H.; Muller, D. A.; DiSalvo, F. J.; Abruña, H. D. Tuning Oxygen Reduction Reaction Activity via Controllable Dealloying: a Model Study of Ordered Cu_3Pt/C Intermetallic Nanocatalysts. *Nano Lett.* **2012**, *12*, 5230−5238.
(111) Lu, X.; Ahmadi, M.; DiSalvo, F. J.; Abruña, H. D. Enhancing the Electrocatalytic Activity of Pd/M (M = Ni, Mn) Nanoparticles for the Oxygen Reduction Reaction in Alkaline Media through Electrochemical Dealloying. *ACS Catal.* **2020**, *10*, 5891−5898.
(112) Gan, L.; Heggen, M.; O'Malley, R.; Theobald, B.; Strasser, P. Understanding and Controlling Nanoporosity Formation for Improving the Stability of Bimetallic Fuel Cell Catalysts. *Nano Lett.* **2013**, *13*, 1131−1138.
(113) Meier, J. C.; Galeano, C.; Katsounaros, I.; Witte, J.; Bongard, H. J.; Topalov, A. A.; Baldizzone, C.; Mezzavilla, S.; Schuth, F.; Mayrhofer, K. J. Design Criteria for Stable Pt/C Fuel Cell Catalysts. *Beilstein J. Nanotechnol.* **2014**, *5*, 44−67.
(114) Yarlagadda, V.; Carpenter, M. K.; Moylan, T. E.; Kukreja, R. S.; Koestner, R.; Gu, W.; Thompson, L.; Kongkanand, A. Boosting Fuel Cell Performance with Accessible Carbon Mesopores. *ACS Energy Lett.* **2018**, *3*, 618−621.
(115) Yu, Y.; Li, H.; Wang, H.; Yuan, X.-Z.; Wang, G.; Pan, M. A Review on Performance Degradation of Proton Exchange Membrane Fuel Cells during Startup and Shutdown Processes: Causes, Consequences, and Mitigation Strategies. *J. Power Sources* **2012**, *205*, 10−23.
(116) Padgett, E.; Yarlagadda, V.; Holtz, M. E.; Ko, M.; Levin, B. D. A.; Kukreja, R. S.; Ziegelbauer, J. M.; Andrews, R. N.; Ilavsky, J.; Kongkanand, A.; Muller, D. A. Mitigation of PEM Fuel Cell Catalyst Degradation with Porous Carbon Supports. *J. Electrochem. Soc.* **2019**, *166*, F198−F207.
(117) Xin, H. L.; Mundy, J. A.; Liu, Z.; Cabezas, R.; Hovden, R.; Kourkoutis, L. F.; Zhang, J.; Subramanian, N. P.; Makharia, R.; Wagner, F. T.; Muller, D. A. Atomic-Resolution Spectroscopic Imaging of Ensembles of Nanocatalyst Particles across the Life of a Fuel Cell. *Nano Lett.* **2012**, *12*, 490−497.
(118) Chung, H. T.; Cullen, D. A.; Higgins, D.; Sneed, B. T.; Holby, E. F.; More, K. L.; Zelenay, P. Direct Atomic-Level Insight into the Active Sites of a High-Performance PGM-free ORR Catalyst. *Science* **2017**, *357*, 479−484.
(119) Ren, H.; Wang, Y.; Yang, Y.; Tang, X.; Peng, Y.; Peng, H.; Xiao, L.; Lu, J.; Abruña, H. D.; Zhuang, L. Fe/N/C Nanotubes with Atomic Fe Sites: A Highly Active Cathode Catalyst for Alkaline Polymer Electrolyte Fuel Cells. *ACS Catal.* **2017**, *7*, 6485−6492.
(120) Xiong, Y.; Yang, Y.; DiSalvo, F. J.; Abruña, H. D. Metal-Organic-Framework-Derived Co-Fe Bimetallic Oxygen Reduction Electrocatalysts For Alkaline Fuel Cells. *J. Am. Chem. Soc.* **2019**, *141*, 10744−10750.
(121) Chong, L.; Wen, J.; Kubal, J.; Sen, F. G.; Zou, J.; Greeley, J.; Chan, M.; Barkholtz, H.; Ding, W.; Liu, D.-J. Ultralow-Loading Platinum-Cobalt Fuel Cell Catalysts Derived from Imidazolate Frameworks. *Science* **2018**, *362*, 1276−1281.
(122) Lu, B.; Liu, Q.; Chen, S. Electrocatalysis of Single-Atom Sites: Impacts of Atomic Coordination. *ACS Catal.* **2020**, *10*, 7584−7618.
(123) Padgett, E.; Andrejevic, N.; Liu, Z.; Kongkanand, A.; Gu, W.; Moriyama, K.; Jiang, Y.; Kumaraguru, S.; Moylan, T. E.; Kukreja, R.; Muller, D. A. Editors' Choice-Connecting Fuel Cell Catalyst Nanostructure and Accessibility Using Quantitative Cryo-STEM Tomography. *J. Electrochem. Soc.* **2018**, *165*, F173−F180.
(124) Mayrhofer, K. J. J.; Ashton, S. J.; Meier, J. C.; Wiberg, G. K. H.; Kraus, F.; Hanzlik, M.; Arenz, M. Fuel Cell Catalyst Degradation on the Nanoscale. *Electrochem. Commun.* **2008**, *10*, 1144−1147.
(125) Mayrhofer, K. J. J.; Ashton, S. J.; Meier, J. C.; Wiberg, G. K. H.; Hanzlik, M.; Arenz, M. Non-destructive Transmission Electron Microscopy Study of Catalyst Degradation under Electrochemical Treatment. *J. Power Sources* **2008**, *185*, 734−739.
(126) Baldizzone, C.; Mezzavilla, S.; Carvalho, H. W. P.; Meier, J. C.; Schuppert, A. K.; Heggen, M.; Galeano, C.; Grunwaldt, J.-D.; Schüth, F.; Mayrhofer, K. J. J. Confined-Space Alloying of Nanoparticles for the Synthesis of Efficient PtNi Fuel-Cell Catalysts. *Angew. Chem., Int. Ed.* **2014**, *53*, 14250−14254.
(127) Claudel, F.; Dubau, L.; Berthomé, G.; Sola-Hernandez, L.; Beauger, C.; Piccolo, L.; Maillard, F. Degradation Mechanisms of Oxygen Evolution Reaction Electrocatalysts: A Combined Identical-Location Transmission Electron Microscopy and X-Ray Photoelectron Spectroscopy Study. *ACS Catal.* **2019**, *9*, 4688−4698.
(128) Aiyappa, H.; Wilde, P.; Quast, T.; Masa, J.; Andronescu, C.; Chen, Y.; Muhler, M.; Fischer, R.; Schuhmann, W. Oxygen Evolution Electrocatalysis of a Single MOF-Derived Composite Nanoparticle on the Tip of a Nanoelectrode. *Angew. Chem., Int. Ed.* **2019**, *58*, 8927−8931.
(129) Arenz, M.; Zana, A. Fuel Cell Catalyst Degradation: Identical Location Electron Microscopy and Related Methods. *Nano Energy* **2016**, *29*, 299−313.
(130) Rasouli, S.; Myers, D.; Kariuki, N.; Higashida, K.; Nakashima, N.; Ferreira, P. Electrochemical Degradation of Pt-Ni Nanocatalysts:

An Identical Location Aberration-Corrected Scanning Transmission Electron Microscopy Study. *Nano Lett.* **2019**, *19*, 46−53.
(131) Arán-Ais, R. M.; Yu, Y.; Hovden, R.; Solla-Gullón, J.; Herrero, E.; Feliu, J. M.; Abruña, H. D. IL-TEM Imaging of Site-Selective Pt Nanocatalysts: Electrochemical Activation and Surface Disordering. *J. Am. Chem. Soc.* **2015**, *137*, 14992−14998.
(132) Yu, Y.; Xin, H. L.; Hovden, R.; Wang, D.; Rus, E. D.; Mundy, J. A.; Muller, D. A.; Abruña, H. D. Three-Dimensional Tracking and Visualization of Hundreds of Pt-Co Fuel Cell Nanocatalysts During Electrochemical Aging. *Nano Lett.* **2012**, *12*, 4417−4423.
(133) Perez-Alonso, F.; Elkjær, C.; Shim, S.; Abrams, B.; Stephens, I.; Chorkendorff, I. Identical Locations Transmission Electron Microscopy Study of Pt/C Electrocatalyst Degradation during Oxygen Reduction Reaction. *J. Power Sources* **2011**, *196*, 6085−6091.
(134) Dubau, L.; Castanheira, L.; Berthomé, G.; Maillard, F. An Identical-Location Transmission Electron Microscopy Study on the Degradation of Pt/C Nanoparticles under Oxidizing, Reducing and Neutral Atmosphere. *Electrochim. Acta* **2013**, *110*, 273−281.
(135) Lafforgue, C.; Chatenet, M.; Dubau, L.; Dekel, D. Accelerated Stress-test of Pt/C Nanoparticles in Interface with an Anion-Exchange Membrane - An Identical Location Transmission Electron Microscopy Study. *ACS Catal.* **2018**, *8*, 1278−1286.
(136) Williamson, M.; Tromp, R.; Vereecken, P.; Hull, R.; Ross, F. Dynamic Microscopy of Nanoscale Cluster Growth at the Solid-Liquid Interface. *Nat. Mater.* **2003**, *2*, 532−536.
(137) de Jonge, N.; Ross, F. M. Electron Microscopy of Specimens in Liquid. *Nat. Nanotechnol.* **2011**, *6*, 695−704.
(138) Ross, F. M. Opportunities and Challenges in Liquid Cell Electron Microscopy. *Science* **2015**, *350*, No. aaa9886.
(139) Ross, F. M. *Liquid Cell Electron Microscopy*; Cambridge University Press: New York, 2017; p 210.
(140) Hodnik, N.; Dehm, G.; Mayrhofer, K. J. J. Importance and Challenges of Electrochemical in Situ Liquid Cell Electron Microscopy for Energy Conversion Research. *Acc. Chem. Res.* **2016**, *49*, 2015−2022.
(141) Zeng, Z.; Zheng, W.; Zheng, H. Visualization of Colloidal Nanocrystal Formation and Electrode-Electrolyte Interfaces in Liquids Using TEM. *Acc. Chem. Res.* **2017**, *50*, 1808−1817.
(142) Schneider, N. M.; Norton, M. M.; Mendel, B. J.; Grogan, J. M.; Ross, F. M.; Bau, H. H. Electron-Water Interactions and Implications for Liquid Cell Electron Microscopy. *J. Phys. Chem. C* **2014**, *118*, 22373−22382.
(143) de Jonge, N.; Houben, L.; Dunin-Borkowski, R. E.; Ross, F. M. Resolution and Aberration Correction in Liquid Cell Transmission Electron Microscopy. *Nat. Rev. Mater.* **2019**, *4*, 61−78.
(144) Holtz, M. E.; Yu, Y.; Gunceler, D.; Gao, J.; Sundararaman, R.; Schwarz, K. A.; Arias, T. A.; Abruña, H. D.; Muller, D. A. Nanoscale Imaging of Lithium Ion Distribution during In Situ Operation of Battery Electrode and Electrolyte. *Nano Lett.* **2014**, *14*, 1453−1459.
(145) Beermann, V.; Holtz, M. E.; Padgett, E.; de Araujo, J. F.; Muller, D. A.; Strasser, P. Real-Time Imaging of Activation and Degradation of Carbon Supported Octahedral Pt-Ni Alloy Fuel Cell Catalysts at the Nanoscale Using In Situ Electrochemical Liquid Cell STEM. *Energy Environ. Sci.* **2019**, *12*, 2476−2485.
(146) Holtz, M. E.; Yu, Y.; Gao, J.; Abruña, H. D.; Muller, D. A. *In Situ* Electron Energy-Loss Spectroscopy in Liquids. *Microsc. Microanal.* **2013**, *19*, 1027−1035.
(147) Yu, Y.; Holtz, M. E.; Xin, H. L.; Wang, D.; Abruña, H. D.; Muller, D. A. Understanding Pt-Co Catalyst Degradation Mechanism: from Ex-situ to In-situ. *Microsc. Microanal.* **2013**, *19*, 1666−1667.
(148) Sacci, R. L.; Black, J. M.; Balke, N.; Dudney, N. J.; More, K. L.; Unocic, R. R. Nanoscale Imaging of Fundamental Li Battery Chemistry: Solid-Electrolyte Interphase Formation and Preferential Growth of Lithium Metal Nanoclusters. *Nano Lett.* **2015**, *15*, 2011−2018.
(149) Zeng, Z.; Zhang, X.; Bustillo, K.; Niu, K.; Gammer, C.; Xu, J.; Zheng, H. In Situ Study of Lithiation and Delithiation of MoS_2 Nanosheets Using Electrochemical Liquid Cell Transmission Electron Microscopy. *Nano Lett.* **2015**, *15*, 5214−5220.
(150) Yang, C.; Han, J.; Liu, P.; Hou, C.; Huang, G.; Fujita, T.; Hirata, A.; Chen, M. Direct Observations of the Formation and Redox-Mediator-Assisted Decomposition of Li_2O_2 in a Liquid-Cell Li-O_2 Microbattery by Scanning Transmission Electron Microscopy. *Adv. Mater.* **2017**, *29*, 1702752.
(151) Lutz, L.; Dachraoui, W.; Demortiere, A.; Johnson, L. R.; Bruce, P. G.; Grimaud, A.; Tarascon, J.-M. Operando Monitoring of the Solution-Mediated Discharge and Charge Processes in a Na-O_2 Battery Using Liquid-Electrochemical Transmission Electron Microscopy. *Nano Lett.* **2018**, *18*, 1280−1289.
(152) Huang, J. Y.; Zhong, L.; Wang, C. M.; Sullivan, J. P.; Xu, W.; Zhang, L. Q.; Mao, S. X.; Hudak, N. S.; Liu, X. H.; Subramanian, A.; Fan, H.; Qi, L.; Kushima, A.; Li, J. In Situ Observation of the Electrochemical Lithiation of a Single SnO_2 Nanowire Electrode. *Science* **2010**, *330*, 1515−1520.
(153) Aran-Ais, R. M.; Rizo, R.; Grosse, P.; Algara-Siller, G.; Dembele, K.; Plodinec, M.; Lunkenbein, T.; Chee, S. W.; Cuenya, B. R. Imaging Electrochemically Synthesized Cu_2O Cubes and Their Morphological Evolution under Conditions Relevant To CO_2 Electroreduction. *Nat. Commun.* **2020**, *11*, 3489.
(154) Li, Y.; Kim, D.; Louisia, S.; Xie, C.; Kong, Q.; Yu, S.; Lin, T.; Aloni, S.; Fakra, S.; Yang, P. Electrochemically Scrambled Nanocrystals are Catalytically Active for CO_2-To-Multicarbons. *Proc. Natl. Acad. Sci. U. S. A.* **2020**, *117*, 9194−9201.
(155) Aliyah, K.; Lyu, J.; Goldmann, C.; Bizien, T.; Hamon, C.; Alloyeau, D.; Constantin, D. Real-Time In Situ Observations Reveal a Double Role for Ascorbic Acid in the Anisotropic Growth of Silver on Gold. *J. Phys. Chem. Lett.* **2020**, *11*, 2830−2837.
(156) Liao, H.-G.; Zherebetskyy, D.; Xin, H.; Czarnik, C.; Ercius, P.; Elmlund, H.; Pan, M.; Wang, L.-W.; Zheng, H. Facet Development during Platinum Nanocube Growth. *Science* **2014**, *345*, 916−919.
(157) Liao, H.-G.; Zheng, H. Liquid Cell Transmission Electron Microscopy Study of Platinum Iron Nanocrystal Growth and Shape Evolution. *J. Am. Chem. Soc.* **2013**, *135*, 5038−5043.
(158) Sutter, E. A.; Sutter, P. W. Determination of Redox Reaction Rates and Orders by In Situ Liquid Cell Electron Microscopy of Pd and Au Solution Growth. *J. Am. Chem. Soc.* **2014**, *136*, 16865−16870.
(159) Tan, S.; Chee, S.; Lin, G.; Bosman, M.; Lin, M.; Mirsaidov, U.; Nijhuis, C. Real-Time Imaging of the Formation of Au-Ag Core-Shell Nanoparticles. *J. Am. Chem. Soc.* **2016**, *138*, 5190−5193.
(160) Hauwiller, M. R.; Ondry, J. C.; Chan, C. M.; Khandekar, P.; Yu, J.; Alivisatos, A. P. Gold Nanocrystal Etching as a Means of Probing the Dynamic Chemical Environment in Graphene Liquid Cell Electron Microscopy. *J. Am. Chem. Soc.* **2019**, *141*, 4428−4437.
(161) Shan, H.; Gao, W.; Xiong, Y.; Shi, F.; Yan, Y.; Ma, Y.; Shang, W.; Tao, P.; Song, C.; Deng, T.; et al. Nanoscale Kinetics of Asymmetrical Corrosion in Core-Shell Nanoparticles. *Nat. Commun.* **2018**, *9*, 1011.
(162) Hermannsdorfer, J.; de Jonge, N.; Verch, A. Electron Beam Induced Chemistry of Gold Nanoparticles in Saline Solution. *Chem. Commun.* **2015**, *51*, 16393−16396.
(163) Proetto, M. T.; Rush, A. M.; Chien, M.-P.; Abellan Baeza, P.; Patterson, J. P.; Thompson, M. P.; Olson, N. H.; Moore, C. E.; Rheingold, A. L.; Andolina, C.; Millstone, J.; Howell, S. B.; Browning, N. D.; Evans, J. E.; Gianneschi, N. C. Dynamics of Soft Nanomaterials Captured by Transmission Electron Microscopy in Liquid Water. *J. Am. Chem. Soc.* **2014**, *136*, 1162−1165.
(164) Patterson, J. P.; Abellan, P.; Denny, M. S.; Park, C.; Browning, N. D.; Cohen, S. M.; Evans, J. E.; Gianneschi, N. C. Observing the Growth of Metal-Organic Frameworks by in Situ Liquid Cell Transmission Electron Microscopy. *J. Am. Chem. Soc.* **2015**, *137*, 7322−7328.
(165) de Jonge, N.; Peckys, D. B.; Kremers, G. J.; Piston, D. W. Electron Microscopy of Whole Cells in Liquid with Nanometer Resolution. *Proc. Natl. Acad. Sci. U. S. A.* **2009**, *106*, 2159−2164.
(166) Le Ferrand, H.; Duchamp, M.; Gabryelczyk, B.; Cai, H.; Miserez, A. Time-Resolved Observations of Liquid-Liquid Phase Separation at the Nanoscale Using in Situ Liquid Transmission Electron Microscopy. *J. Am. Chem. Soc.* **2019**, *141*, 7202−7210.

https://dx.doi.org/10.1021/acscatal.0c04789
ACS Catal. 2021, 11, 1136−1178

(167) Henderson, R. The Potential and Limitations of Neutrons, Electrons and X-rays for Atomic Resolution Microscopy of Unstained Biological Moleclues. *Q. Rev. Biophys.* **1995**, *28*, 171−193.
(168) Schilling, S.; Janssen, A.; Zaluzec, N.; Burke, M. G. Practical Aspects of Electrochemical Corrosion Measurements During In Situ Analytical Transmission Electron Microscopy (TEM) of Austenitic Stainless Steel in Aqueous Media. *Microsc. Microanal.* **2017**, *23*, 741−750.
(169) Unocic, R.; Sacci, R. L.; Brown, G. M.; Veith, G. M.; Dudney, N. J.; More, K. M.; Walden, F. S., II; Gardiner, D. S.; Damiano, J.; Nackashi, D. P. Quantitative Electrochemical Measurements Using *In Situ* ec-S/TEM Devices. *Microsc. Microanal.* **2014**, *20*, 452−461.
(170) Stricker, E. A.; Ke, X.; Wainright, J. S.; Unocic, R.; Savinell, R. F. Current Density Distribution in Electrochemical Cells with Small Cell Heights and Coplanar Thin Electrodes as Used in EC-S/TEM Cell Geometries. *J. Electrochem. Soc.* **2019**, *166*, H126−H134.
(171) Zhu, G.-Z.; Prabhudev, S.; Yang, J.; Gabardo, C. M.; Botton, G. A.; Soleymani, L. In Situ Liquid Cell TEM Study of Morphological Evolution and Degradation of Pt-Fe Nanocatalysts During Potential Cycling. *J. Phys. Chem. C* **2014**, *118*, 22111−22119.
(172) Tian, N.; Zhou, Z.-Y.; Sun, S.-G.; Ding, Y.; Wang, Z. L. Synthesis of Tetrahexahedral Platinum Nanocrystals with High-Index Facets and High Electro-Oxidation Activity. *Science* **2007**, *316*, 732−735.
(173) Schouten, K. J. P.; Perez Gallent, E.; Koper, M. T. M. Structure Sensitivity of the Electrochemical Reduction of Carbon Monoxide on Copper Single Crystals. *ACS Catal.* **2013**, *3*, 1292−1295.
(174) Roberts, F. S.; Kuhl, K. P.; Nilsson, A. High Selectivity for Ethylene from Carbon Dioxide Reduction over Copper Nanocube Electrocatalysts. *Angew. Chem., Int. Ed.* **2015**, *54*, 5179−5182.
(175) Kim, D.; Kley, C. S.; Li, Y.; Yang, P. Copper Nanoparticle Ensembles for Selective Electroreduction of CO_2 to C_2-C_3 Products. *Proc. Natl. Acad. Sci. U. S. A.* **2017**, *114*, 10560−10565.
(176) Grosse, P.; Gao, D.; Scholten, F.; Sinev, I.; Mistry, H.; Roldan Cuenya, B. Dynamic Changes in the Structure, Chemical State and Catalytic Selectivity of Cu Nanocubes during CO_2 Electroreduction: Size and Support Effects. *Angew. Chem., Int. Ed.* **2018**, *57*, 6192−6197.
(177) Zaluzec, N.; Burke, M. G.; Haigh, S. J.; Kulzick, M. X-ray Energy-Dispersive Spectrometry During In Situ Liquid Cell Studies Using an Analytical Electron Microscope. *Microsc. Microanal.* **2014**, *20*, 323−329.
(178) Lewis, E.; Haigh, S. J.; Slater, T. J. A.; He, Z.; Kulzick, M. A.; Burke, M. G.; Zaluzec, N. J. Real-Time Imaging and Local Elemental Analysis of Nanostructures in Liquids. *Chem. Commun.* **2014**, *50*, 10019−10022.
(179) Kim, B. H.; Heo, J.; Kim, S.; Reboul, C. F.; Chun, H.; Kang, D.; Bae, H.; Hyun, H.; Lim, J.; Lee, H.; Han, B.; Hyeon, T.; Alivisatos, P. A.; Ercius, P.; Elmlund, H.; Park, J. Critical Differences in 3D Atomic Structure of Individual Ligand-Protected Nanocrystals in Solution. *Science* **2020**, *368*, 60−67.
(180) Ross, F. M. Temperature Effects in Liquid-Cell Transmission Electron Microscopy. *Microsc. Microanal.* **2020**, *26*, 2566−2567.
(181) Liu, J.; Wei, B.; Sloppy, J.; Ouyang, L.; Ni, C.; Martin, D. Direct Imaging Of The Electrochemical Deposition Of Poly(3,4-Ethylenedioxythiophene) By Transmission Electron Microscopy. *ACS Macro Lett.* **2015**, *4*, 897−900.
(182) Jiang, Y.; Chen, Z.; Han, Y.; Deb, P.; Gao, H.; Xie, S.; Purohit, P.; Tate, M. W.; Park, J.; Gruner, S. M.; Elser, V.; Muller, D. A. Electron Ptychography of 2D Materials to Deep Sub-Ångström Resolution. *Nature* **2018**, *559*, 343−349.
(183) Tate, M. W.; Purohit, P.; Chamberlain, D.; Nguyen, K. X.; Hovden, R.; Chang, C. S.; Deb, P.; Turgut, E.; Heron, J. T.; Schlom, D. G.; Ralph, D.; Fuchs, G. D.; Shanks, K. S.; Philipp, H. T.; Muller, D. A.; Gruner, S. M. High Dynamic Range Pixel Array Detector for Scanning Transmission Electron Microscopy. *Microsc. Microanal.* **2016**, *22*, 237−249.
(184) Creemer, J. F.; Helveg, S.; Hoveling, G. H.; Ullmann, S.; Molenbroek, A. M.; Sarro, P. M.; Zandbergen, H. W. Atomic-Scale Electron Microscopy at Ambient Pressure. *Ultramicroscopy* **2008**, *108*, 993−998.
(185) de Jonge, N.; Bigelow, W. C.; Veith, G. M. Atmospheric Pressure Scanning Transmission Electron Microscopy. *Nano Lett.* **2010**, *10*, 1028−1031.
(186) Zugic, B.; Wang, L.; Heine, C.; Zakharov, D. N.; Lechner, B. A. J.; Stach, E. A.; Biener, J.; Salmeron, M.; Madix, R. J.; Friend, C. M. Dynamic Restructuring Drives Catalytic Activity on Nanoporous Gold-Silver Alloy Catalysts. *Nat. Mater.* **2017**, *16*, 558−564.
(187) Kodambaka, S.; Tersoff, J.; Reuter, M. C.; Ross, F. M. Germanium Nanowire Growth Below the Eutectic Temperature. *Science* **2007**, *316*, 729−732.
(188) van der Vliet, D.; Wang, C.; Tripkovic, D.; Strmcnik, D.; Zhang, X.; Debe, M.; Atanasoski, R.; Marković, N.; Stamenković, V. Mesostructured Thin Films as Electrocatalysts with Tunable Composition and Surface Morphology. *Nat. Mater.* **2012**, *11*, 1051−1058.
(189) Beermann, V.; Gocyla, M.; Kuhl, S.; Padgett, E.; Schmies, H.; Goerlin, M.; Erini, N.; Shviro, M.; Heggen, M.; Dunin-Borkowski, R. E.; Muller, D. A.; Strasser, P. Tuning the Electrocatalytic Oxygen Reduction Reaction Activity and Stability of Shape-Controlled Pt-Ni Nanoparticles by Thermal Annealing-Elucidating the Surface Atomic Structural and Compositional Changes. *J. Am. Chem. Soc.* **2017**, *139*, 16536−16547.
(190) Gocyla, M.; Kuehl, S.; Shviro, M.; Heyen, H.; Selve, S.; Dunin-Borkowski, R. E.; Heggen, M.; Strasser, P. Shape Stability of Octahedral PtNi Nanocatalysts for Electrochemical Oxygen Reduction Reaction Studied by in Situ Transmission Electron Microscopy. *ACS Nano* **2018**, *12*, 5306−5311.
(191) Onn, T.; Zhang, S.; Arroyo-Ramirez, L.; Chung, Y.; Graham, G.; Pan, X.; Gorte, R. Improved Thermal Stability And Methane-Oxidation Activity Of Pd/Al_2O_3 Catalysts by Atomic Layer Deposition Of ZrO_2. *ACS Catal.* **2015**, *5*, 5696−5701.
(192) Xin, H.; Alayoglu, S.; Tao, R.; Genc, A.; Wang, C.; Kovarik, L.; Stach, E.; Wang, L.; Salmeron, M.; Somorjai, G.; Zheng, H. Revealing the Atomic Restructuring of Pt-Co Nanoparticles. *Nano Lett.* **2014**, *14*, 3203−3207.
(193) Chi, M.; Wang, C.; Lei, Y.; Wang, G.; Li, D.; More, K.; Lupini, A.; Allard, L.; Marković, N.; Stamenković, V. Surface Faceting and Elemental Diffusion Behaviour at Atomic Scale for Alloy Nanoparticles during In Situ Annealing. *Nat. Commun.* **2015**, *6*, 8925.
(194) Avanesian, T.; Dai, S.; Kale, M.; Graham, G.; Pan, X.; Christopher, P. Quantitative and Atomic-Scale View of CO-induced Pt Nanoparticle Surface Reconstruction at Saturation Coverage via DFT Calculations Coupled with In Situ TEM and IR. *J. Am. Chem. Soc.* **2017**, *139*, 4551−4558.
(195) Dubau, L.; Nelayah, J.; Moldovan, S.; Ersen, O.; Bordet, P.; Drnec, J.; Asset, T.; Chattot, R.; Maillard, F. Defects Do Catalysis: CO Monolayer Oxidation and Oxygen Reduction Reaction on Hollow PtNi/C Nanoparticles. *ACS Catal.* **2016**, *6*, 4673−4684.
(196) Moliner, M.; Gabay, J.; Kliewer, C.; Carr, R.; Guzman, J.; Casty, G.; Serna, P.; Corma, A. Reversible Transformation of Pt Nanoparticles into Single Atoms inside High-Silica Chabazite Zeolite. *J. Am. Chem. Soc.* **2016**, *138*, 15743−15750.
(197) Dai, S.; You, Y.; Zhang, S.; Cai, W.; Xu, M.; Xie, L.; Wu, R.; Graham, G.; Pan, X. In Situ Atomic-Scale Observation of Oxygen-Driven Core-shell Formation in Pt_3Co Nanoparticles. *Nat. Commun.* **2017**, *8*, 204.
(198) Dai, S.; Hou, Y.; Onoue, M.; Zhang, S.; Gao, W.; Yan, X.; Graham, G.; Wu, R.; Pan, X. Revealing Surface Elemental Composition and Dynamic Processes Involved in Facet-Dependent Oxidation of Pt_3Co Nanoparticles via In Situ Transmission Electron Microscopy. *Nano Lett.* **2017**, *17*, 4683−4688.
(199) Altantzis, T.; Lobato, I.; De Backer, A.; Beche, A.; Zhang, Y.; Basak, S.; Porcu, M.; Xu, Q.; Sanchez-Iglesias, A.; Liz-Marzan, L. M.; Van Tendeloo, G.; Van Aert, S.; Bals, S. Three-Dimensional Quantification of the Facet Evolution of Pt Nanoparticles in a Variable Gaseous Environment. *Nano Lett.* **2019**, *19*, 477−481.

https://dx.doi.org/10.1021/acscatal.0c04789
ACS Catal. 2021, 11, 1136−1178

(200) Han, L.; Meng, Q.; Wang, D.; Zhu, Y.; Wang, J.; Du, X.; Stach, E. A.; Xin, H. L. Interrogation of Bimetallic Particle Oxidation in Three Dimensions at the Nanoscale. *Nat. Commun.* **2016**, *7*, 13335.
(201) Vanrompay, H.; Bladt, E.; Albrecht, W.; Béché, A.; Zakhozheva, M.; Sánchez-Iglesias, A.; Liz-Marzán, L. M.; Bals, S. 3D Characterization of Heat-Induced Morphological Changes of Au Nanostars by Fast In Situ Electron Tomography. *Nanoscale* **2018**, *10*, 22792−22801.
(202) Baaziz, W.; Bahri, M.; Gay, A.; Chaumonnot, A.; Uzio, D.; Valette, S.; Hirlimann, C.; Ersen, O. Thermal Behavior of Pd@SiO_2 Nanostructures in Various Gas Environments: A Combined 3D And in Situ TEM Approach. *Nanoscale* **2018**, *10*, 20178−20188.
(203) Xin, H. L.; Pach, E. A.; Diaz, R. E.; Stach, E. A.; Salmeron, M.; Zheng, H. Revealing Correlation of Valence State with Nanoporous Structure in Cobalt Catalyst Nanoparticles by In Situ Environmental TEM. *ACS Nano* **2012**, *6*, 4241−4247.
(204) Prestat, E.; Kulzick, M.; Dietrich, P.; Smith, M.; Tien, M.; Burke, M.; Haigh, S.; Zaluzec, N. In Situ Industrial Bimetallic Catalyst Characterization Using Scanning Transmission Electron Microscopy and X-Ray Absorption Spectroscopy at One Atmosphere and Elevated Temperature. *ChemPhysChem* **2017**, *18*, 2151−2156.
(205) Xiong, Y.; Yang, Y.; Joress, H.; Padgett, E.; Gupta, U.; Yarlagadda, V.; Agyeman-Budu, D. N.; Huang, X.; Moylan, T. E.; Zeng, R.; Kongkanand, A.; Escobedo, F. A.; Brock, J. D.; DiSalvo, F. J.; Muller, D. A.; Abruña, H. D. Revealing the Atomic Ordering of Binary Intermetallics Using *in Situ* Heating Techniques at Multilength Scales. *Proc. Natl. Acad. Sci. U. S. A.* **2019**, *116*, 1974−1983.
(206) Xiao, W.; Lei, W.; Gong, M.; Xin, H. L.; Wang, D. Recent Advances of Structurally Ordered Intermetallic Nanoparticles for Electrocatalysis. *ACS Catal.* **2018**, *8*, 3237−3256.
(207) Xiong, Y.; Yang, Y.; DiSalvo, F. J.; Abruña, H. D. Pt-Decorated Composition-Tunable Pd-Fe@Pd/C Core-Shell Nanoparticles with Enhanced Electrocatalytic Activity toward the Oxygen Reduction Reaction. *J. Am. Chem. Soc.* **2018**, *140*, 7248−7255.
(208) Chung, D.; Jun, S.; Yoon, G.; Kwon, S.; Shin, D.; Seo, P.; Yoo, J.; Shin, H.; Chung, Y.; Kim, H.; Mun, B.; Lee, K.; Lee, N.; Yoo, S.; Lim, D.; Kang, K.; Sung, Y.; Hyeon, T. Highly Durable and Active PtFe Nanocatalyst for Electrochemical Oxygen Reduction Reaction. *J. Am. Chem. Soc.* **2015**, *137*, 15478−15485.
(209) Yang, Y.; Chen, G.; Zeng, R.; Villarino, A. M.; DiSalvo, F. J.; van Dover, R. B.; Abruna, H. D. Combinatorial Studies of Palladium-Based Oxygen Reduction Electrocatalysts for Alkaline Fuel Cells. *J. Am. Chem. Soc.* **2020**, *142*, 3980−3988.
(210) Gunji, T.; Noh, S.; Tanabe, T.; Han, B.; Nien, C.; Ohsaka, T.; Matsumoto, F. Enhanced Electrocatalytic Activity of Carbon-Supported Ordered Intermetallic Palladium-Lead (Pd_3Pb) Nanoparticles toward Electrooxidation of Formic Acid. *Chem. Mater.* **2017**, *29*, 2906−2913.
(211) Yang, Y.; Xiao, W.; Feng, X.; Xiong, Y.; Gong, M.; Shen, T.; Lu, Y.; Abruña, H. D.; Wang, D. Golden Palladium Zinc Ordered Intermetallics as Oxygen Reduction Electrocatalysts. *ACS Nano* **2019**, *13*, 5968−5974.
(212) Kang, Y.; Murray, C. Synthesis and Electrocatalytic Properties of Cubic Mn-Pt Nanocrystals (nanocubes). *J. Am. Chem. Soc.* **2010**, *132*, 7568−7569.
(213) Zhu, J.; Yang, Y.; Chen, L.; Xiao, W.; Liu, H.; Abruña, H. D.; Wang, D. Copper-Induced Formation of Structurally Ordered Pt-Fe-Cu Ternary Intermetallic Electrocatalysts with Tunable Phase Structure and Improved Stability. *Chem. Mater.* **2018**, *30*, 5987−5995.
(214) Abe, H.; Matsumoto, F.; Alden, L.; Warren, S.; Abruña, H. D.; DiSalvo, F. J. Electrocatalytic Performance of Fuel Oxidation by Pt_3Ti Nanoparticles. *J. Am. Chem. Soc.* **2008**, *130*, 5452−5458.
(215) Xie, Y.; Yang, Y.; Muller, D. A.; Abruña, H. D.; Dimitrov, N.; Fang, J. Enhanced ORR Kinetics on Au-Doped Pt-Cu Porous Films in Alkaline Media. *ACS Catal.* **2020**, *10*, 9967−9976.
(216) Cui, Z.; Chen, H.; Zhao, M.; Marshall, D.; Yu, Y.; Abruña, H. D.; DiSalvo, F. J. Synthesis of Structurally Ordered Pt_3Ti and Pt_3V Nanoparticles as Methanol Oxidation Catalysts. *J. Am. Chem. Soc.* **2014**, *136*, 10206−10209.
(217) Sra, A.; Schaak, R. Synthesis of Atomically Ordered AuCu and $AuCu_3$ Nanocrystals from Bimetallic Nanoparticle Precursors. *J. Am. Chem. Soc.* **2004**, *126*, 6667−6672.
(218) Kang, Y.; Pyo, J.; Ye, X.; Gordon, T.; Murray, C. Synthesis, Shape Control, and Methanol Electro-Oxidation Properties of Pt-Zn Alloy and Pt_3Zn Intermetallic Nanocrystals. *ACS Nano* **2012**, *6*, 5642−5647.
(219) Wang, G.; Huang, B.; Xiao, L.; Ren, Z.; Chen, H.; Wang, D.; Abruña, H. D.; Lu, J.; Zhuang, L. Pt Skin on AuCu Intermetallic Substrate: A Strategy to Maximize Pt Utilization for Fuel Cells. *J. Am. Chem. Soc.* **2014**, *136*, 9643−9649.
(220) Yoshida, H.; Omote, H.; Takeda, S. Oxidation and Reduction Processes of Platinum Nanoparticles Observed at the Atomic Scale by Environmental Transmission Electron Microscopy. *Nanoscale* **2014**, *6*, 13113−13118.
(221) Yoshida, H.; Kuwauchi, Y.; Jinschek, J. R.; Sun, K.; Tanaka, S.; Kohyama, M.; Shimada, S.; Haruta, M.; Takeda, S. Visualizing Gas Molecules Interacting with Supported Nanoparticulate Catalysts at Reaction Conditions. *Science* **2012**, *335*, 317−319.
(222) Unocic, K.; Walden, F. S.; Marthe, N. L.; Datye, A. K.; Bigelow, W. C.; Allard, L. F. Introducing and Controlling Water Vapor in Closed-Cell In Situ Electron Microscopy Gas Reactions. *Microsc. Microanal.* **2020**, *26*, 229−239.
(223) Kamino, T.; Yaguchi, T.; Shimizu, T. Development and Application of a Sample Holder for In Situ Gaseous TEM Studies of Membrane Electrode Assemblies for Polymer Electrolyte Fuel Cells. *Microsc. Microanal.* **2017**, *23*, 945−950.
(224) Durst, J.; Simon, C.; Hasche, F.; Gasteiger, H. A. Hydrogen Oxidation and Evolution Reaction Kinetics on Carbon Supported Pt, Ir, Rh, and Pd Electrocatalysts in Acidic Media. *J. Electrochem. Soc.* **2015**, *162*, F190−F203.
(225) Bertoncello, P. Advances on scanning electrochemical microscopy (SECM) for energy. *Energy Environ. Sci.* **2010**, *3*, 1620−1633.
(226) Polcari, D.; Dauphin-Ducharme, P.; Mauzeroll, J. Scanning Electrochemical Microscopy: A Comprehensive Review of Experimental Parameters from 1989 to 2015. *Chem. Rev.* **2016**, *116*, 13234−13278.
(227) Liu, H. Y.; Fan, F. R. F.; Lin, C. W.; Bard, A. J. Scanning Electrochemical and Tunneling Ultramicroelectrode Microscope for High-Resolution Examination of Electrode Surfaces in Solution. *J. Am. Chem. Soc.* **1986**, *108*, 3838−3839.
(228) Kwak, J.; Bard, A. J. Scanning Electrochemical Microscopy. Apparatus and Two-Dimensional Scans of Conductive and Insulating Substrates. *Anal. Chem.* **1989**, *61*, 1794−1799.
(229) Rodríguez-López, J. N.; Minguzzi, A.; Bard, A. J. Reaction of Various Reductants with Oxide Films on Pt Electrodes as Studied by the Surface Interrogation Mode of Scanning Electrochemical Microscopy (SI-SECM): Possible Validity of a Marcus Relationship. *J. Phys. Chem. C* **2010**, *114*, 18645−18655.
(230) Rodriguez-Lopez, J.; Alpuche-Aviles, M. A.; Bard, A. J. Interrogation of Surfaces for the Quantification of Adsorbed Species on Electrodes: Oxygen on Gold and Platinum in Neutral Media. *J. Am. Chem. Soc.* **2008**, *130*, 16985−16995.
(231) Cornut, R.; Lefrou, C. New Analytical Approximation of Feedback Approach Curves with a Microdisk SECM Tip and Irreversible Kinetic Reaction at the Substrate. *J. Electroanal. Chem.* **2008**, *621*, 178−184.
(232) Wightman, R. M. Microvoltammetric Electrodes. *Anal. Chem.* **1981**, *53*, 1125A−1134A.
(233) Clausmeyer, J.; Schuhmann, W. Nanoelectrodes: Applications in Electrocatalysis, Single-Cell Analysis and High-Resolution Electrochemical Imaging. *TrAC, Trends Anal. Chem.* **2016**, *79*, 46−59.
(234) Sun, T.; Yu, Y.; Zacher, B. J.; Mirkin, M. V. Scanning Electrochemical Microscopy of Individual Catalytic Nanoparticles. *Angew. Chem., Int. Ed.* **2014**, *53*, 14120−14123.
(235) Meier, J.; Friedrich, K. A.; Stimming, U. Novel Method for the Investigation of Single Nanoparticle Reactivity. *Faraday Discuss.* **2002**, *121*, 365−372.

https://dx.doi.org/10.1021/acscatal.0c04789
ACS Catal. 2021, 11, 1136−1178

(236) Yu, Y.; Sun, T.; Mirkin, M. V. Scanning Electrochemical Microscopy of Single Spherical Nanoparticles: Theory and Particle Size Evaluation. *Anal. Chem.* **2015**, *87*, 7446−7453.
(237) Kim, J.; Renault, C.; Nioradze, N.; Arroyo-Currás, N. Y.; Leonard, K. C.; Bard, A. J. Electrocatalytic Activity of Individual Pt Nanoparticles Studied by Nanoscale Scanning Electrochemical Microscopy. *J. Am. Chem. Soc.* **2016**, *138*, 8560−8568.
(238) Liang, Z.; Ahn, H. S.; Bard, A. J. A Study of the Mechanism of the Hydrogen Evolution Reaction on Nickel by Surface Interrogation Scanning Electrochemical Microscopy. *J. Am. Chem. Soc.* **2017**, *139*, 4854−4858.
(239) Krumov, M. R.; Simpson, B. H.; Counihan, M. J.; Rodríguez-López, J. In Situ Quantification of Surface Intermediates and Correlation to Discharge Products on Hematite Photoanodes Using a Combined Scanning Electrochemical Microscopy Approach. *Anal. Chem.* **2018**, *90*, 3050−3057.
(240) Simpson, B. H.; Rodríguez-López, J. Redox Titrations via Surface Interrogation Scanning Electrochemical Microscopy at an Extended Semiconducting Surface for the Quantification of Photogenerated Adsorbed Intermediates. *Electrochim. Acta* **2015**, *179*, 74−83.
(241) Li, P.; Jin, Z.; Qian, Y.; Fang, Z.; Xiao, D.; Yu, G. Probing Enhanced Site Activity of Co-Fe Bimetallic Subnanoclusters Derived from Dual Cross-Linked Hydrogels for Oxygen Electrocatalysis. *ACS Energy Lett.* **2019**, *4*, 1793−1802.
(242) Fernández, J. L.; Walsh, D. A.; Bard, A. J. Thermodynamic Guidelines for the Design of Bimetallic Catalysts for Oxygen Electroreduction and Rapid Screening by Scanning Electrochemical Microscopy. M- Co (M: Pd, Ag, Au). *J. Am. Chem. Soc.* **2005**, *127*, 357−365.
(243) Rus, E. D.; Wang, H.; Legard, A. E.; Ritzert, N. L.; Van Dover, R. B.; Abruña, H. D. An Exchangeable-Tip Scanning Probe Instrument for the Analysis of Combinatorial Libraries of Electrocatalysts. *Rev. Sci. Instrum.* **2013**, *84*, 024101.
(244) Liang, Y.; Pfisterer, J. H.; McLaughlin, D.; Csoklich, C.; Seidl, L.; Bandarenka, A. S.; Schneider, O. Electrochemical Scanning Probe Microscopies in Electrocatalysis. *Small Methods* **2019**, *3*, 1800387.
(245) Bentley, C. L.; Kang, M.; Unwin, P. R. Scanning Electrochemical Cell Microscopy: New Perspectives on Electrode Processes in Action. *Curr. Opin. Electrochem.* **2017**, *6*, 23−30.
(246) Mariano, R. G.; McKelvey, K.; White, H. S.; Kanan, M. W. Selective Increase in CO_2 Electroreduction Activity at Grain-Boundary Surface Terminations. *Science* **2017**, *358*, 1187−1192.
(247) Gao, R.; Edwards, M. A.; Qiu, Y.; Barman, K.; White, H. S. Visualization of Hydrogen Evolution at Individual Platinum Nanoparticles at a Buried Interface. *J. Am. Chem. Soc.* **2020**, *142*, 8890−8896.
(248) Bentley, C. L.; Kang, M.; Unwin, P. R. Nanoscale Structure Dynamics within Electrocatalytic Materials. *J. Am. Chem. Soc.* **2017**, *139*, 16813−16821.
(249) Ebejer, N.; Schnippering, M.; Colburn, A. W.; Edwards, M. A.; Unwin, P. R. Localized High Resolution Electrochemistry and Multifunctional Imaging: Scanning Electrochemical Cell Microscopy. *Anal. Chem.* **2010**, *82*, 9141−9145.
(250) Bruckenstein, S.; Gadde, R. R. Use of a Porous Electrode for in Situ Mass Spectrometric Determination of Volatile Electrode Reaction Products. *J. Am. Chem. Soc.* **1971**, *93*, 793−794.
(251) Wolter, O.; Heitbaum, J. Differential Electrochemical Mass Spectroscopy (DEMS) — A New Method for the Study of Electrode Processes. *Ber. Bunsenges. Phys. Chem.* **1984**, *88*, 2−6.
(252) Baltruschat, H. Differential Electrochemical Mass Spectrometry. *J. Am. Soc. Mass Spectrom.* **2004**, *15*, 1693−1706.
(253) Oberacher, H.; Pitterl, F.; Erb, R.; Plattner, S. Mass Spectrometric Methods for Monitoring Redox Processes in Electrochemical Cells. *Mass Spectrom. Rev.* **2015**, *34*, 64−92.
(254) Wang, H.; Abruña, H. D. Origin of Multiple Peaks in the Potentiodynamic Oxidation of CO Adlayers on Pt and Ru-Modified Pt Electrodes. *J. Phys. Chem. Lett.* **2015**, *6*, 1899−1906.
(255) Gao, Y.; Tsuji, H.; Hattori, H.; Kita, H. New On-Line Mass Spectrometer System Designed for Platinum-Single Crystal Electrode and Electroreduction of Acetylene. *J. Electroanal. Chem.* **1994**, *372*, 195−200.
(256) Wang, H.; Abruña, H. D. Electrocatalysis of Direct Alcohol Fuel Cells: Quantitative DEMS Studies. *Struct. Bonding (Berlin, Ger.)* **2011**, *141*, 33−83.
(257) Ashton, S. J. *Design, Construction and Research Application of a Differential Electrochemical Mass Spectrometer (DEMS)*; Springer: Heidelberg, Germany, 2012.
(258) Zeng, R.; Yang, Y.; Shen, T.; Wang, H.; Xiong, Y.; Zhu, J.; Wang, D.; Abruña, H. D. Methanol Oxidation Using Ternary Ordered Intermetallic Electrocatalysts: A DEMS Study. *ACS Catal.* **2020**, *10*, 770−776.
(259) Heinen, M.; Chen, Y. X.; Jusys, Z.; Behm, R. J. In Situ ATR-FTIRS Coupled with on-Line DEMS under Controlled Mass Transport Conditions—A Novel Tool for Electrocatalytic Reaction Studies. *Electrochim. Acta* **2007**, *52*, 5634−5643.
(260) Jusys, Z.; Massong, H.; Baltruschat, H. A New Approach for Simultaneous DEMS and EQCM: Electro-Oxidation of Adsorbed CO on Pt and Pt-Ru. *J. Electrochem. Soc.* **1999**, *146*, 1093.
(261) Jambunathan, K.; Jayaraman, S.; Hillier, A. C. A Multielectrode Electrochemical and Scanning Differential Electrochemical Mass Spectrometry Study of Methanol Oxidation on Electrodeposited $PtxRu_Y$. *Langmuir* **2004**, *20*, 1856−1863.
(262) Jambunathan, K.; Hillier, A. C. Measuring Electrocatalytic Activity on a Local Scale with Scanning Differential Electrochemical Mass Spectrometry. *J. Electrochem. Soc.* **2003**, *150*, E312−E320.
(263) Wang, H.; Rus, E.; Abruña, H. D. New Double-Band-Electrode Channel Flow Differential Electrochemical Mass Spectrometry Cell: Application for Detecting Product Formation during Methanol Electrooxidation. *Anal. Chem.* **2010**, *82*, 4319−4324.
(264) Momotenko, D.; Qiao, L.; Cortes-Salazar, F.; Lesch, A.; Wittstock, G.; Girault, H. H. Electrochemical Push-Pull Scanner with Mass Spectrometry Detection. *Anal. Chem.* **2012**, *84*, 6630−6637.
(265) Chen, W.; Cai, J.; Yang, J.; Sartin, M. M.; Chen, Y.-X. The Kinetics of Methanol Oxidation at a Pt Film Electrode, a Combined Mass and Infrared Spectroscopic Study. *J. Electroanal. Chem.* **2017**, *800*, 89−98.
(266) Pérez-Rodríguez, S.; Corengia, M.; García, G.; Zinola, C. F.; Lázaro, M. J.; Pastor, E. Gas Diffusion Electrodes for Methanol Electrooxidation Studied by a New DEMS Configuration: Influence of the Diffusion Layer. *Int. J. Hydrogen Energy* **2012**, *37*, 7141−7151.
(267) Jusys, Z.; Behm, R. J. DEMS Analysis of Small Organic Molecule Electrooxidation: A High-Temperature High-Pressure DEMS Study. In *ECS Transactions*; ECS, 2008; Vol. *16*, pp 1243−1251.
(268) Niether, C.; Rau, M. S.; Cremers, C.; Jones, D. J.; Pinkwart, K.; Tübke, J. Development of a Novel Experimental DEMS Set-up for Electrocatalyst Characterization under Working Conditions of High Temperature Polymer Electrolyte Fuel Cells. *J. Electroanal. Chem.* **2015**, *747*, 97−103.
(269) Wang, H.; Baltruschat, H. DEMS Study on Methanol Oxidation at Poly- and Monocrystalline Platinum Electrodes: The Effect of Anion, Temperature, Surface Structure, Ru Adatom, and Potential. *J. Phys. Chem. C* **2007**, *111*, 7038−7048.
(270) Clark, E. L.; Singh, M. R.; Kwon, Y.; Bell, A. T. Differential Electrochemical Mass Spectrometer Cell Design for Online Quantification of Products Produced during Electrochemical Reduction of CO_2. *Anal. Chem.* **2015**, *87*, 8013−8020.
(271) Debe, M. K. Electrocatalyst Approaches and Challenges for Automotive Fuel Cells. *Nature* **2012**, *486*, 43−51.
(272) Kakati, N.; Maiti, J.; Lee, S. H.; Jee, S. H.; Viswanathan, B.; Yoon, Y. S. Anode Catalysts for Direct Methanol Fuel Cells in Acidic Media: Do We Have Any Alternative for Pt or Pt-Ru? *Chem. Rev.* **2014**, *114*, 12397−12429.
(273) Shen, T.; Chen, S.; Zeng, R.; Gong, M.; Zhao, T.; Lu, Y.; Liu, X.; Xiao, D.; Yang, Y.; Hu, J.; Wang, D.; Xin, H. L.; Abruña, H. D. Tailoring the Antipoisoning Performance of Pd for Formic Acid

https://dx.doi.org/10.1021/acscatal.0c04789
ACS Catal. 2021, 11, 1136−1178

Electrooxidation via an Ordered PdBi Intermetallic. *ACS Catal.* **2020**, *10*, 9977−9985.
(274) Wang, D.; Subban, C. V.; Wang, H.; Rus, E.; DiSalvo, F. J.; Abruña, H. D. Highly Stable and CO-Tolerant Pt/$Ti_{0.7}W_{0.3}O_2$ Electrocatalyst for Proton-Exchange Membrane Fuel Cells. *J. Am. Chem. Soc.* **2010**, *132*, 10218−10220.
(275) Wolter, O.; Willsau, J.; Heitbaum, J. Reaction Pathways of the Anodic Oxidation of Formic Acid on Pt Evidenced by ^{18}O Labeling-A DEMS Study. *J. Electrochem. Soc.* **1985**, *132*, 1635−1638.
(276) Kita, H.; Lei, H.-W. Oxidation of Formic Acid in Acid Solution on Pt Single-Crystal Electrodes. *J. Electroanal. Chem.* **1995**, *388*, 167−177.
(277) Xia, X. H.; Iwasita, T. Influence of Underpotential Deposited Lead upon the Oxidation of HCOOH in $HClO_4$ at Platinum Electrodes. *J. Electrochem. Soc.* **1993**, *140*, 2559−2565.
(278) Xia, X. H. New Insights into the Influence of Upd Sn on the Oxidation of Formic Acid on Platinum in Acidic Solution. *Electrochim. Acta* **1999**, *45*, 1057−1066.
(279) Vidal-Iglesias, F. J.; Solla-Gullón, J.; Herrero, E.; Aldaz, A.; Feliu, J. M. Formic Acid Oxidation on Pd-Modified Pt(100) and Pt(111) Electrodes: A DEMS Study. *J. Appl. Electrochem.* **2006**, *36*, 1207−1214.
(280) John, J.; Wang, H.; Rus, E. D.; Abruña, H. D. Mechanistic Studies of Formate Oxidation on Platinum in Alkaline Medium. *J. Phys. Chem. C* **2012**, *116*, 5810−5820.
(281) Willsau, J.; Wolter, O.; Heitbaum, J. On the Nature of the Adsorbate during Methanol Oxidation at Platinum: A DEMS Study. *J. Electroanal. Chem. Interfacial Electrochem.* **1985**, *185*, 163−170.
(282) Iwasita, T.; Vielstich, W. On-Line Mass Spectroscopy of Volatile Products during Methanol Oxidation at Platinum in Acid Solutions. *J. Electroanal. Chem. Interfacial Electrochem.* **1986**, *201*, 403−408.
(283) Wang, H.; Löffler, T.; Baltruschat, H. Formation of Intermediates during Methanol Oxidation: A Quantitative DEMS Study. *J. Appl. Electrochem.* **2001**, *31*, 759−765.
(284) Krausa, M.; Vielstich, W. Study of the Electrocatalytic Influence of Pt/Ru and Ru on the Oxidation of Residues of Small Organic Molecules. *J. Electroanal. Chem.* **1994**, *379*, 307−314.
(285) Jusys, Z.; Kaiser, J.; Behm, R. J. Composition and Activity of High Surface Area PtRu Catalysts towards Adsorbed CO and Methanol Electrooxidation: A DEMS Study. *Electrochim. Acta* **2002**, *47*, 3693−3706.
(286) Bergamaski, K.; Pinheiro, A. L. N.; Teixeira-Neto, E.; Nart, F. C. Nanoparticle Size Effects on Methanol Electrochemical Oxidation on Carbon Supported Platinum Catalysts. *J. Phys. Chem. B* **2006**, *110*, 19271−19279.
(287) Nagao, R.; Cantane, D. A.; Lima, F. H. B.; Varela, H. Influence of Anion Adsorption on the Parallel Reaction Pathways in the Oscillatory Electro-Oxidation of Methanol. *J. Phys. Chem. C* **2013**, *117*, 15098−15105.
(288) Seidel, Y. E.; Schneider, A.; Jusys, Z.; Wickman, B.; Kasemo, B.; Behm, R. J. Transport Effects in the Electrooxidation of Methanol Studied on Nanostructured Pt/Glassy Carbon Electrodes. *Langmuir* **2010**, *26*, 3569−3578.
(289) Chen, W.; Uwitonze, N.; He, F.; Sartin, M. M.; Cai, J.; Chen, Y. X. Effect of Mass Transfer and Solution Composition on the Quantification of Reaction Kinetics by Differential Electrochemical Mass Spectrometry. *J. Energy Chem.* **2021**, *56*, 412−419.
(290) Chen, W.; Tao, Q.; Cai, J.; Chen, Y. X. The Effect of Alcohol Concentration on the Mass Signal of CO_2 Detected by Differential Mass Spectrometry. *Electrochem. Commun.* **2014**, *48*, 10−12.
(291) Reichert, R.; Schnaidt, J.; Jusys, Z.; Behm, R. J. The Influence of Reactive Side Products in Electrocatalytic Reactions: Methanol Oxidation as Case Study. *ChemPhysChem* **2013**, *14*, 3678−3681.
(292) Rizo, R.; Arán-Ais, R. M.; Padgett, E.; Muller, D. A.; Lázaro, M. J.; Solla-Gullón, J.; Feliu, J. M.; Pastor, E.; Abruña, H. D. Pt-$Rich_{Core}$/Sn-$Rich_{Subsurface}$/Pt_{Skin} Nanocubes As Highly Active and Stable Electrocatalysts for the Ethanol Oxidation Reaction. *J. Am. Chem. Soc.* **2018**, *140*, 3791−3797.
(293) Willsau, J.; Heitbaum, J. Elementary Steps of Ethanol Oxidation on Pt in Sulfuric Acid as Evidenced by Isotope Labelling. *J. Electroanal. Chem. Interfacial Electrochem.* **1985**, *194*, 27−35.
(294) Iwasita, T.; Pastor, E. A Dems and FTir Spectroscopic Investigation of Adsorbed Ethanol on Polycrystalline Platinum. *Electrochim. Acta* **1994**, *39*, 531−537.
(295) Schmiemann, U.; Müller, U.; Baltruschat, H. The Influence of the Surface Structure on the Adsorption of Ethene, Ethanol and Cyclohexene as Studied by DEMS. *Electrochim. Acta* **1995**, *40*, 99−107.
(296) Abd-El-Latif, A. A.; Mostafa, E.; Huxter, S.; Attard, G.; Baltruschat, H. Electrooxidation of Ethanol at Polycrystalline and Platinum Stepped Single Crystals: A Study by Differential Electrochemical Mass Spectrometry. *Electrochim. Acta* **2010**, *55*, 7951−7960.
(297) Mostafa, E.; Abd-El-Latif, A.-E.-A. A.; Ilsley, R.; Attard, G.; Baltruschat, H. Quantitative DEMS Study of Ethanol Oxidation: Effect of Surface Structure and Sn Surface Modification. *Phys. Chem. Chem. Phys.* **2012**, *14*, 16115−16129.
(298) Bach Delpeuch, A.; Chatenet, M.; Rau, M. S.; Cremers, C. Influence of H- and OH-Adsorbates on the Ethanol Oxidation Reaction - A DEMS Study. *Phys. Chem. Chem. Phys.* **2015**, *17*, 10881−10893.
(299) Busó-Rogero, C.; Brimaud, S.; Solla-Gullon, J.; Vidal-Iglesias, F. J.; Herrero, E.; Behm, R. J.; Feliu, J. M. Ethanol Oxidation on Shape-Controlled Platinum Nanoparticles at Different PHs: A Combined in Situ IR Spectroscopy and Online Mass Spectrometry Study. *J. Electroanal. Chem.* **2016**, *763*, 116−124.
(300) Bach Delpeuch, A.; Jacquot, M.; Chatenet, M.; Cremers, C. The Influence of Mass-Transport Conditions on the Ethanol Oxidation Reaction (EOR) Mechanism of Pt/C Electrocatalysts. *Phys. Chem. Chem. Phys.* **2016**, *18*, 25169−25175.
(301) Rao, V.; Hariyanto; Cremers, C.; Stimming, U. Investigation of the Ethanol Electro-Oxidation in Alkaline Membrane Electrode Assembly by Differential Electrochemical Mass Spectrometry. *Fuel Cells* **2007**, *7*, 417−423.
(302) Bayer, D.; Cremers, C.; Baltruschat, H.; Tübke, J. The Electro-Oxidation of Ethanol in Alkaline Medium at Different Catalyst Metals. In *ECS Transactions*; The Electrochemical Society, 2011; Vol. *41*, pp 1669−1680.
(303) Sharma, S.; Pollet, B. G. Support Materials for PEMFC and DMFC Electrocatalysts—A Review. *J. Power Sources* **2012**, *208*, 96−119.
(304) Castanheira, L.; Silva, W. O.; Lima, F. H. B.; Crisci, A.; Dubau, L.; Maillard, F. Carbon Corrosion in Proton-Exchange Membrane Fuel Cells: Effect of the Carbon Structure, the Degradation Protocol, and the Gas Atmosphere. *ACS Catal.* **2015**, *5*, 2184−2194.
(305) Li, W.; Lane, A. M. Analysis of Oxygen Sources and Reaction Pathways of Carbon Support Corrosion at the Cathode in PEMFC Using Oxygen-18 DEMS. *Electrochim. Acta* **2010**, *55*, 6926−6931.
(306) Li, W.; Lane, A. M. Investigation of Pt Catalytic Effects on Carbon Support Corrosion of the Cathode Catalyst in PEM Fuel Cells Using DEMS Spectra. *Electrochem. Commun.* **2009**, *11*, 1187−1190.
(307) Colmenares, L. C.; Wurth, A.; Jusys, Z.; Behm, R. J. Model Study on the Stability of Carbon Support Materials under Polymer Electrolyte Fuel Cell Cathode Operation Conditions. *J. Power Sources* **2009**, *190*, 14−24.
(308) Möller, S.; Barwe, S.; Masa, J.; Wintrich, D.; Seisel, S.; Baltruschat, H.; Schuhmann, W. Online Monitoring of Electrochemical Carbon Corrosion in Alkaline Electrolytes by Differential Electrochemical Mass Spectrometry. *Angew. Chem., Int. Ed.* **2020**, *59*, 1585−1589.
(309) Cremers, C.; Jurzinsky, T.; Meier, J.; Schade, A.; Branghofer, M.; Pinkwart, K.; Tübke, J. DEMS and Online Mass Spectrometry Studies of the Carbon Support Corrosion under Various Polymer Electrolyte Membrane Fuel Cell Operating Conditions. *J. Electrochem. Soc.* **2018**, *165*, F3307−F3315.

https://dx.doi.org/10.1021/acscatal.0c04789
ACS Catal. 2021, 11, 1136−1178

(310) Gebauer, C.; Jusys, Z.; Behm, R. J. On the Role of the Support in Pt Anode Catalyst Degradation under Simulated H_2 Fuel Starvation Conditions. *J. Electrochem. Soc.* **2018**, *165*, J3342−J3349.
(311) Rus, E. D.; Wang, H.; Wang, D.; Abruña, H. D. A Mechanistic Differential Electrochemical Mass Spectrometry (DEMS) and in Situ Fourier Transform Infrared Investigation of Dimethoxymethane Electro-Oxidation at Platinum. *J. Phys. Chem. C* **2011**, *115*, 13293−13302.
(312) Zheng, Y.; Chen, W.; Zuo, X.-Q.; Cai, J.; Chen, Y.-X. The Kinetics of the Oxidation and Reduction of H_2O_2 at a Pt Electrode: A Differential Electrochemical Mass Spectrometric Study. *Electrochem. Commun.* **2016**, *73*, 38−41.
(313) Schnaidt, J.; Heinen, M.; Jusys, Z.; Behm, R. J. Oxidation of the Partly Oxidized Ethylene Glycol Oxidation Products Glycolaldehyde, Glyoxal, Glycolic Acid, Glyoxylic Acid, and Oxalic Acid on Pt Electrodes: A Combined ATR-FTIRS and DEMS Spectroelectrochemical Study. *J. Phys. Chem. C* **2013**, *117*, 12689−12701.
(314) Stefanova, A.; Ayata, S.; Erem, A.; Ernst, S.; Baltruschat, H. Mechanistic Studies on Boron-Doped Diamond: Oxidation of Small Organic Molecules. *Electrochim. Acta* **2013**, *110*, 560−569.
(315) Bondue, C. J.; Calle-Vallejo, F.; Figueiredo, M. C.; Koper, M. T. M. Structural Principles to Steer the Selectivity of the Electrocatalytic Reduction of Aliphatic Ketones on Platinum. *Nat. Catal.* **2019**, *2*, 243−250.
(316) Kamimura, J.; Bogdanoff, P.; Lähnemann, J.; Hauswald, C.; Geelhaar, L.; Fiechter, S.; Riechert, H. Photoelectrochemical Properties of (In,Ga)N Nanowires for Water Splitting Investigated by in Situ Electrochemical Mass Spectroscopy. *J. Am. Chem. Soc.* **2013**, *135*, 10242−10245.
(317) Ullman, A. M.; Brodsky, C. N.; Li, N.; Zheng, S.-L.; Nocera, D. G. Probing Edge Site Reactivity of Oxidic Cobalt Water Oxidation Catalysts. *J. Am. Chem. Soc.* **2016**, *138*, 4229−4236.
(318) Amin, H. M. A.; Baltruschat, H. How Many Surface Atoms in Co_3O_4 Take Part in Oxygen Evolution? Isotope Labeling Together with Differential Electrochemical Mass Spectrometry. *Phys. Chem. Chem. Phys.* **2017**, *19*, 25527−25536.
(319) Görlin, M.; Chernev, P.; Ferreira de Araújo, J.; Reier, T.; Dresp, S.; Paul, B.; Krähnert, R.; Dau, H.; Strasser, P. Oxygen Evolution Reaction Dynamics, Faradaic Charge Efficiency, and the Active Metal Redox States of Ni-Fe Oxide Water Splitting Electrocatalysts. *J. Am. Chem. Soc.* **2016**, *138*, 5603−5614.
(320) Ullman, A. M.; Liu, Y.; Huynh, M.; Bediako, D. K.; Wang, H.; Anderson, B. L.; Powers, D. C.; Breen, J. J.; Abruña, H. D.; Nocera, D. G. Water Oxidation Catalysis by Co(II) Impurities in $Co(III)_4O_4$ Cubanes. *J. Am. Chem. Soc.* **2014**, *136*, 17681−17688.
(321) Nitopi, S.; Bertheussen, E.; Scott, S. B.; Liu, X.; Engstfeld, A. K.; Horch, S.; Seger, B.; Stephens, I. E. L.; Chan, K.; Hahn, C.; Nørskov, J. K.; Jaramillo, T. F.; Chorkendorff, I. Progress and Perspectives of Electrochemical CO_2 Reduction on Copper in Aqueous Electrolyte. *Chem. Rev.* **2019**, *119*, 7610−7672.
(322) Grote, J. P.; Zeradjanin, A. R.; Cherevko, S.; Mayrhofer, K. J. J. Coupling of a Scanning Flow Cell with Online Electrochemical Mass Spectrometry for Screening of Reaction Selectivity. *Rev. Sci. Instrum.* **2014**, *85*, 104101.
(323) Clark, E. L.; Bell, A. T. Direct Observation of the Local Reaction Environment during the Electrochemical Reduction of CO_2. *J. Am. Chem. Soc.* **2018**, *140*, 7012−7020.
(324) Levi, M. D.; Shpigel, N.; Sigalov, S.; Dargel, V.; Daikhin, L.; Aurbach, D. In Situ Porous Structure Characterization of Electrodes for Energy Storage and Conversion by EQCM-D: A Review. *Electrochim. Acta* **2017**, *232*, 271−284.
(325) Shpigel, N.; Levi, M. D.; Sigalov, S.; Daikhin, L.; Aurbach, D. In Situ Real-Time Mechanical and Morphological Characterization of Electrodes for Electrochemical Energy Storage and Conversion by Electrochemical Quartz Crystal Microbalance with Dissipation Monitoring. *Acc. Chem. Res.* **2018**, *51*, 69−79.
(326) Schumacher, R. The Quartz Microbalance: A Novel Approach to the In-Situ Investigation of Interfacial Phenomena at the Solid/Liquid Junction. *Angew. Chem., Int. Ed. Engl.* **1990**, *29*, 329−343.
(327) Buttry, D. A.; Ward, M. D. Measurement of Interfacial Processes at Electrode Surfaces with the Electrochemical Quartz Crystal Microbalance. *Chem. Rev.* **1992**, *92*, 1355−1379.
(328) Bruckenstein, S.; Shay, M. Experimental Aspects of Use of the Quartz Crystal Microbalance in Solution. *Electrochim. Acta* **1985**, *30*, 1295−1300.
(329) Gabrielli, C.; Keddam, M.; Torresi, R. Calibration of the Electrochemical Quartz Crystal Microbalance. *J. Electrochem. Soc.* **1991**, *138*, 2657−2660.
(330) Vatankhah, G.; Lessard, J.; Jerkiewicz, G.; Zolfaghari, A.; Conway, B. E. Dependence of the Reliability of Electrochemical Quartz-Crystal Nanobalance Mass Responses on the Calibration Constant, C_f: Analysis of Three Procedures for Its Determination. *Electrochim. Acta* **2003**, *48*, 1613−1622.
(331) Moore, C. E.; Afsahi, F.; Young, A. P.; Gyenge, E. L. Vibrating Powders: Electrochemical Quartz Crystal Microbalance Study of IrO_2 and Pt/C Catalyst Layers for Voltage Reversal Tolerant Anodes in Fuel Cells. *J. Phys. Chem. C* **2019**, *123*, 23361−23373.
(332) Gu, N.; Niu, L.; Dong, S. Simultaneous Determination of Both the Calibration Constant in an Electrochemical Quartz Crystal Microbalance and the Active Surface Area of a Polycrystalline Gold Electrode. *Electrochem. Commun.* **2000**, *2*, 48−50.
(333) Martín, A. J.; Chaparro, A. M.; Daza, L. EQCM Study of the Electrodeposition of Pt-WO_3 and Its Catalytic Activity Towards the ORR. *ECS Trans.* **2010**, *33*, 309−320.
(334) Asen, L.; Ju, W.; Mostafa, E.; Martens, S.; Heiz, U.; Stimming, U.; Schneider, O. Electrodeposition of Pt-Rare Earth Alloys as ORR Catalysts for Fuel Cells. *ECS Trans.* **2016**, *75*, 323−332.
(335) Vigier, F.; Gloaguen, F.; Leger, J.-M.; Lamy, C. Electrochemical and Spontaneous Deposition of Ruthenium at Platinum Electrodes for Methanol Oxidation: An Electrochemical Quartz Crystal Microbalance Study. *Electrochim. Acta* **2001**, *46*, 4331−4337.
(336) Liu, N.; Zhang, C.; Chao, L.; Xiong, X.; Liu, H.; Cheng, Y.; Xie, Q. Preparation of a Thin- Film Pt Electrocatalyst by MnO_2 Electrodeposition and Galvanic Replacement Reaction for Oxidation of Methanol. *J. Electroanal. Chem.* **2019**, *853*, 113553.
(337) Chao, L.; Liu, N.; Xiong, X.; He, F.; Huang, T.; Xie, Q.; Yao, S. Preparation of an Ultrathin Pt Electrocatalyst via a Galvanic Replacement Reaction of Electrodeposited CuCl for the Oxidation of Methanol in an Alkaline Medium. *Chem. Commun.* **2018**, *54*, 3743−3746.
(338) Zhang, C.; Chao, L.; Wang, L.; Cheng, Y.; Xie, Q. Preparation of a Pt Thin-Film Modified Electrode for Alkaline Electrocatalytic Oxidation of Methanol by $Cu(OH)_2$ Electrodeposition and Galvanic Replacement Reaction. *Electrochim. Acta* **2020**, *330*, 135234.
(339) Hu, X.; Vrubel, H. Growth and Activation of an Amorphous Molybdenum Sulfide Hydrogen Evolving Catalyst. *ACS Catal.* **2013**, *3* (3), 2002−2011.
(340) Lee, C.; Tseng, C.; Wu, R.; Wu, C.; Syu, S. Catalytic Characterization of Hollow Silver/Palladium Nanoparticles Synthesized by a Displacement Reaction. *Electrochim. Acta* **2009**, *54*, 5544−5547.
(341) He, W.; Liberman, I.; Rozenberg, I.; Ifraemov, R.; Hod, I. Electrochemically Driven Cation Exchange Enables the Rational Design of Active CO_2 Reduction Electrocatalysts. *Angew. Chem., Int. Ed.* **2020**, *59*, 8262−8269.
(342) Fayette, M.; Nelson, A.; Robinson, R. D. Electrophoretic Deposition Improves Catalytic Performance of Co_3O_4 Nanoparticles for Oxygen Reduction/Oxygen Evolution Reactions. *J. Mater. Chem. A* **2015**, *3*, 4274−4283.
(343) Łukaszewski, M.; Czerwinski, A. Dissolution of Noble Metals and Their Alloys Studied by Electrochemical Quartz Crystal Microbalance. *J. Electroanal. Chem.* **2006**, *589*, 38−45.
(344) Sugawara, Y.; Yadav, A. P.; Nishikata, A.; Tsuru, T. EQCM Study on Dissolution of Ruthenium in Sulfuric Acid. *J. Electrochem. Soc.* **2008**, *155*, 897−902.
(345) Watanabe, M.; Ozuka, H.; Uchida, H. Electrochemical Quartz Crystal Microbalance Analysis of CO-Tolerance at Pt-Fe Alloy Electrodes. *Electrochim. Acta* **2002**, *47*, 3629−3636.

https://dx.doi.org/10.1021/acscatal.0c04789
ACS Catal. 2021, 11, 1136−1178

(346) Ofstad, A. B.; Thomassen, M. S.; Gomez de la Fuente, J. L.; Seland, F.; Moller-Holst, S.; Sunde, S. Assessment of Platinum Dissolution from a Pt/C Fuel Cell Catalyst: An Electrochemical Quartz Crystal Microbalance Study. *J. Electrochem. Soc.* **2010**, *157*, B621−B627.
(347) Munichandraiah, N.; Irshad, A. EQCM Investigation of Electrochemical Deposition and Stability of Co-Pi Oxygen Evolution Catalyst of Solar Energy Storage. *J. Phys. Chem. C* **2013**, *117*, 8001−8008.
(348) Han, S.; Liu, S.; Yin, S.; Chen, L.; He, Z. Electrodeposited Co-Doped Fe_3O_4 Thin Films as Efficient Catalysts for the Oxygen Evolution Reaction. *Electrochim. Acta* **2016**, *210*, 942−949.
(349) Luo, S.; Li, X.; Wang, M.; Zhang, X.; Gao, W.; Su, S.; Liu, G.; Luo, M. Long-Term Electrocatalytic N_2 Fixation by MOF-Derived Y-Stabilized ZrO_2: Insight into the Deactivation Mechanism. *J. Mater. Chem. A* **2020**, *8*, 5647−5654.
(350) Visscher, W.; Gootzen, J. F. E.; Cox, A. P.; van Veen, J. A. R. Electrochemical Quartz Crystal Microbalance Measurements of CO Adsorption and Oxidation on Pt in Various Electrolytes. *Electrochim. Acta* **1998**, *43*, 533−547.
(351) Siwek, H.; Łukaszewski, M.; Czerwinski, A. Electrochemical Study on the Adsorption of Carbon Oxides and Oxidation of Their Adsorption Products on Platinum Group Metals and Alloys. *Phys. Chem. Chem. Phys.* **2008**, *10*, 3752−3765.
(352) Łukaszewski, M.; Siwek, H.; Czerwinski, A. Analysis of the Electrochemical Quartz Crystal Microbalance Response during Oxidation of Carbon Oxides Adsorption Products on Platinum Group Metals and Alloys. *J. Solid State Electrochem.* **2010**, *14*, 1279−1292.
(353) Kanezashi, I.; Nohara, S.; Omura, J.; Watanabe, M.; Uchida, H. Electrochemical Quartz Crystal Microbalance Analysis of the CO Oxidation Reaction at Pt Alloy Electrodes. *J. Electroanal. Chem.* **2011**, *662*, 123−129.
(354) Wilde, C. P.; Zhang, M. Oxidation of Glucose at Electrodeposited Platinum Electrodes in Alkaline Solution. *J. Chem. Soc., Faraday Trans.* **1993**, *89*, 385−389.
(355) Wilde, C. P.; Zhang, M. Chemisorption and Oxidation of Methanol at Polycrystalline Pt In Acid Solutions. *Electrochim. Acta* **1994**, *39*, 347−354.
(356) Frelink, T.; Visscher, W.; van Veen, J. A. R. Measurement of the Ru Surface Content of Electrocodeposited PtRu Electrodes with the Electrochemical Quartz Crystal Microbalance: Implications for Methanol and CO Electrooxidation. *Langmuir* **1996**, *12*, 3702−3708.
(357) Omura, J.; Yano, J.; Watanabe, M.; Uchida, H. Electrochemical Quartz Crystal Microbalance Analysis of the Oxygen Reduction Reaction on Pt-Based Electrodes. Part 1: Effect of Adsorbed Anions on the Oxygen Reduction Activities of Pt in HF, $HClO_4$, and H_2SO_4 Solutions. *Langmuir* **2011**, *27*, 6464−6470.
(358) Omura, J.; Yano, H.; Tryk, D. A.; Watanabe, M.; Uchida, H. Electrochemical Quartz Crystal Microbalance Analysis of the Oxygen Reduction Reaction on Pt-Based Electrodes. Part 2: Adsorption of Oxygen Species and ClO_4^- Anions on Pt and Pt-Co Alloy in $HClO_4$ Solutions. *Langmuir* **2014**, *30*, 432−439.
(359) El-Jemni, M. A.; Abdel-Samad, H. S.; Essa, A. S.; Hassan, H. H. Controlled Electrodeposited Cobalt Phases for Efficient OER Catalysis, RRDE and EQCM Studies. *Electrochim. Acta* **2019**, *313*, 403−414.
(360) Taviot-Gueho, C.; Vialat, P.; Leroux, F.; Razzaghi, F.; Perrot, H.; Sel, O.; Jensen, N. D.; Nielsen, U. G.; Peulon, S.; Elkaim, E.; Mousty, C. Dynamic Characterization of Inter- and Intralamellar Domains of Cobalt-Based Layered Double Hydroxides upon Electrochemical Oxidation. *Chem. Mater.* **2016**, *28*, 7793−7806.
(361) Soliman, A. B.; Abdel-Samad, H. S.; Abdel Rehim, S. S.; Ahmed, M. A.; Hassan, H. H. High Performance Nano-Ni/Graphite Electrode for Electro-Oxidation in Direct Alkaline Ethanol Fuel Cells. *J. Power Sources* **2016**, *325*, 653−663.
(362) Vyas, A. N.; Desai, M. A.; Phase, D. M.; Saratale, R. G.; Ambekar, J. D.; Kale, B. B.; Pathan, H. M.; Sartale, S. D. Nickel Nanoparticles Grown by Successive Ionic Layer Adsorption and Reaction Method for Ethanol Electrooxidation and Electrochemical Quartz. *New J. Chem.* **2019**, *43*, 2955−2965.
(363) Wehrens-Dijksma, M.; Notten, P. H. L. Electrochemical Quartz Microbalance Characterization of $Ni(OH)_2$-Based Thin Film Electrodes. *Electrochim. Acta* **2006**, *51*, 3609−3621.
(364) Wu, T.; Scivetti, I.; Chen, J.; Wang, J.; Teobaldi, G.; Hu, C.; Hardwick, L. J. Quantitative Resolution of Complex Stoichiometric Changes during Electrochemical Cycling by Density Functional Theory-Assisted Electrochemical Quartz Crystal Microbalance. *ACS Appl. Energy Mater.* **2020**, *3*, 3347−3357.
(365) John, J.; Hugar, K. M.; Rivera-Meléndez, J.; Kostalik, H. A.; Rus, E. D.; Wang, H.; Coates, G. W.; Abruña, H. D. An Electrochemical Quartz Crystal Microbalance Study of a Prospective Alkaline Anion Exchange Membrane Material for Fuel Cells: Anion Exchange Dynamics and Membrane Swelling. *J. Am. Chem. Soc.* **2014**, *136*, 5309−5322.

https://dx.doi.org/10.1021/acscatal.0c04789
ACS Catal. 2021, 11, 1136−1178